Title
Third Sound in Superfluid ^{4}He Films Adsorbed on Packed Multiwall Carbon Nanotubes

Author
Menachekanian, Emin

Publication Date
2014

Peer reviewed|Thesis/dissertation

University of California

Los Angeles

Third Sound in Superfluid ^{4}He Films Adsorbed on Packed Multiwall Carbon Nanotubes

A dissertation submitted in partial satisfaction

of the requirements for the degree

Doctor of Philosophy in Physics

by

Emin Menachekanian

2014

Abstract of the Dissertation

Third Sound in Superfluid ^{4}He Films Adsorbed on Packed Multiwall Carbon Nanotubes

by

Emin Menachekanian

Doctor of Philosophy in Physics

University of California, Los Angeles, 2014

Professor Gary A. Williams, Chair

Third sound is studied for superfluid films of ^{4}He adsorbed on multiwall carbon nanotubes packed into an annular resonator. The third sound is generated with mechanical oscillation of the cell, and detected with carbon bolometers. A filling curve at temperatures near 250 mK shows oscillations in the third sound velocity, with maxima at the completion of the 4th and 5th atomic layers. Sharp changes in the Q factor of the third sound are found at partial layer fillings. Temperature sweeps at a number of fill points show strong broadening effects on the Kosterlitz-Thouless (KT) transition, and rapidly increasing dissipation, in qualitative agreement with the predictions of Machta and Guyer. At the 4th layer completion there is a sudden reduction of the transition temperature T_{KT}, and then a recovery back to linear variation with fill, although the slope is considerably smaller than the KT prediction. These effects might be related to changes in the gas-liquid coexistence regions.

The dissertation of Emin Menachekanian is approved.

Benjamin J. Schwartz

Karoly Holczer

Gary A. Williams, Committee Chair

University of California, Los Angeles

2014

This dissertation is dedicated to the memory of my father-in-law, Hagop Mikaelian. As an adamant supporter of my pursuit for the doctorate in physics, I hope that his spirit is cheerfully humming—as he did when he felt pure joy—now that I have reached the finish line.

Table of Contents

List of Figures

Acknowledgments

First and foremost, I would like to thank my advisor, Gary Williams, for being the best advisor any graduate student can ever have. He is an incredibly gifted experimentalist and talented theoretician, and I am so thankful that he gave me the opportunity to work on such a fascinating and fulfilling research topic. His support for my endeavors has been unparalleled. I am eternally grateful for his willingness to urge me to pursue the full-time professorship at Santa Monica College (SMC), even in the wake of the constraints this job would place on my research obligations in the lab. I will forever cherish the years I spent working in his lab, and I hope to inherit the same undying passion for physics that he has demonstrated over his illustrious career. His kindheartedness, care, patience, and humor made my experience in working under him truly unforgettable.

I would like to thank my wife, Armineh Mikaelian, who has supported me throughout this arduous journey with unmitigated love. I could not have asked for a better person with whom to share the rest of my life, as her will to provide me with the comfort I needed to be able to manage my various responsibilities was second to none. Our life as a married couple has been constrained due to these obligations, but her support has never wavered, and I am glad to finally be able to share more of my life with her upon finishing the doctorate.

Without the uncompromising support of my parents, Asik and Silva Menachekanian, none of my successes would have been possible. After my birth, they decided to leave the life they knew to join the rest of their family and relatives in the journey to start a completely new life in the United States. Through an act of complete selflessness, they raised my brother and me, and gave us the opportunity to pursue our dreams and to live a life unbounded. They went through many stressful years to give us all that we desired within their means. There are no words that can express how grateful I am to have them as my parents. Even

in the most difficult of times, they have provided my brother and me with more than for which we could have ever even asked. They dedicated their lives to help us achieve our goals, and instilled in us the importance of education. They never once urged us to work from a young age—even when they may have needed the financial assistance—because they knew that our future success would be directly related to focusing on our studies. They have cheered me on all the way to the end, and I hope that I have made them proud with my accomplishments.

I would also like to thank my brother, Meishel Menachekanian, who has been an incredible role model for me. Seeing his focus in going through higher education set a precedent for me to follow in his footsteps throughout my schooling career. My childhood was an incredible experience because of him. Even with our age difference, he was, and still is, my best friend, and I cannot thank him enough for being so supportive throughout the years. He has also been instrumental in my development as a human being, passing on to me a love for music and a genuine curiosity for the world around us. His spontaneity has made a big impact on me as well, especially as I recount the countless times that I ended up experiencing things I would not have otherwise experienced had it not been for his sense of exploration. I am very fortunate to have him in my life.

I am also very lucky to have wonderful extended siblings. Lauren Menachekanian, Ani Mikaelian, and Ray Badalyan have always supported my endeavors, and I am thankful to them for providing me with much-needed moral support in this long journey towards the light at the end of the tunnel. The tunnel had more light than originally anticipated because of their presence.

I would like to thank Harry Lockart and his crew at the Physical Sciences Machine Shop for fabricating the various parts used in this study. It was always a pleasure working with Harry to get the finer details mapped out in order to be able to use the machined parts successfully. Moreover, I owe a great deal to Shylo Stiteler, the supervisor of the Physical Sciences Student Machine Shop. He

patiently taught me the basics of machining and helped me to build some of the parts that I would end up using in these experiments. He is an extremely talented artist, and I will never forget the wonderful hours spent with him in the student shop.

Chuck Buchanan and Brent Corbin have been very meaningful in my development as a physics teacher. Being Chuck's teaching assistant on many occasions helped me see how an experienced professor approaches the teaching process. I will forever cherish the weekly meetings we had to discuss the progress of the students, as these would help shape my desire for student success. Brent was responsible for hiring me to teach physics workshops for PEERS (Program for Excellence in Education and Research in the Sciences), which has been an experience for which I am grateful. He has been instrumental in showing me the power in collaborative learning, which I try to use as much as possible at SMC. I am so fortunate to have him as a mentor and a friend, and he has been an integral part of my development as a challenging physics teacher who tries to make the teaching process fun for the students.

Finally, I would like to thank Jenny Lee, Carol Finn, Cecile Chang, and Elaine Dolalas. As graduate counselors and administrators, they have made my experience in the department as if I was part of an extended family. I will always remember their helpfulness, care, and warmth when I look back at my graduate career.

Vita

2007	B.S. (Physics), UCLA, Los Angeles, California.
2009	M.S. (Physics), UCLA, Los Angeles, California.
2012 - Present	Assistant Professor of Physics, Santa Monica College, Santa Monica, California.

CHAPTER 1

Introduction to Superfluidity in ^{4}He

The theoretical and experimental understanding of superfluidity currently spans a history of over a century. It was Kamerlingh Onnes' technological breakthrough of the liquefaction of ^{4}He that began the effort of understanding liquid helium and its novel properties. In particular, this chapter is devoted to giving a firm background in superfluidity in ^{4}He.[1] This introduction is based on various standard sources. [3–8]

1.1 The ^{4}He Phase Diagram

An enormous class of elements and molecules have a phase diagram similar to the one shown in Figure 1.1. The most important feature on which to focus in this figure is the fact that it is impossible for a material obeying such a generic phase diagram to remain a liquid down to absolute zero. Most such elements undergo freezing into a crystalline solid at their saturated vapor pressure (SVP) and remain a crystal down to absolute zero.

In sharp contrast, ^{4}He behaves rather differently, as can be seen in Figure 1.2. The reason for this behavior is discussed in Section 1.3. Interestingly enough, in

[1] The isotope ^{3}He also undergoes a superfluid phase transition. [1, 2] Much of the ideas mentioned in this section apply very nicely to this isotope. However, the mechanism by which ^{3}He undergoes the superfluid phase transition is very different from ^{4}He. This has to do with the fact that ^{4}He obeys bosonic statistics in which all such atoms have the ability to enter into the same quantum state; however, ^{3}He obeys fermionic statistics so that it can only undergo a superfluid transition if the ^{3}He atoms pair up to form a bosonic entity. This mechanism is analogous to the formation of Cooper pairs of electrons in superconductivity.

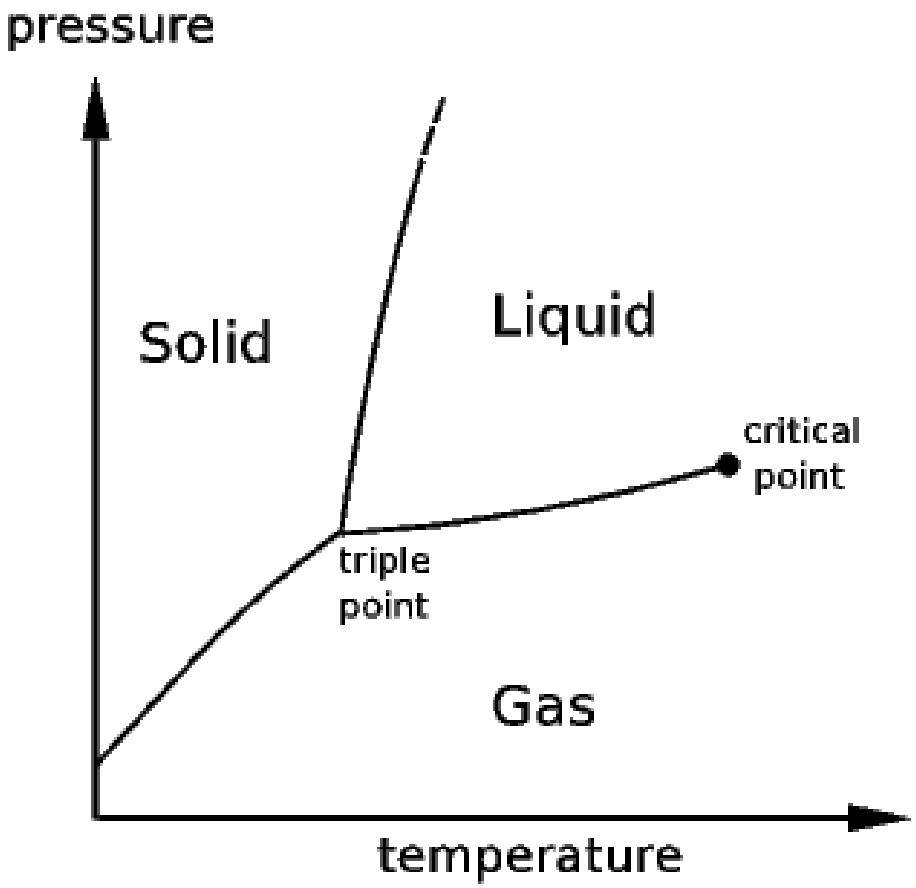

Figure 1.1: **Typical phase diagram of ordinary elements or molecules.** At ultra-low pressures the substance may remain in its gaseous state, but it is known that at SVP, almost all substances will condense into a solid phase at low-enough temperatures. Helium is the exception, even at very large pressures.

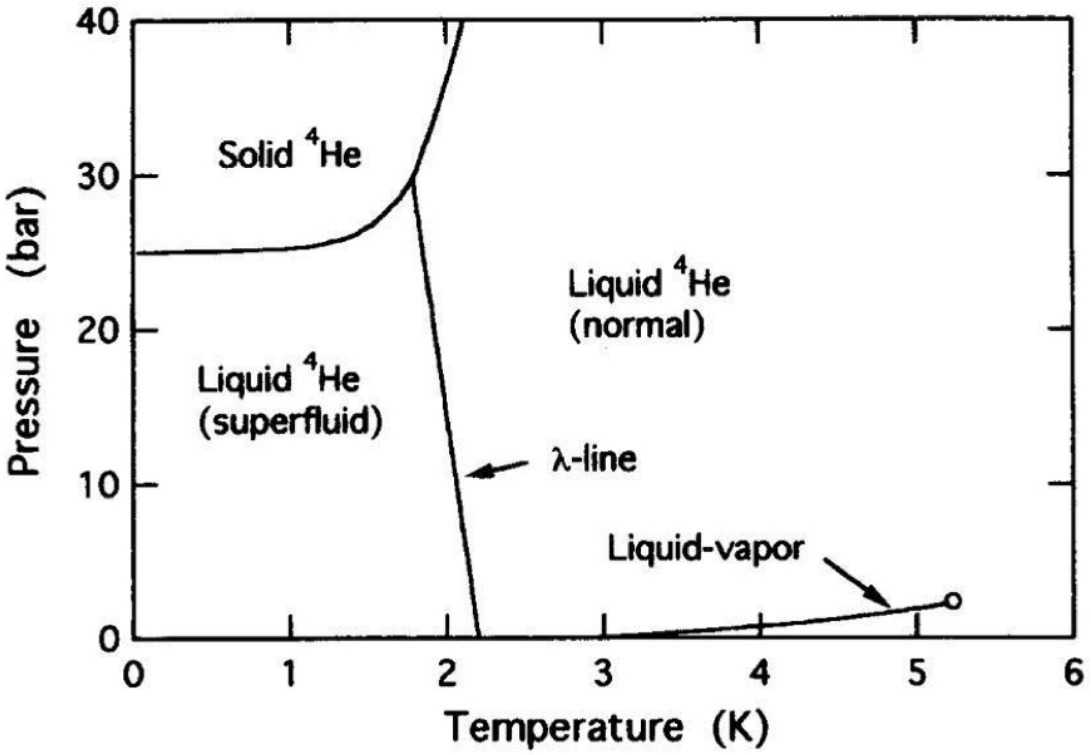

Figure 1.2: **The phase diagram of ^{4}He.** Notice how it remains a liquid down to absolute zero and requires about 25 bars of pressure in order to solidify around 1 K. The λ-line indicates the second-order phase transition separating the normal-fluid state (at high temperature) and the superfluid state (at low temperature).

order to achieve the crystalline phase in ^{4}He, one must necessarily apply enormous amounts of pressure: 25 atm or more. Furthermore, one sees that there is, in fact, no triple point in which a three-phase coexistence takes place. A critical point nevertheless exists, so that it is possible to go from the liquid to the gas phase (or vice versa) without having to incur a first-order phase transition (i.e., there exists no latent heat of transition between the two phases if the path in the phase diagram is mapped out appropriately in an experiment).

1.2 Determining the Importance of Quantum Effects

For most fluids in nature, quantum mechanics is reasonably irrelevant in understanding the properties of fluids and how they interact, even at low temperatures. Indeed, quantum-mechanical effects become much more significant when the thermal energy of a system is reduced. Namely, quantum effects dominate when $\hbar\omega \gg k_B T$, with $\hbar$ the reduced Planck's constant, k_B Boltzmann's constant, T the temperature of the system, and ω the characteristic quantum-mechanical frequency of the system at hand.

A fluid of ^{4}He particles is a fluid for which quantum effects drastically dictate how it behaves at low temperatures. From statistical mechanics, a useful measure from which one could roughly deduce the importance of quantum effects in systems of particles is the thermal de Broglie wavelength, defined by

$$\lambda_T \equiv \left(\frac{2\pi\hbar^2}{m k_B T} \right)^{1/2}, \tag{1.1}$$

where m is the mass of an individual particle in the gas under question. If λ_T is larger than, or of the same order as, other typical length scales in the fluid, then the quantum regime will have great bearing on the observed results. For instance, neon and helium share approximately the same interatomic separation d at the minimum of the potential energy of interaction between these particles in a gas. (For neon $d_{\mathrm{Ne}} = 0.296$ nm and for helium $d_{\mathrm{He}} = 0.265$ nm.) Also, the atomic masses are given by: $m_{\mathrm{Ne}} = 20.2$ u $= 3.35 \times 10^{-26}$ kg and $m_{\mathrm{He}} = 4.00$ u $= 6.65 \times 10^{-27}$ kg. At SVP, neon turns into a liquid at $T_{\mathrm{Ne}} \approx 27$ K and helium turns into a liquid at $T_{\mathrm{He}} \approx 4$ K. As a result[2], $\lambda_T^{(\mathrm{Ne})} \approx 7.5 \times 10^{-2}$ nm $< d_{\mathrm{Ne}}$ and

[2]In this case, the gas of particles is being treated as noninteracting, even though at these temperatures neon and helium are in a liquid state and, thus, are strongly interacting. In any case, such an estimate gives one a rough idea of the nature of the fluids and whether they behave classically or quantum mechanically. In fact, the de Broglie wavelength simply stems out of the momentum distribution for a collection of particles. So, although the potential energy may contain terms that couple particles together, the potential energy should generically not depend on the momentum of the particles. Thus, since λ_T is born out of the momentum distribution—

$\lambda_T^{(\mathrm{He})} \approx 0.44$ nm $\sim d_{\mathrm{He}}$. Thus, the helium fluid will be dictated more significantly by quantum effects than the neon fluid.

1.3 The Zero-Point Energy

The major quantum-mechanical effect that determines the behavior of helium at low temperatures is the zero-point energy (also known as the kinetic energy of localization). The zero-point motion in ^{4}He is not negligible when considering the total energy of the quantum fluid. The reason for this is two-fold: the ^{4}He mass is rather small and the interaction between ^{4}He atoms is weak in comparison to other elements.

To analyze this further, it is paramount to obtain an expression for the zero-point energy for the ^{4}He quantum fluid. Although the atoms in this quantum fluid move, one could say that, on average, one ^{4}He atom is contained[3] within a sphere whose radius is roughly the size of the interatomic spacing, a, so that its volume $\mathcal{V} \sim a^3$. From the Heisenberg uncertainty principle, the uncertainty in the momentum of such a ^{4}He atom is

$$\Delta p \sim \frac{h}{a} \sim \frac{h}{V^{1/3}}.$$

As a result, the kinetic energy of localization of this atom is given by

$$\mathcal{T}_0 \sim \frac{(\Delta p)^2}{2m_4} \sim \frac{h^2}{2m_4}\frac{1}{V^{2/3}}, \tag{1.2}$$

where $m_4 = 6.65 \times 10^{-24}$ g is the mass of the ^{4}He atom.

In order to complete the story, a rough expression for the interatomic potential energy must also be described. This is a rather complicated process, but the

which (for all practical purposes) decouples from the interaction potential—it is still permissible to gauge the importance of quantum effects using rough estimates of the thermal de Broglie wavelength.

[3] In other words, the ^{4}He atom under question is contained in an imaginary cage bounded by its nearest neighbors.

behavior of the interaction can be modeled upon considering both the weak, long-ranged (van der Waals) attraction as well as the relatively strong, short-ranged (exponentially decaying) repulsion of the helium atoms.[4] Such a potential can take the form

$$V(r) = \alpha e^{-\beta r} - \frac{\varphi}{r^6}, \tag{1.3}$$

where α, β, and φ are parameters that may be determined empirically. Such a potential will contain an attractive well since the two terms in Equation 1.3 compete with one another in the intermediate values of r. So, the total energy of the liquid helium, adding in the kinetic energy $\mathcal{T}_0$, then becomes

$$\varepsilon = \mathcal{T}_0 + V(r). \tag{1.4}$$

Qualitatively speaking, when plotting ε, $\mathcal{T}_0$, and V as functions of the atomic volume, one obtains Figure 1.3. The large zero-point contribution causes the total-energy minimum to be shifted to a considerably larger atomic volume in comparison to the minimum of the liquid's potential energy. So, even though the interatomic forces are apparently strong enough for helium to finally liquefy at 4.25 K (at SVP), the large zero-point energy keeps the density of the liquid rather small, thus preventing ^{4}He solidification. It is expected that the potential-energy minimum for a crystalline lattice of helium atoms would occur at a smaller atomic volume—in comparison to the liquid state—because of the dense nature of solids in general. Notice from Figure 1.3 that at smaller atomic volumes, the zero-point energy is considerably stronger. As a result, one must necessarily apply a great deal of pressure to the system in forcing the helium atoms to get closer together in order to finally achieve crystallization.

[4] A more accurate potential for the intermolecular attraction between helium atoms is the Aziz potential [9]. However, using the simplified potential here is to simply establish a qualitative argument for how zero-point effects are important to describe helium's status as a true quantum liquid.

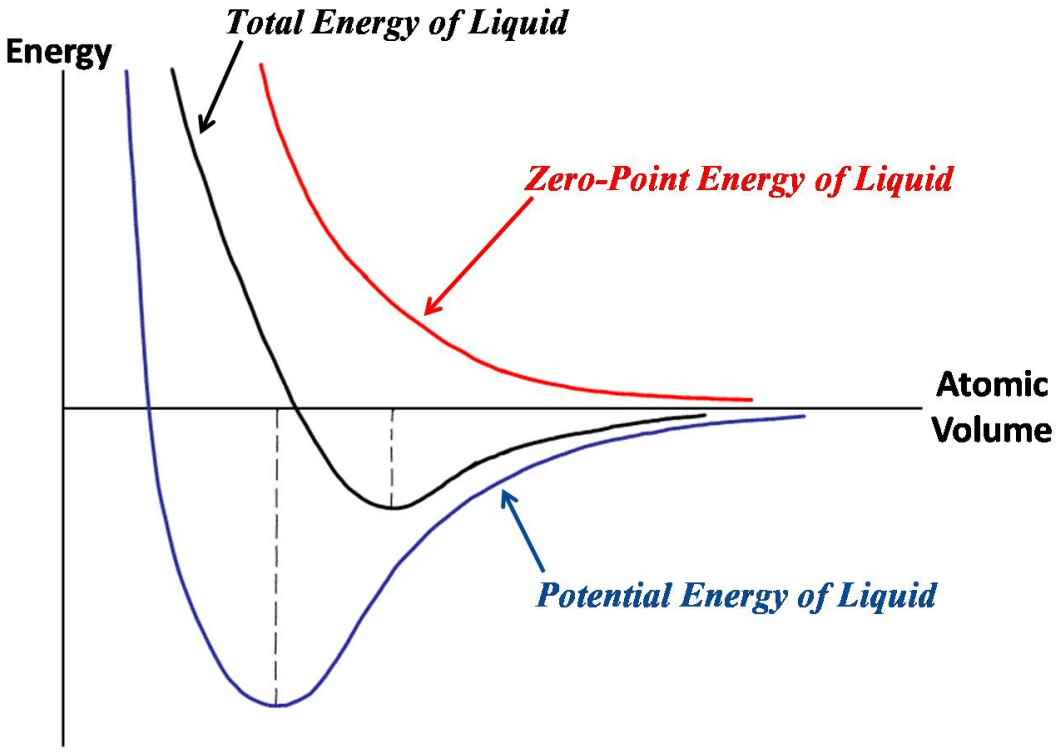

Figure 1.3: **Qualitative sketches of total energy, potential energy, and zero-point energy of liquid helium.** The zero-point-energy curve drives the total-energy minimum to higher values of the atomic volume in comparison to the minimum of the potential-energy curve, thus lowering the density of the helium atoms in the liquid and preventing crystallization without external pressure.

Helium is the only[5] substance that remains a liquid down to absolute zero. Indeed, the H_2 molecule has a van der Waals attraction that is approximately an order of magnitude larger than in the case of helium, due to the fact that hydrogen is much more easily polarized. It is true that the hydrogen atom should have a larger zero-point energy due to its smaller mass; however, the van der Waals attraction far outweighs the increase in zero-point energy in hydrogen, so that it necessarily chooses the stable configuration of solidification at low enough temperatures without the application of an external pressure. Furthermore, all atoms larger in mass than helium do not have enough zero-point energy to keep their densities small enough upon cooling. As a result, helium stands alone in its ability to remain a liquid down to absolute zero.

1.4 Experimental Evidence for Superfluidity in ^{4}He

Superfluidity in helium was discovered experimentally without any theoretical insight in making predictions regarding such novel behavior. Although one may explain it nowadays in terms of a Bose-Einstein condensation of a strongly interacting system of bosons, many of the phenomenologies developed—in particular, Landau's two-fluid hydrodynamics—owe to the overwhelming experimental evidence suggesting the existence of superfluidity in helium. Thus, it is worthwhile to discuss the experimental observations for further development of helium's theoretical background.

As can be seen in Figure 1.2, there are two distinct liquid phases in helium. (The nomenclature He I and He II is assigned to the normal and superfluid regions, respectively, in the phase diagram.) The line that separates the two regions is a line of phase transitions. This phase transition is (in the language of Landau) a second-order, or (in more proper, modern lingo) continuous, phase transition.

[5]This applies to both stable isotopes of helium (i.e., ^{3}He and ^{4}He).

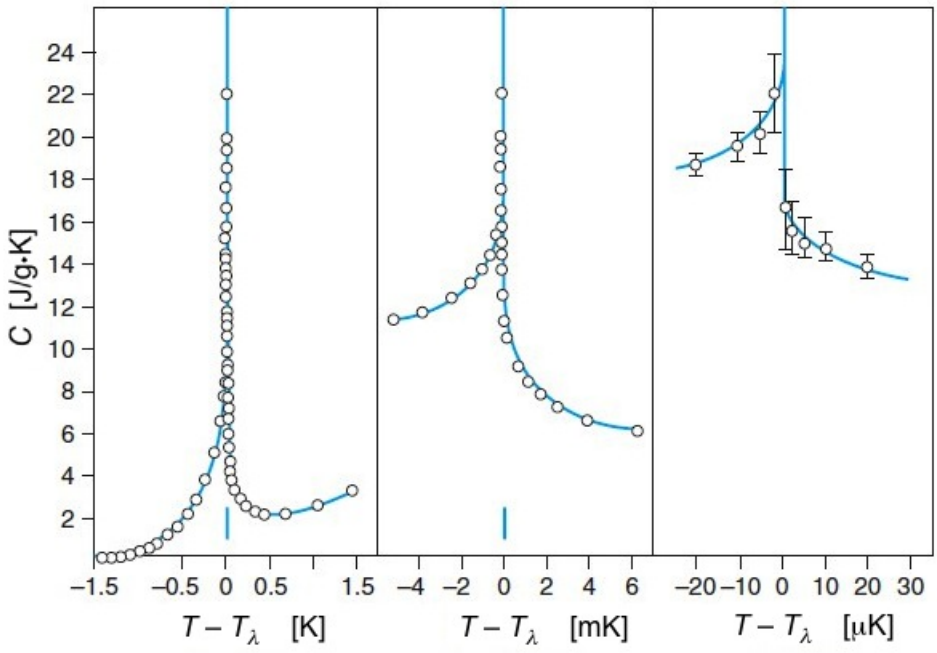

Figure 1.4: **The specific heat of ^{4}He as a function of $T - T_\lambda$.** The curve resembles the Greek letter λ, which is why the superfluid phase transition is referred to as the λ transition. Data in the plot is adapted from Reference [10]. Note the sharp feature at $T - T_\lambda = 0$ even at the micro-Kelvin resolution.

The second-order nature of the phase transition follows from the fact that as one traverses from the He I to the He II regime (or vice versa), there is no discontinuity in the thermodynamic state of the system. Instead, the phase transition occurs because of a discontinuous anomaly in the specific heat of ^{4}He as a function of temperature, shown in Figure 1.4. The shape of the specific-heat curve resembles the Greek letter λ, so that the phase transition line is dubbed the λ-line, while the transition temperature is called the lambda point T_λ. At SVP, $T_\lambda = 2.17$ K.

As mentioned previously, the two-fluid nature of He II was conjectured as a result of experimental evidence that suggested both the presence and absence of viscosity below the λ point. First, a discussion of two experiments which naturally showcase the absence of viscosity is in order. Pyotr Kapitza performed

an experiment in which he observed the flow velocity, v, of He II through narrow capillaries (ranging from a diameter of 0.1 μm to 4 μm). [11] In a normal fluid, the flow velocity will depend on the viscosity of the fluid, η, the pressure difference between the ends of the capillary, ΔP, the cross-sectional area of the capillary, A, and the length of the capillary, L. Through dimensional analysis of these fundamental quantities the dependence of η on ΔP, v, A, and L can be easily written:

$$\eta \sim \frac{A}{Lv}\Delta P. \tag{1.5}$$

No matter what capillary diameter was utilized in the experiment, it was found that even though a finite flow speed was detected, the pressure difference was always zero. As a result of Equation 1.5, the viscosity was therefore found to be essentially zero. Allen and Misener [12] obtained similar results in flow experiments as well.

Another experiment demonstrating the absence of viscosity in He II is the persistent-current measurements performed by Reppy and Depatie in 1964 [13]. In this experiment, a torus filled with liquid helium above T_λ was made to rotate at a given angular speed. Then, the liquid helium was cooled below the lambda point and, in turn, the external rotation was stopped. Over a twelve-hour period, measurements were made of the flow angular velocity and it was found that there was literally no reduction in the angular velocity. Indeed, in the case of a normal fluid with a finite viscosity, the angular velocity would have surely gone down to zero soon after the torus ceased to rotate: after the rotation stops, the walls in contact with the liquid no longer entrain the liquid to flow at the speed of the walls and, thus, the liquid gradually slows down to a halt. However, in the case of He II, the timescale—during which zero dissipation of angular velocity was observed in this experiment—was so large that the viscosity just had to be zero in order for such measurements to have even made sense.

Although these two experiments seem to suggest the zero-resistance nature of He II, other experiments actually showcase the opposite scenario. An elegant experiment was carried out by Alfred Leitner in 1963 in a low-temperature-physics demonstration video on superfluid helium that very nicely showcased the viscous nature of He II.[6] [15] The experimental schematic is shown in Figure 1.5. The induction coils are powered by an induction motor, and they are set up (as shown in Figure 1.5a) so that the copper cylinder can feel a torque set up by the magnetic field, spinning it in a predetermined direction. As seen in Figure 1.5b, both the copper cylinder and the propeller are placed in a bath of liquid helium.[7] The cylinder and the propeller are not connected. Furthermore, the propeller is not made of a magnetic material so that it is not affected by the stray magnetic fields from the induction coils.

Prior to cooling, it is expected that by turning on the induction coils to make the copper cylinder turn[8], the boundary layers of liquid in contact with the copper cylinder will also start moving. Indeed, because of the finite viscosity inherent in He I (which behaves as a normal fluid), the boundary layers of the liquid are entrained by the motion of the copper cylinder. Thus, one expects the propeller to attain the same circulation as the copper cylinder in the steady state.

As one cools below the lambda point, the ^{4}He transitions into the superfluid regime. Based on the aforementioned experiments, which showcased the absence of viscosity in He II, one would expect the rotation of the copper cylinder to no

[6]Experiments as early as 1938 validated the viscous nature of He II. In fact, the first suggestion for a two-fluid model was made by Tisza in 1938. [14]

[7]The apparatus is optically visible. To prevent thermal radiation, particularly from the infrared part of the spectrum, from entering into the cryostat (or dewar), the cryostats are normally made opaque with a highly-polished surface. In any case, to make the dewar optically visible, normally one surrounds the helium bath by a liquid nitrogen bath, thus providing a good shield from infrared and visible radiation. Finally, surrounding the liquid nitrogen bath is a vacuum jacket which serves as a means of not only keeping away air at room temperature from diffusing into the apparatus, but also reducing thermal conduction. These extra details are not shown in the schematics of Figure 1.5.

[8]Since ^{4}He has neutral charge, the magnetic fields generated by the induction coils do not have a net effect on the liquid helium itself.

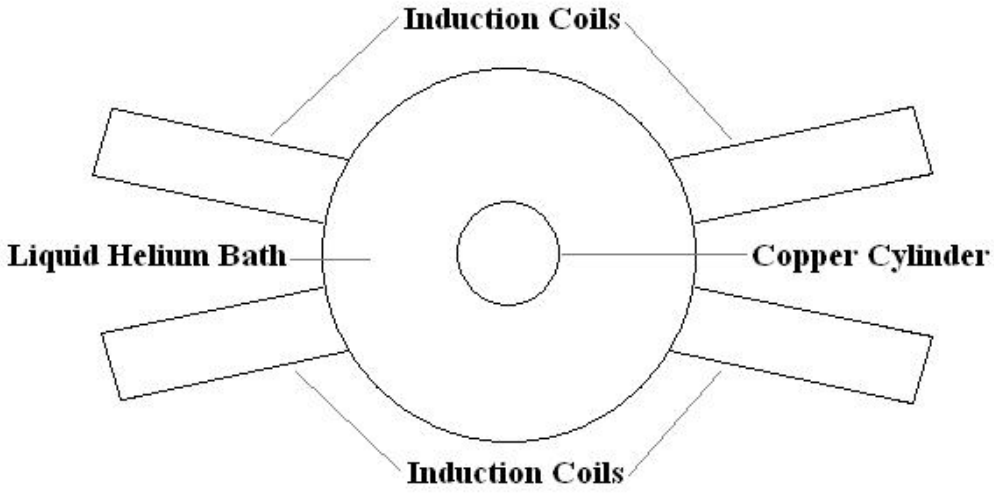

(a) Propeller Bottom View

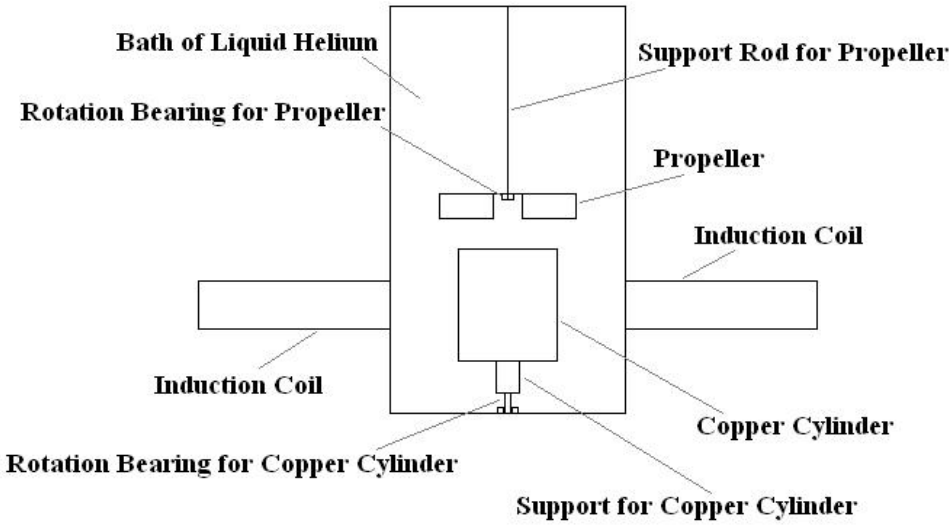

(b) Propeller Side View

Figure 1.5: **Schematic of Leitner's experiment for detecting a nonzero viscosity in He II.** The propeller is seen to rotate even though it is decoupled from a spinning source below it that is driven using induction. There is a viscosity within the liquid helium, as the only explanation of the propeller's rotation is through the entrainment of fluid layers, as in the classical notion of deriving a velocity gradient in the fluid from the entrainment of the fluid set forth by a moving wall.

longer result in a circulation of the propeller. Nevertheless, it is found that the motion of the copper cylinder still entrains the liquid boundary layers, eventually making the propeller acquire the same rotation as the cylinder. Since no other agents can possibly cause this rotation, this leads to the conclusion that He II has a viscous nature.

It is clear that none of the experimental findings can be invalidated, even though the results achieved seem to be rather paradoxical. The experiments were all carried out in an extremely accurate fashion and were reproduced by other experimentalists alike, thus reinforcing the truth of the observations. A way to get out of this apparent paradox is to reach, in essence, some form of compromise, which necessarily led to the proposition of a two-fluid model of He II. In this model, He II contains both a normal component (which behaves like any other classical, low-density fluid) and a superfluid component (which has absolutely no viscosity). [14, 16, 17]

However, none of the mentioned experiments have been able to showcase both the absence and presence of viscosity simultaneously. Thus, it is worthwhile to discuss an experiment which naturally caters to both sides of the story. This experiment involves measurements using a torsion pendulum, and was first conducted by Elepter Andronikashvili in 1946. [18] The apparatus for the experiment is shown in Figure 1.6.

The spacing between the discs (roughly on the order of 0.1 mm) is small enough such that, above the lambda point, all the (normal) fluid in between the discs would be completely dragged by the motion of the discs. If the rotational motion of the oscillator is parametrized by using the the azimuthal angle ϕ, then labeling I as the moment of inertia[9], β as some dissipative coefficient, κ as the stiffness of the torsion pendulum and τ as an external (possibly time-dependent)

[9]There is only a need to consider the single component of the generalized moment-of-inertia tensor $\overleftrightarrow{I}$ since the oscillatory motion is exclusively along the principal axis that runs along the string (running through the center of mass) attached to the oscillator.

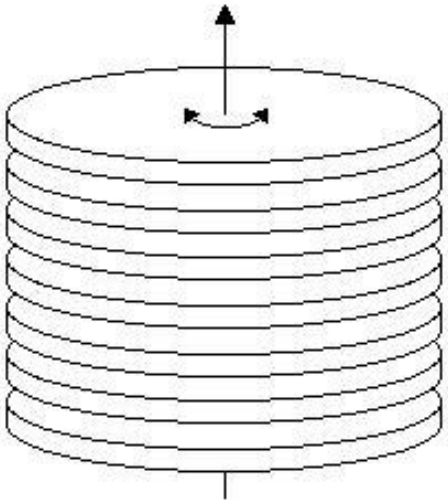

Figure 1.6: **Andronikashvili's torsion oscillator.** It consists of a pile of equally spaced, thin metallic discs suspended by a torsion fiber that can be twisted to allow for torsion oscillations. The spacing between the discs is on the order of 0.1 mm in the original Andronikashvili apparatus. [18] This spacing ensured enough viscous clamping of the normal component to the oscillator to couple to the moment of inertia of the discs.

torque, then the equation of motion is given by

$$I\frac{d^2\phi}{dt^2} + \beta\frac{d\phi}{dt} + \kappa\phi = \tau. \tag{1.6}$$

If the system is fairly non-dissipative, then the pendulum will obtain a resonance at approximately its natural (angular) frequency

$$\omega_0 = \sqrt{\frac{\kappa}{I}}. \tag{1.7}$$

Since the moment of inertia I is directly proportional to the density ρ, then the period of oscillations, $\mathcal{P}$ (which is inversely proportional to the frequency), depends on ρ as

$$\mathcal{P} \sim \sqrt{\rho}. \tag{1.8}$$

As a result, when the mass density decreases (increases), the resonant period decreases (increases) monotonically.

Upon conducting this experiment, it was found that cooling the liquid helium below the lambda point saw a significant decrease in the period of oscillation of the pendulum. In this sense, the transition to the superfluid state below T_λ necessarily makes the thinly separated discs entrain less fluid in their motion due to the fact that the superfluid component exhibits zero viscous drag. In cooling below the transition temperature, it is obvious that new helium particles are not being created, which implies that the fraction of atoms behaving as a normal fluid decreased as a result of the superfluid onset. Thus, the resonant period of oscillation in Equation 1.8 must be modified to take into account the decoupling of the superfluid component. In particular, the period will shift according to the amount of normal fluid present. In other words, $\mathcal{P} = \mathcal{P}(\rho_{\mathrm{n}})$. Dividing up the He II density, ρ, into a normal-fluid component, ρ_{n}, and a superfluid component,

ρ_{s}, the total density—in this development of the two-fluid hydrodynamics of He II—is equal to the sum of each component's density:

$$\rho = \rho_{\mathrm{n}} + \rho_{\mathrm{s}}. \tag{1.9}$$

As a result, extracting the normal fluid density based on the period shift in Andronikashvili's experiment, the superfluid density can then be measured upon applying Equation 1.9. The data (at SVP) is summarized in Figure 1.7. The λ point marks the temperature at which a macroscopic number of helium atoms occupy the superfluid state. At temperatures above T_λ, the total density is simply the normal-fluid density. Furthermore, notice that at about 1.0 K, $\rho_s \approx \rho$ and $\rho_n \approx 0$. However, if this curve is further extrapolated to absolute zero, then the entire fluid will strictly comprise of superfluid.

Utilizing the results of Andronikashvili's experiment, the absence of entropy can be deduced in superfluid helium with the help of the phase diagram of ^{4}He. Notice from Figure 1.2 that the melting curve (i.e., the solid-liquid phase coexistence line) is rather steep above the lambda point, while its slope essentially goes to zero in the transition below T_λ. The Clausius-Clapeyron equation for the melting curve states that the slope of this curve is given by

$$\frac{dP_{\mathrm{m}}}{dT} = \frac{S_{\mathrm{liq}} - S_{\mathrm{sol}}}{\mathcal{V}_{\mathrm{liq}} - \mathcal{V}_{\mathrm{sol}}} \equiv \frac{\Delta S_{\mathrm{m}}}{\Delta \mathcal{V}_{\mathrm{m}}}, \tag{1.10}$$

where S_{liq} and $\mathcal{V}_{\mathrm{liq}}$ are the entropy and volume in the liquid phase (respectively), and S_{sol} and $\mathcal{V}_{\mathrm{sol}}$ are the entropy and volume in the solid phase. Notice that because of the nature of the slope close to about 1.0 K, Equation 1.10 reveals that the change in entropy is essentially zero. So, looking at ^{4}He as a liquid in this temperature range, it is clear that the liquid cannot lose entropy by solidifying (since, due to Equation 1.10, the solid and liquid entropies exactly cancel one another). Thus, the liquid will choose to stay in its liquid state for a fixed

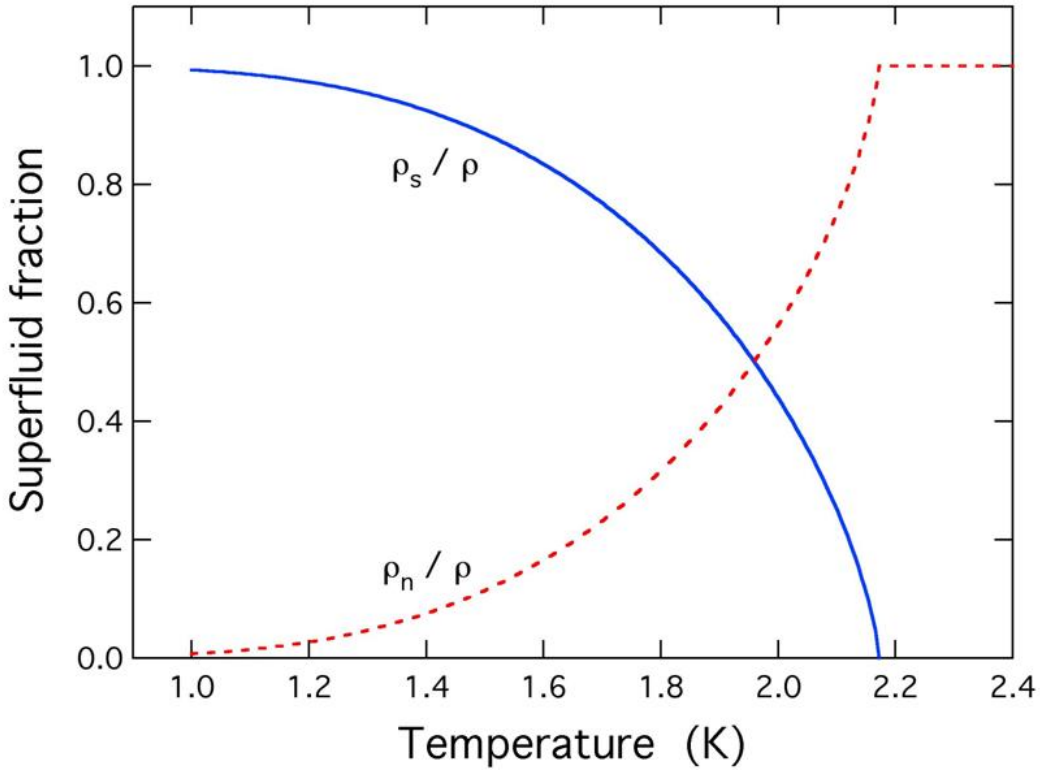

Figure 1.7: **The fraction of superfluid atoms, ρ_s/ρ, and normal fluid atoms, ρ_n/ρ, as functions of the temperature at SVP.** Notice how the superfluid fraction goes to zero as $T_\lambda = 2.17$ K is approached. Also, notice that the superfluid fraction almost completely dominates at approximately 1.0 K.

external pressure near the melting curve. Furthermore, since the Third Law of Thermodynamics must be obeyed, it is thus concluded that $S_{\text{liq}} \to 0$ as $T \to 0$. Moreover, as seen in Figure 1.7, He II consists completely of the superfluid fraction at absolute zero. Ultimately, in the scheme of the two-fluid model, the superfluid fraction carries no entropy, and all of the entropic content resides in the normal fluid. This then explains the nature of the melting curve above 1.0 K, since the normal fluid fraction above this temperature becomes considerably larger and, as a result, the entropic content of the liquid increases, as a whole.

From the experimental evidence suggested in Andronikashvili's experiment, it seems that the λ point triggers some sort of tendency for the helium to take form as a superfluid.[10] As such, one is inevitably led to think of the phenomenon of Bose-Einstein condensation, in which a gas of bosonic particles—at low enough temperatures—macroscopically condenses into the lowest quantum state. Thus, it is common for one to think of the superfluid transition as an occurrence of Bose-Einstein condensation, in which the superfluid component composes of the condensate, while the normal fluid consists of helium atoms in the excited states[11]. However, the picture is not as clear-cut as this. In fact, evidence—from deep-inelastic-neutron-scattering experiments [19] and from Quantum Monte Carlo (QMC) simulations [20–22]—suggests that the condensate is actually depleted. In other words, not all of the superfluid condenses into the lowest quantum-mechanical state. Indeed, due to the strong interactions present in He II, it is found that the condensate only consists of roughly 10% of the total fluid at absolute zero. In this sense, it seems as though the superfluid fraction comprises of

[10] It is not correct to say that the fluids can be separated physically. In other words, it cannot be said that some of the atoms are superfluid while others are normal. Indeed, at the quantum-mechanical level, ^{4}He atoms are indistinguishable since all such atoms are utterly identical. As a result, the correct way in which to describe the two-fluid nature of ^{4}He is to speak of the two "states" (super and normal) to be accessible to any helium atom at the same instant. The temperature dictates how many atoms, taken as a whole, will occupy one "state" as opposed to the other, with lower temperatures favoring the super "state" instead of the normal one.

[11] These excited states are identified as thermal excitations.

both the condensate and its depletion.

Without a doubt, many complications arise when including interactions in the theoretical framework of any system. However, it is still possible to understand the nature of the superfluid fraction by introducing the idea of the macroscopic wave function.

1.5 The Macroscopic Wave Function

The approach of introducing a macroscopic wave function is a bold step in understanding the nature of ^{4}He. The first proposition of the existence of such a wave function was due to Fritz London in 1954 [7]. He motivated its existence by creating a connection between dissipationless flow in superfluid helium and dissipationless flow of bound electrons in atoms. In the same way in which electrons orbiting a stable atom are described by a wave function (namely, an eigenfunction of the appropriate Hamiltonian describing the electron), London argued that such a wave function should also be able to describe the macroscopic nature of a body of superfluid. In this sense, the wave function should extend throughout the superfluid specimen. Thus, just as electrons are quantum-mechanical particles described by a (microscopic) wave function, superfluid currents are quantum-mechanical currents described by a (macroscopic) wave function. London's bold argument gave rise to postulating the existence of a wave function that describes superflow.

One can also motivate the presence of a quantum-mechanical wave function based on the existence of an order parameter in the description of the superfluid phase transition. Near the lambda point, the specific heat (at constant volume) has the form:

$$\mathcal{C}(T) = \begin{cases} \mathcal{C}(T) + A_{>} \left|T - T_{\lambda}\right|^{-\alpha} & (T > T_{\lambda}) \\ \mathcal{C}(T) + A_{<} \left|T - T_{\lambda}\right|^{-\alpha} & (T < T_{\lambda}) \end{cases}, \tag{1.11}$$

where $\mathcal{C}(T)$ is a smooth function of T close to T_{λ}, and $A_{>}$ and $A_{<}$ are constants. Such a discontinuity is typical of a continuous (or second-order) phase transition, which can be described using the Ginzburg-Landau formalism [23]. In particular, the transition is described by an ordering of an order parameter, which is effectively zero at and above the critical temperature T_{λ} and continuously becomes nonzero below the transition temperature. Over the course of the development of the Ginzburg-Landau theory, it has become evident that, depending on the nature of the order parameter (i.e., whether it is a scalar, two-component vector, n-component vector, second-rank tensor, etc.), seemingly unrelated phase transitions can be grouped into a particular class, referred to as a universality class. The universality class into which superfluid helium's phase transition falls is known as the three-dimensional XY-model[12] class. In this class, phase transitions are characterized by systems that attain a certain order that is fully described by a two-component unit vector

$$\vec{n}(\vec{r}) = (n_x(\vec{r}), n_y(\vec{r})) = (\cos[\theta(\vec{r})], \sin[\theta(\vec{r})]), \tag{1.12}$$

which is assigned at every point $\vec{r}$ in three-dimensional space. The angle θ parametrizes the two-dimensional unit vector. When above the lambda point the angle θ is spatially random (i.e., no true correlations exist between points in space), while below the lambda point there is a definite ordering in the angle θ (i.e., correlations begin to take hold). To physically draw the connection between the angle θ and the superfluid phase transition, one postulates the existence of a macroscopic, complex-valued wave function (which describes the condensate). In

[12]Which consists of a three-dimensional lattice of spins confined to rotate in a two-dimensional plane with some interaction between lattice sites.

this sense, the angle θ is exactly the phase of the wave function. In this proposition, it is expected that the phase of the wave function plays the critical role in the description of superflow in He II. The condensate wave function has the form

$$\psi(\vec{r}) = \psi_0(\vec{r})e^{i\theta(\vec{r})}. \tag{1.13}$$

Consider the condensate wave function in the Ginzburg-Landau framework of order parameters. If above the transition temperature and, as a result, $|\psi_0(\vec{r})| = 0$, then it is not possible to define the phase θ (i.e., there is no ordering in the phase); however, if below the transition temperature and, as a result, $|\psi_0(\vec{r})| \neq 0$, then the phase of the system can be defined and, thus, this phase can be identified as a physical parameter of the He II system.

From the microscopic quantum theory, for a wave function ϕ, the expression $\phi^*\phi = |\phi|^2$ for, say an electron, describes the probability density that one will find the electron at position $\vec{r}$. In the macroscopic case, such an interpretation does not make sense, simply because one is dealing with a macroscopic object composed of an enormous collection of atoms. Indeed, the important idea is that the macroscopic wave function should somehow relate to the fraction of helium atoms that are superfluid. So, if the number density of superfluid atoms is called ν_{s}, then it is conventional to normalize the condensate wave function such that

$$|\psi|^2 = \psi_0^2 = \nu_{\mathrm{s}}. \tag{1.14}$$

Integrating over all space, one finds:

$$\int d^3r|\psi(\vec{r})|^2 = \nu_{\mathrm{s}}\mathcal{V} = \mathcal{N}_{\mathrm{s}}, \tag{1.15}$$

where $\mathcal{V}$ is the volume of the space and $\mathcal{N}_{\mathrm{s}}$ is the number of superfluid atoms.

One may utilize the condensate wave function

$$\psi(\vec{r}) = \sqrt{\nu_{\rm s}(\vec{r})}e^{i\theta(\vec{r})} \tag{1.16}$$

to develop a mass-current density. Adapting the probability-current density from quantum mechanics into the superfluid (number) current density for the macroscopic wave function, one may write

$$\vec{J}_{\rm s}(\vec{r}) = \frac{\hbar}{2m_4 i}\left[\psi^*(\vec{r})\vec{\nabla}\psi(\vec{r}) - \psi(\vec{r})\vec{\nabla}\psi^*(\vec{r})\right]. \tag{1.17}$$

Noting that

$$\vec{\nabla}\psi(\vec{r}) = e^{i\theta(\vec{r})}\vec{\nabla}\sqrt{\nu_{\rm s}(\vec{r})} + i\sqrt{\nu_{\rm s}(\vec{r})}e^{i\theta(\vec{r})}\vec{\nabla}\theta(\vec{r})$$
$$\vec{\nabla}\psi^*(\vec{r}) = e^{-i\theta(\vec{r})}\vec{\nabla}\sqrt{\nu_{\rm s}(\vec{r})} - i\sqrt{\nu_{\rm s}(\vec{r})}e^{-i\theta(\vec{r})}\vec{\nabla}\theta(\vec{r})$$

then Equation 1.17 becomes:

$$\vec{J}_{\rm s}(\vec{r}) = \frac{\hbar}{m_4}\nu_{\rm s}(\vec{r})\vec{\nabla}\theta(\vec{r}). \tag{1.18}$$

Relating this (number) current density to the superfluid velocity via the relation

$$\nu_{\rm s}\vec{v}_{\rm s} = \vec{J}_{\rm s}, \tag{1.19}$$

then it is seen that the superfluid velocity is directly proportional to the gradient of the condensate wave function's phase:

$$\vec{v}_s = \frac{\hbar}{m_4}\vec{\nabla}\theta. \tag{1.20}$$

One may use Equation 1.20 to understand why the supercurrent is able to maintain a constant velocity over long periods of time, as seen in the experiment

of Reppy and Depatie (described in Section 1.4). Indeed, according to this equation, when the superfluid is at rest, the phase is constant. Furthermore, when the superfluid is moving at constant velocity, the phase varies uniformly in the direction of the superfluid velocity. In this sense, the phase appears to be a rather smooth function of position, even on a macroscopic scale.[13] The phase creates a form of coherence among the collection of particles over a macroscopic length scale, locking the particles into a state of uniform motion. Indeed, suppose one focuses on a particular superfluid helium atom flowing in a pipe. If this helium atom were to encounter an impurity in its path, then it would actually not scatter off of the impurity—contrary to what one would expect if the atom behaved classically (i.e., as a particle in a normal fluid). If the helium atom scattered, then due to the strong phase coherence, this would potentially cause every other superfluid atom to scatter as well. Energetically speaking, this would be an event so improbable that it could altogether be discarded. In this framework, it is therefore not surprising that the measured angular velocity in Reppy and Depatie's experiment [13] remained the same over such an extended period of time.

1.6 Vortices in Liquid Helium

In Section 1.5 it was found that a gradient in the phase of the macroscopic wave function gave rise to a finite superfluid velocity. In other words, it is the phase that determines the presence of superflow. For any well-behaved function $f = f(\vec{r})$, it is known from vector calculus that

$$\vec{\nabla} \times (\vec{\nabla} f) = \vec{0}.$$

So, as a result of Equation 1.20,

[13] This is not the case near a vortex core where the phase undergoes abrupt changes over a distance scale on the order of the atomic separation.

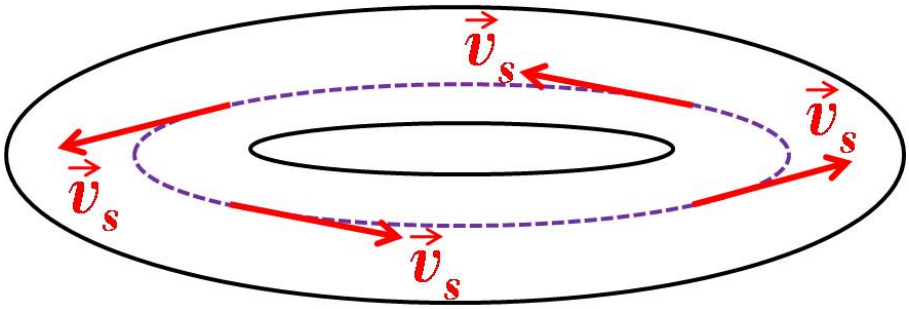

Figure 1.8: **Superflow in a torus.** The superfluid velocity, $\vec{v}_{\rm s}$, is tangent to the streamline and maintains a constant speed throughout.

$$\vec{\nabla} \times \vec{v}_{\rm s} = \vec{0}, \tag{1.21}$$

which, from classical fluid mechanics, implies that the fluid is irrotational (i.e., the fluid undergoes potential flow).

Now, suppose that there is superflow around a torus, as in Figure 1.8. The circulation is defined as

$$\Gamma = \oint_\gamma d\vec{\ell} \cdot \vec{v}_{\rm s}, \tag{1.22}$$

where γ represents the closed path and $d\vec{\ell}$ is an infinitesimal line element that is in the direction tangent to $\vec{v}_{\rm s}$ in Figure 1.8. Via Equation 1.20, and the utilization of the Fundamental Theorem for Line Integrals[14], it is seen that the circulation is independent of the path (by virtue of the nature of Equation 1.20) and is given by

[14]This theorem states that if $f(\vec{r})$ is a scalar field for which $\vec{\nabla} f$ is a well-behaved function, then for any path γ taken in the counter-clockwise (positive) orientation which begins at position vector $\vec{a}$ and ends at position vector $\vec{b}$, the value of the line integral of $\vec{\nabla} f$ taken over this path is given by:

$$\int_\gamma d\vec{\ell} \cdot \nabla f = f(\vec{b}) - f(\vec{a}).$$

This is the multi-dimensional equivalent of the Second Fundamental Theorem of Calculus.

$$\Gamma = \frac{\hbar}{m_4} \oint_\gamma d\vec{\ell} \cdot \vec{\nabla}\theta = \frac{\hbar}{m_4} \Delta\theta, \tag{1.23}$$

where $\Delta\theta$ is the change in phase over the closed loop.[15]

As in elementary quantum-mechanical situations, one desires the single-valued nature of the wave function. So, according to Figure 1.8, if one starts at a specific point on the drawn loop, performs a full rotation and returns to the same chosen point, then the value of the wave function must not have changed. In mathematical terms,

$$\psi(\vec{r}) = \psi(\vec{r}) e^{i\Delta\theta}. \tag{1.24}$$

As a result,

$$\Delta\theta = 2\pi q, \tag{1.25}$$

where $q \in \mathbb{Z} = \{0, \pm 1, \pm 2, \ldots\}$. Utilizing the quantization of this change in phase, Equation 1.23 showcases the quantized nature of the circulation

$$\Gamma = \frac{h}{m_4} q, \tag{1.26}$$

upon utilizing $\hbar = h/2\pi$. Thus, the quantum of circulation in ^{4}He is h/m_4.

As mentioned before, vortices are actually able to form even in the presence of such an irrotational flow. This can be seen with the use of some simple vector calculus. Indeed, because of the nature of the superfluid velocity in the form of Equation 1.20, based on Stokes' Theorem it is expected that

$$\Gamma \equiv \oint_{\partial S} d\vec{\ell} \cdot \vec{v}_\mathrm{s} = \int_S d\vec{S} \cdot \nabla \times \vec{v}_\mathrm{s} = 0, \tag{1.27}$$

[15]Here, the phase (as the so-called argument of a complex-valued function) has been allowed to acquire a nonzero change over the closed path.

where ∂S is the boundary of the surface S[16]. To look more closely at the curl of the superfluid velocity, it is instructive to write the superfluid velocity in cylindrical coordinates, $\vec{v}_{\rm s} = (v_r, v_\phi, v_z)$. Then the curl is given by:

$$\nabla \times \vec{v}_{\rm s} = \frac{1}{r}\det \begin{pmatrix} \hat{e}_r & r\hat{e}_\phi & \hat{e}_z \\ \frac{\partial}{\partial r} & \frac{\partial}{\partial \phi} & \frac{\partial}{\partial z} \\ v_r & r v_\phi & v_z \end{pmatrix}, \tag{1.28}$$

where $\hat{e}_i$ is the unit vector along the i direction ($i = r, \phi, z$). Consider now a rotating bucket of bulk superfluid helium. If the superfluid flows like a classical fluid—in which case the fluid would form a parabolic meniscus due to the centrifugal force present in the rotating frame—then one expects the fluid to only flow in the ϕ direction. Noting that the speed of the fluid can neither depend on the z direction (due to the translational symmetry along this direction) nor on the ϕ direction (due to rotational symmetry), then if Equation 1.28 is set equal to zero, one finds:

$$\frac{1}{r}\frac{\partial}{\partial r}\left(r v_\phi\right) = 0. \tag{1.29}$$

Solving this differential equation and identifying the definition of the circulation Γ, the superfluid velocity becomes

$$\vec{v}_{\rm s} = v_\phi(r)\hat{e}_\phi = \frac{\Gamma}{2\pi r}\hat{e}_\phi. \tag{1.30}$$

Furthermore, since the circulation is quantized, based on Equation 1.26, then

$$v_s = \frac{\hbar}{m_4 r} q \tag{1.31}$$

for $q \in \mathbb{Z}$.

[16] As in standard topological notation.

There is experimental evidence to showcase the fact that vortices can form even based on the irrotational nature of the flow in superfluid helium. The vortex lines were first predicted by Onsager [24] and Feynman [25]. Feynman predicted that the number of vortices that appear in a rotating bucket of superfluid helium would be directly proportional to the angular speed of rotation. His predictions were verified in 1975 with an experiment performed by Williams and Packard. [26] The experimental apparatus (shown in Figure 1.9a) consists of a cylindrical bucket into which liquid helium is poured and ultimately cooled. Using a potential difference, electrons are injected from the bottom and are able to flow up and through the normal-fluid cores of the vortices. When coming out of the other side of the vortex lines, the electrons strike a phosphor screen located at the top. The electrons light up the screen and, thus, allow for direct photographic evidence of the quantized vortices. The resulting photographs are displayed in Figure 1.9b.

The photographs were taken at various angular speeds and it was seen that the number of vortices increased in proportion to the angular speed. However, this was not simply a linear relationship. The number of vortices would remain the same for a range of angular speeds, until a given threshold was reached to permit the nucleation of another vortex. Thus, the relationship was more step-like, contrary to Feynman's aforementioned prediction. Furthermore, notice from Figure 1.9b that the vortices tend to form a lattice arrangement to minimize the overall energy of the system. This is particularly evident at higher rotation speeds, which suggests the tendency of the vortices to repel one another. The rotation speed in this case was always made to vary in a slow, continuous fashion. Indeed, abrupt changes in the angular speed of the bucket necessarily led to vortex entanglement, giving rise to nonlinear effects such as turbulence.

Although the rotating-bucket experiment gave rise to vortex lines, it is also possible to generate vortex rings, where the normal core—about which there is a circulation of He II—wraps around in a donut shape. The existence of these vortex

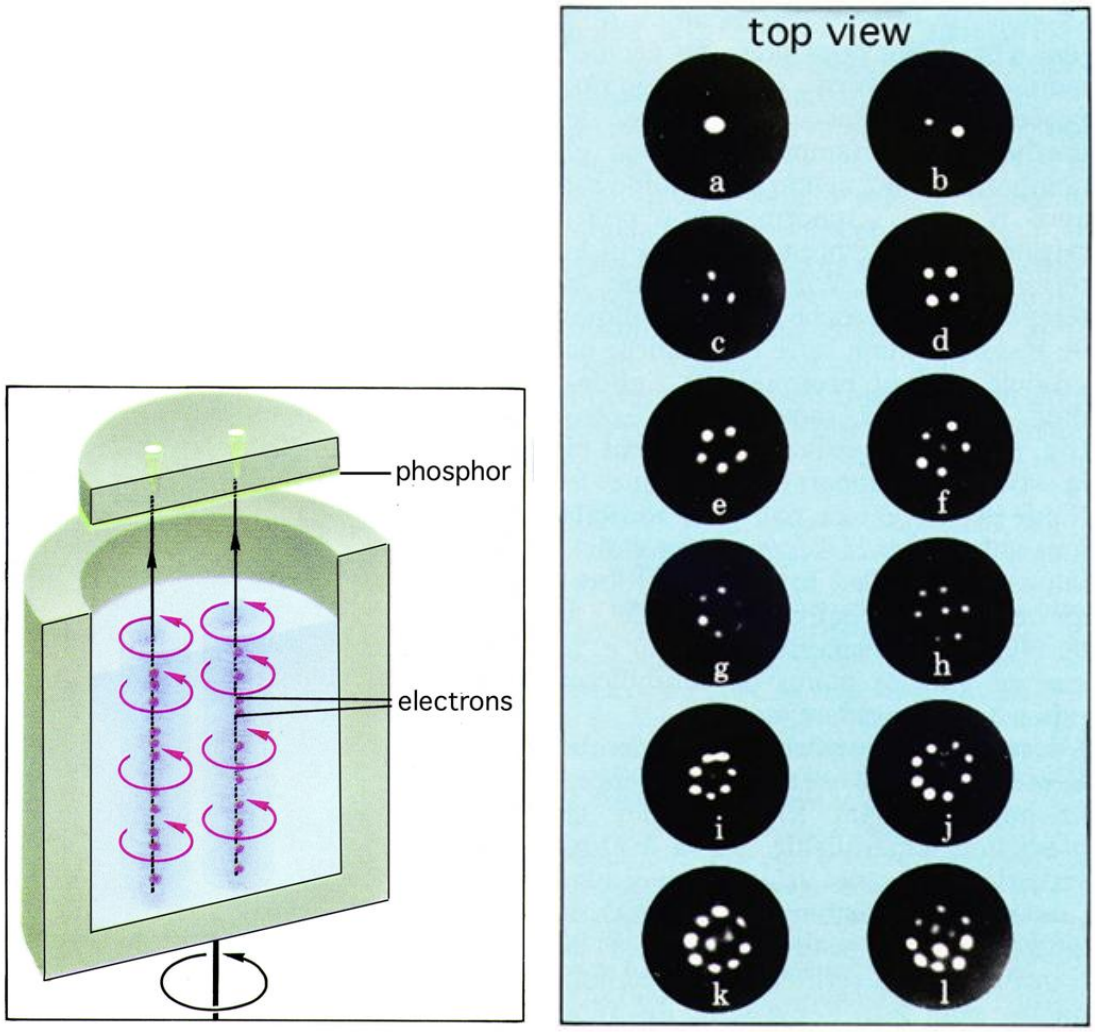

(a) (b)

Figure 1.9: **Experimental setup and results of vortex photography from Reference [26].** (a) The rotating bucket of superfluid helium. At a range of angular speeds, a fixed number of vortices nucleate and form a lattice. Electrons are injected from the bottom and travel through the normal-fluid cores to then get ejected from the opposite end of the vortex line to then collide into a phosphor screen. (b) Photographs of the vortices in the rotating bucket. Following the letters alphabetically corresponds to higher angular speeds. Note the formation of various lattice structures when more vortex lines nucleate on account of the interaction of the fluid with the cylindrical wall.

rings was established by the work of Rayfield and Reif in which time-of-flight measurements of an ion complex running through a chamber of He II were observed. A radioactive source generated excitations within the liquid helium which would then travel through the fluid unhindered when the temperature was low enough.[17] The excitations would then trap the ions used to initially form the complex upon using appropriate electric fields with appropriate potential differences to make the ions travel at the optimal speed for trapping.[18] Upon measurement of the energy of these complexes for a variety of ion velocities—set up by increasing or decreasing the potential differences of the ions generating the complex—it was found that this velocity varied inversely with the complex's (kinetic) energy—measured using the time of flight procedure—which was indicative of a traveling vortex ring from classical fluid mechanics. Moreover, it was also found that the circulation of these rings—upon measurement of the dispersion relation of the rings—was quantized in units of h/m_4, as in Equation 1.26.

These experiments undoubtedly confirm that vortices exist within the superfluid. These topological excitations play a significant role in Helium II, as vortices can cause superfluid atoms to scatter out of their ground-state configuration when a specific critical, or threshold, relative velocity is reached. Indeed, the relative motion between the superfluid and these vortices—whether two-dimensional vortex lines or three-dimensional vortex rings—leads to mutual friction forces, aiming to reduce the overall superfluid fraction. Indeed, as discussed by Anderson [27], these vortices can exchange energy with the flow of the superfluid, thus allowing for this energy to be carried away. This energy loss is a crucial idea in the onset

[17] An operating temperature of 0.3 K was deemed to be optimal in extending the mean free path of the ion complexes, as the primary hindrance was a drag resistance introduced by roton scattering. Operating at such temperatures reduced the roton density enough to suppress these scattering events.

[18] Too high a speed would force the ions to not be trapped within the complex and would lead to a further generation of other complexes as they traveled through more of the fluid. Too slow a speed would prevent the formation of a complex, resulting in the detection of the ion without an accompanying liquid excitation.

of dissipation in the superfluid and for providing the superfluid with a critical velocity far smaller than that predicted by Landau's model of the elementary excitations of Helium II. This notion of the reduction of the superfluid fraction on account of the interaction between superfluid atoms and such topological excitations will be further discussed shortly, but it is important to shed light on how these vortices mold the Helium II excitation spectrum beyond Landau's treatment of elementary excitations.

Indeed, the notion of a critical velocity was crucial in Landau's phenomenological development of the superfluid dispersion relation [30], shown in Figure 1.10. The dispersion relation showcases the presence of elementary excitations within the fluid at some temperature for a motionless fluid. The energy gap in the dispersion relation is a necessity if there truly is frictionless flow in such a system. Under the application of an external flow of this fluid, there is a means by which a helium atom, with some probability, can be scattered from the superfluid state to the normal-fluid one upon the further generation of elementary excitations. In particular, when the external flow reaches some critical velocity—determined by the slope of the dotted tangent line in Figure 1.10—the number of elementary (roton) excitations increases, resulting in flow that is no longer dissipationless. Inelastic neutron scattering experiments have verified the Landau dispersion relation for helium. [31] Note the tangent line that runs through both the predicted and the experimental data in Figure 1.10. The notion of superfluidity is that there is an energy gap that prevents excitations from taking place, which inevitably results in the fluid flow being dissipationless. Only when the flow has the appropriate velocity to nucleate excitations will there be considerable dissipation. Such excitations can be mechanically generated, such as in the rotation of a bucket of superfluid helium which nucleate vortices on account of interaction with the container boundaries[19], or they can be thermally agitated from the inherent

[19]These vortices are inherently macroscopic and should not necessarily be considered as elementary excitations. The quantum of a vortex can be thought of as a roton, so that the

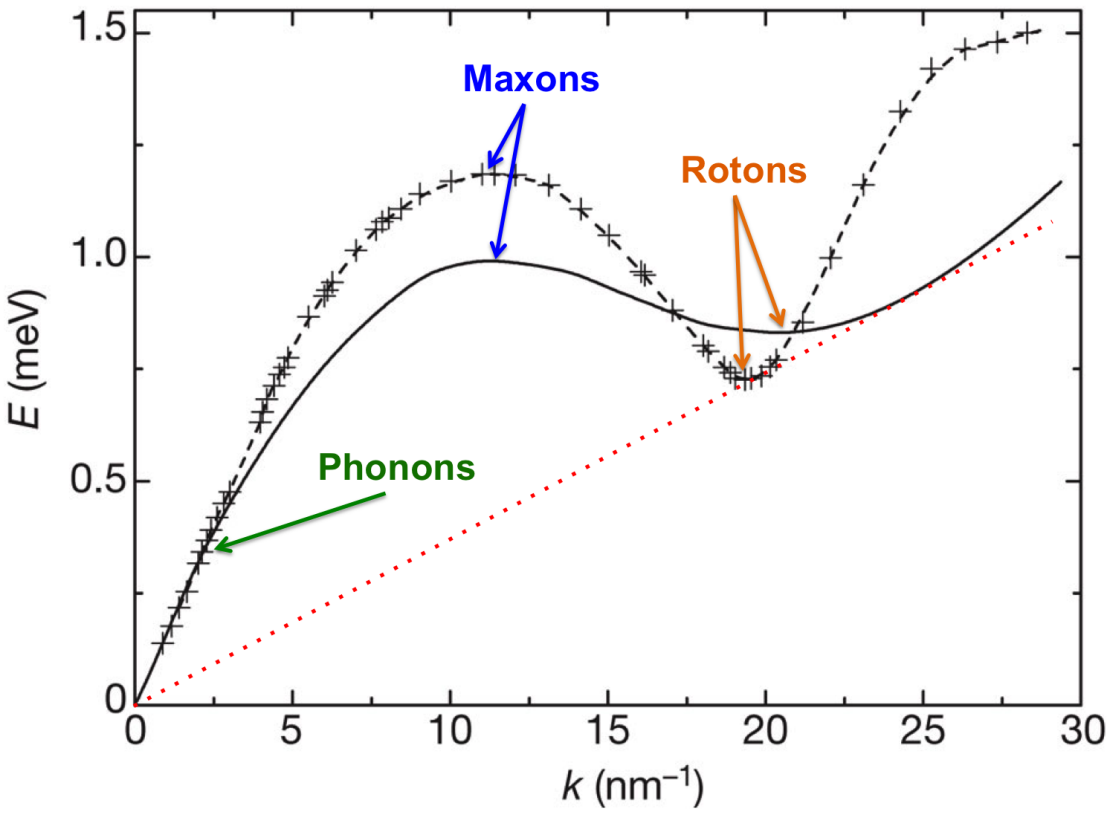

Figure 1.10: **Landau's dispersion relation for superfluid ^{4}He.** The solid line represents Landau's prediction for the helium dispersion relation at $T = 0$. The crosses correspond to neutron-scattering data of the dispersion curve from Reference [28]. This plot has been taken from Reference [29]. The dotted line, which was added to the plot, represents the tangent line which runs through both the experimental data and Landau's prediction. The slope of this line represents $\hbar v_c$, with v_c the critical velocity necessary for the lowest-energy, roton excitations.

restlessness of the fluid constituents.

Based on Landau's phenomenology, it is the energy gap associated with the roton minimum, as well as the lack of any other thermal excitations below the dispersion curve in Figure 1.10, that ensures the notion of flow without viscosity. The critical velocity at which the lowest-energy, roton excitations take place, known as the Landau criterion, is at a relative velocity of $v_c^{(R)} = 58$ m/s. Although experiments [32,33] studying this critical velocity have corroborated a theoretical prediction [34] of $v_c^{(R)} = 46$ m/s, critical values of the superfluid velocity have been seen to be one or more orders of magnitude smaller than $v_c^{(R)}$. Such measurements were aimed to study an intrinsic mechanism by which the superfluid component could invariably go from frictionless to dissipative flow without considering its interaction with the normal-fluid component. In order to eliminate the normal-fluid component from the picture, these experiments were performed under circumstances in which the normal fluid would either be stationary or would undergo laminar flow. Although the mechanism by which rotons are created would seem to be a proper candidate for explaining the transition into dissipative flow for the superfluid component, the measured critical velocities did not corroborate the value set forth by the Landau criterion. An example of such an experiment which resulted in critical velocities much smaller than those predicted by Landau is the persistent-current measurements of Reppy and Langer in a superleak—thus viscously clamping the normal-fluid component—with the use of a superfluid gyroscope. [35,36] A direct measurement of the precessing angular-momentum, whose magnitude is proportional to the angular speed of the current, provided a means of measuring the critical angular momentum at which a considerable decay was seen. Transforming the angular momentum into a linear speed then outputted critical velocities on the order of 10 - 100 cm/s, depending on the temperature and the superleak's pore size. Thus, Landau's elementary excitations are not sufficient to

generation of a macroscopic number of rotons can essentially correspond to the production of a larger-scale vortex.

explain all the intricacies associated with superfluidity.

To this end, the inclusion of (macroscopic) vortices in superfluid helium tends to paint a more complete picture of the physics associated with this exotic phase. In fact, it is now well known that vortices appear as a result of the thermal energy contained within the superfluid, and that these thermally-excited vortices are essential in the physics of the helium phase transition, particularly in two dimensions.[20] Indeed, one of the most compelling pieces of evidence for this came as a result of torsion-oscillator measurements of helium films on flat substrates. [37] Consider a flat substrate isolated in an evacuated chamber that is in good thermal contact with a liquid-helium bath that can be cooled to temperatures sufficiently below the λ point. Upon metering helium gas into an evacuated chamber in which the substrate resides, some of the helium atoms will get attracted to the flat substrate due to the van der Waals attraction between the helium atoms and the substrate material.[21] Naturally, the helium atoms will adsorb onto the flat substrate, and one could control the film thickness by measuring the vapor pressure. In any case, the film thickness (ranging from ~ 0.4 nm all the way to ~ 40 nm) can be controlled in very small steps, depending on the resolution of the apparatus used to meter in the helium gas. Even if the temperature of the outside bath is below the λ point at SVP, the film that forms on the substrate may not necessarily be superfluid. In fact, there is a threshold thickness above which the film is finally able to support superfluidity (i.e., form a superfluid layer

[20] As mentioned before, superfluid helium can be treated as a strongly interacting Bose-Einstein Condensate (BEC). Although it is well known that a noninteracting boson gas cannot undergo a BEC transition at any finite temperature in two dimensions, an interacting Bose gas can undergo such a transition. Superfluidity in ^{4}He films is a specific case in point.

[21] This attraction is mediated by electric-dipole interactions between the helium atoms and the substrate, and is a natural occurrence in even everyday life. For example, one can look very closely at a recently consumed glass of wine to find that there is a reddish hue to the glass that was not present when the glass was clean. This reddish hue is a result of an adsorbed film of red wine to the glass. Although the red wine and the glass may certainly not be electrically charged, there is nonetheless an attractive interaction that "glues" a thin layer of wine to the glass. This is a manifestation of the effects of capillarity that take place when a small-diameter tube is able to suck up liquid without an ambient pressure differential.

of atoms).

Bishop and Reppy were able to map out the superfluid fraction as a function of temperature for various film thicknesses on a Mylar substrate. Their results are presented in Figure 1.11. These results were a direct observation of the so-called Kosterlitz-Thouless (KT) phase transition. [39] Such a phase transition applies to any system that is in the same universality class as the the two-dimensional XY model, one of which happens to be the ^{4}He film. Indeed, this KT theory was fully applied to describe the two-dimensional phase transition of helium films into a superfluid state by Kosterlitz, Thouless, and Nelson (KTN). [40] The theory explained the disappearance of superfluidity in a ^{4}He film as a result of thermal excitations of vortex-antivortex pairs. These pairs comprise of vortices of opposite orientation (i.e., one with clockwise circulation and the other with counterclockwise circulation) that are topological excitations created solely through the available thermal energy within the helium film. A single vortex costs too much energy to be created[22]; however, at the KT onset temperature, T_{KT}, the bound vortex pairs unbind and drive down the superfluid density to zero. The drop is abrupt, as can be seen in the dashed line in Figure 1.11, and this drop in the superfluid areal (mass) density, σ_{s}, is predicted by the KT theory to be a universal[23] jump governed by the relation

$$\left(\frac{\sigma_{\mathrm{s}}(T)}{T}\right)_{T_{\mathrm{KT}}} = \frac{2}{\pi}\left(\frac{m_4}{\hbar}\right)^2 k_{\mathrm{B}} = 3.49 \times 10^{-9}\ \mathrm{g/cm^2 \cdot K}, \tag{1.32}$$

where $m_4 = 6.65 \times 10^{-24}$ g is the ^{4}He mass, $\hbar = 1.05 \times 10^{-27}$ erg $\cdot$ s is the reduced Planck's constant, and $k_{\mathrm{B}} = 1.38 \times 10^{-16}$ erg/K is Boltzmann's constant.

To fully appreciate the consequences of the KTN theory, it is worthwhile to briefly outline its development. It begins with the energy, V_0, required to excite a

[22]Since it would require circulating the entire film of ^{4}He atoms.

[23]The relationship is deemed universal because the ratio of the areal superfluid density to the temperature is written in terms of universal constants, as seen in Equation 1.32.

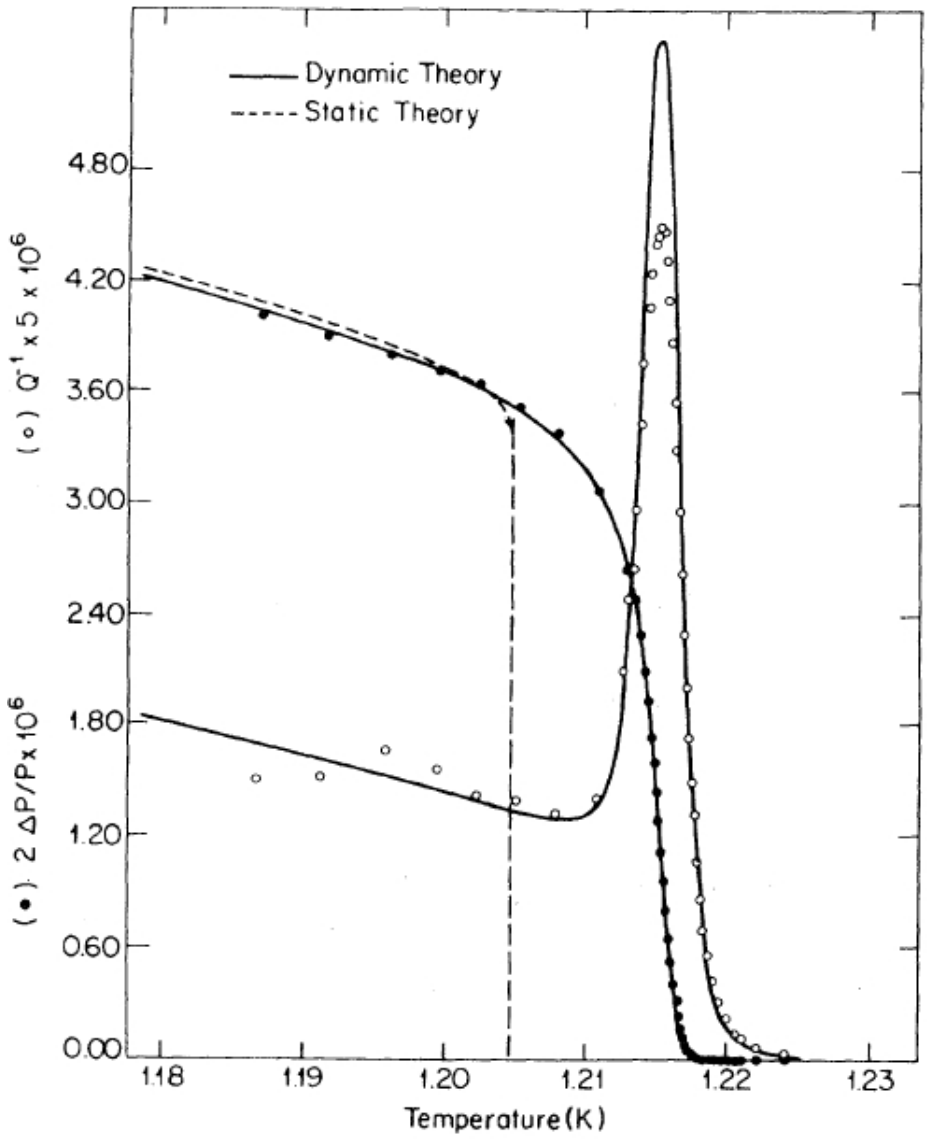

Figure 1.11: **Torsion oscillator measurements of superfluid films made on a flat substrate taken from the work of Bishop and Reppy [37].** The substrate is a Mylar film, which is a stretched, polyester film. The solid lines are fits to the dynamical theory of Ambegaokar *et al.* [38]. The dashed line represents the Kosterlitz-Thouless (KT) transition for a static film. Note the strong attenuation, Q^{-1}, when the normalized period-shift, $\Delta\mathcal{P}/\mathcal{P}$—and thus the superfluid fraction—decreases toward zero. The attenuation profile would be a lot sharper (ideally a Dirac-δ function), and would be centered at the dashed line, if there were no finite-frequency effects.

single vortex-antivortex pair, which is given by

$$V_0 = 2\pi K_0 \ln\left(\frac{r - a_0}{a_0}\right) + 2E_c, \tag{1.33}$$

where a_0 is the vortex core size, E_c is the vortex core energy, r is the separation distance of the vortex pairs (taken from their centers), and K_0 is the dimensionless areal superfluid density given by

$$K_0 = \left(\frac{\hbar}{m_4}\right)^2 \frac{\sigma_s^{(0)}}{k_B T}, \tag{1.34}$$

with $\sigma_s^{(0)}$ the "bare" areal superfluid density (i.e., in the absence of vortices). This so-called "undressed" superfluid density will become "dressed" in the scheme of the renormalization-group analysis that will eventually follow.

The vortex pairs polarize on account of a static superflow since they feel a Magnus force in opposite directions, the net result of which is to reduce the supercurrent with its own opposing flow field.[24] The schematic shown in Figure 1.12 showcases some vortex-antivortex pairs on such a two-dimensional substrate. In particular, note the direction of the flow field between one of the pairs, which is denoted by the arrow in the figure. This arrow will aim to orient completely antiparallel to the externally applied superflow. Since the areal superfluid density is proportional to the net superflow, this reduction in the supercurrent, on account of the backflow generated by the polarized vortex-antivortex pair, results in a reduction of this density. The lower the temperature, the more tightly bound these pairs are since there is very little thermal energy available. These tightly bound pairs will not be successful in the macroscopic reduction of the superfluid fraction. However, upon increasing the temperature, more vortex pairs are excited with larger separation. The pairs with smaller separation tend to screen

[24] This is analogous to Lenz's law in electromagnetism, in which a Lorentz force will result in the re-orientation of a magnetic dipole to reduce an increasing magnetic flux running through the loop.

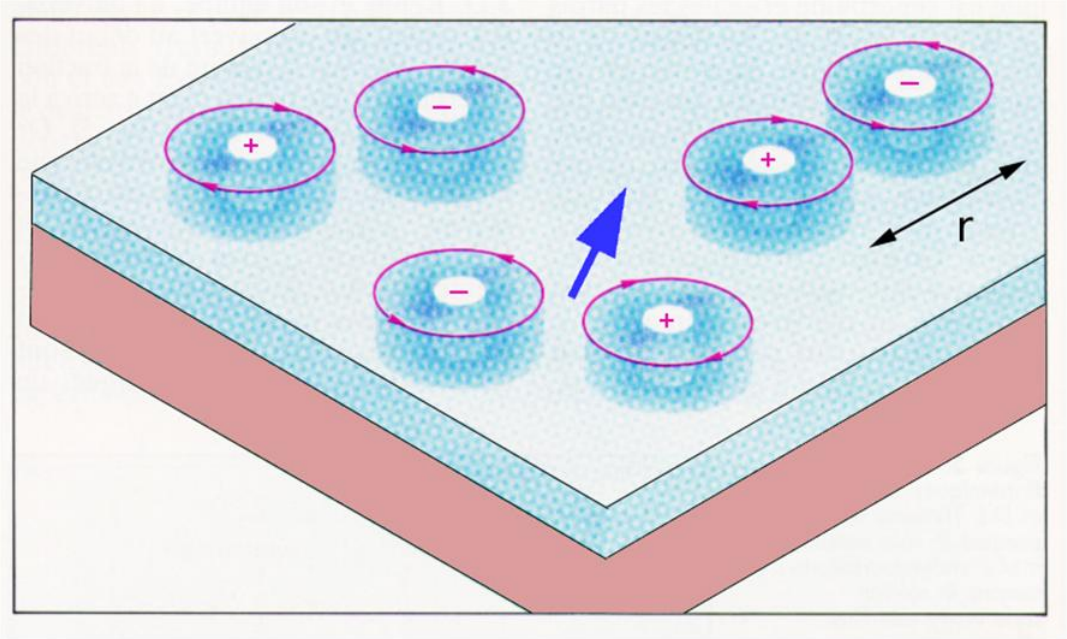

Figure 1.12: **Cartoon of the creation of vortex pairs on a two-dimensional substrate with an adsorbed superfluid film.** The arrow indicates the direction of flow in between a particular vortex-antivortex pair that is caused by the pair. Such pairs will polarize in a way to make this arrow counter the externally applied superflow, thus aiming to renormalize the areal superfluid density.

the flow field generated by the pairs at larger separation. This screening is the reason why it is possible reduce the energy required to excite vortex-antivortex pairs at larger separation.[25] In other words, without such screening, there would not be enough thermal energy available to allow for the complete reduction of the supercurrent on macroscopic length scales, which is what is necessary for a true phase transition to occur from a superfluid film to a normal-fluid film at a high-enough temperature.

Just as a dielectric can be used to reduce the electric field within a material—on account of the polarization field generated by the bound, dipolar atoms in the insulator aligning against the field—the same idea may be applied to describe

[25] Otherwise, it would be energetically improbable to generate such pairs at large separations.

the reduction of the areal superfluid density from the excitation of the vortex pairs. Introducing the dielectric function $\epsilon(r)$—which is a function of the pair separation, r—the reduced superfluid density, $\sigma_{\rm s}$, may be written in terms of the "bare" superfluid density as

$$\sigma_{\rm s} = \frac{\sigma_{\rm s}^{(0)}}{\epsilon(r)}. \tag{1.35}$$

The dielectric function can be redefined in terms of the susceptibility, $\chi(r)$, as in electromagnetism, as:

$$\epsilon(r) = 1 + 4\pi\chi(r). \tag{1.36}$$

Knowing the distribution of vortex pairs, $\Gamma(r)$, and the polarizability of a pair, $\alpha(r)$, linear response theory may be used to come up with a value for the susceptibility:

$$\chi(r) = \int_{a_0}^{r} dr' \Gamma(r')\alpha(r'), \tag{1.37}$$

with

$$\alpha(r) = \pi K_0 r^2. \tag{1.38}$$

The screened energy, $V(r)$—as opposed to the bare energy, V_0, from Equation 1.33—is given by

$$V(r) = 2\pi K_0 \int_{a_0}^{r} \frac{dr'}{r'} \frac{1}{\epsilon(r')} + 2E_{\rm c}, \tag{1.39}$$

and this form can be used to then obtain the distribution of pairs upon utilizing Boltzmann statistics:

$$\Gamma(r) = \frac{2\pi r}{a_0^4} e^{-\frac{V(r)}{k_{\mathrm{B}}T}}. \tag{1.40}$$

Using Equation 1.35, the dimensionless superfluid density is renormalized with the help of the dielectric function:

$$K(r) = \left(\frac{\hbar}{m_4}\right)^2 \frac{\sigma_{\mathrm{s}}}{k_{\mathrm{B}}T} = \frac{K_0}{\epsilon(r)}. \tag{1.41}$$

Using Equation 1.36, Equation 1.41 may be written in terms of the susceptibility, $\chi(r)$ as

$$K^{-1}(r) = K_0^{-1} + 4\pi\chi(r). \tag{1.42}$$

It is useful to introduce the vortex fugacity in its bare form,

$$y_0 = e^{-\frac{E_{\mathrm{c}}}{k_{\mathrm{B}}T}}, \tag{1.43}$$

only to then transform it to its renormalized form,

$$y(r) = y_0 \left(\frac{r}{a_0}\right)^2 e^{-\frac{Ur}{k_{\mathrm{B}}T}}. \tag{1.44}$$

For further convenience, the pair separation, r, is redefined in terms of the parameter l defined by

$$r = a_0 e^l. \tag{1.45}$$

Along with this reparametrization of r, upon using Equations 1.36, 1.37, 1.38, 1.40, and 1.39, the renormalized, dimensionless superfluid density, $K(r) = K(l)$, in Equation 1.42 gets rewritten as

$$K^{-1}(r) = K_0^{-1} + 4\pi^3 \int_0^l dl' y^2(l'), \tag{1.46}$$

while the renormalized vortex fugacity in Equation 1.44, $y(r) = y(l)$, becomes

$$y(l) = y_0 e^{\int_0^l dl'[2-\pi K(l')]}. \tag{1.47}$$

The integral equations 1.46 and 1.47 can be recast into differential form, known as the KT (differential) recursion relations:

$$\frac{dK^{-1}(l)}{dl} = 4\pi^3 y^2(l) \tag{1.48a}$$

$$\frac{dy(l)}{dl} = [2 - \pi K(l)]y(l) \tag{1.48b}$$

Solving these recursion relations gives rise to the universal jump result in Equation 1.32. The temperature at which the jump occurs is called the KT transition temperature, T_{KT}. Films of different thickness have a different value of T_{KT}. At the coldest temperatures, the ^{4}He film can support a submonolayer superfluid film, leading to the smallest value of T_{KT}. Increasing the temperature results in more thermal energy, making it necessary to build up to a thicker film in order to support a superfluid layer. As a result, there is a larger critical onset thickness when the temperature is higher. Nonetheless, the universal jump occurs at T_{KT} for a given onset thickness, so that Equation 1.32 really represents a line of phase transition points, known as the KTN line, when, for instance, making measurements of the superfluid density as a function of the film thickness and temperature, as shown in Figure 1.13.

However, in making experimental measurements of the KT transition on flat substrates—whether by means of a torsion oscillator [37] or by detecting surface waves in the ^{4}He, known as third sound[26] [42]—a static approach is not going

[26]Third sound will be discussed in Section 1.8 in further detail.

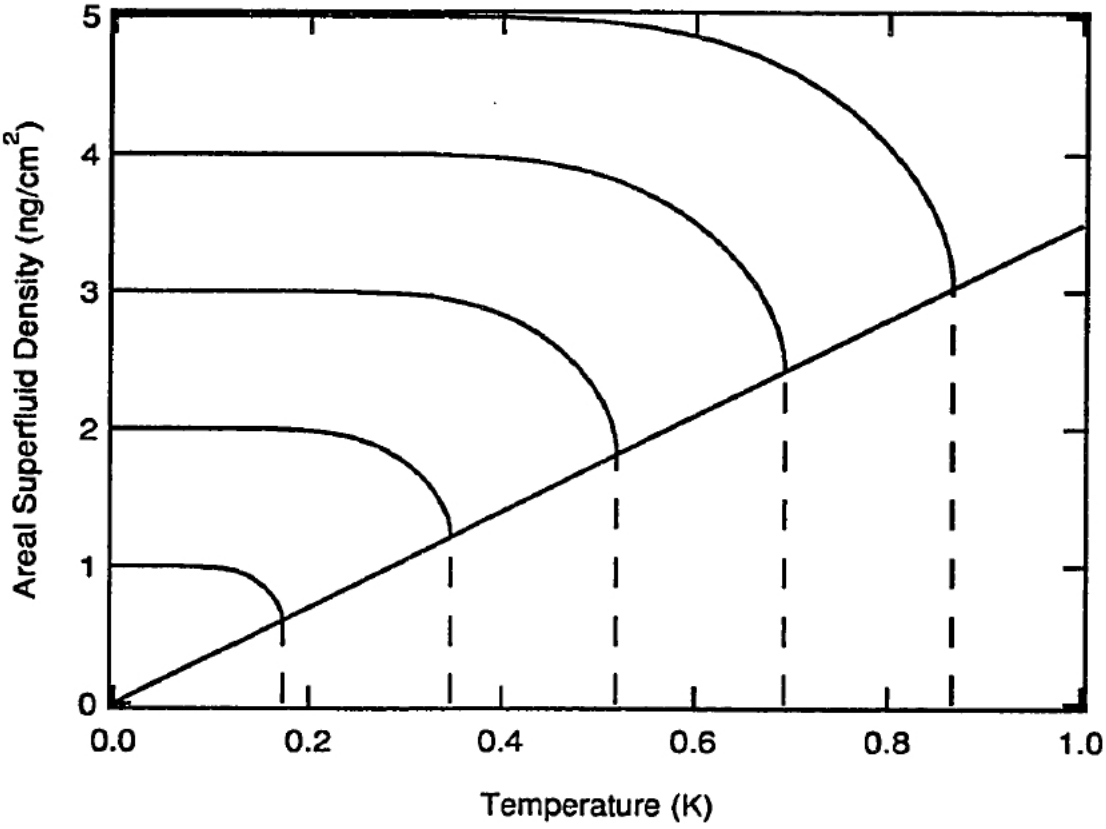

Figure 1.13: **The static KTN theory for various transition temperatures on a flat substrate.** The KTN line, with a slope of 3.49×10^{-9} g/cm$^2 \cdot$K runs through all of the curves right at the point where the abrupt drop in each curve takes place. The curves with a higher value of T_{KT} require a much larger film thickness, as indicated by the larger onset value of the areal superfluid density. The plot is taken from Reference [41] and uses $E_{\mathrm{c}}/K_0 = 2.2$ (in units of $k_{\mathrm{B}}T$).

to work very well. Indeed, such measurements must be run at finite frequency, and this requires a modification of the KT theory. As can be seen from Figure 1.11, there is a more gradual drop in the period shift (and, thus, the superfluid fraction), so that the KT transition under these finite-frequency measurements is broadened. This broadening is well understood theoretically as a finite-frequency effect first discussed by Ambegaokar *et al.* [38]. In this modification, the dielectric function is taken to be frequency dependent

$$\epsilon(r,\omega) = 1 + 4\pi\chi(r,\omega), \tag{1.49}$$

where the frequency-dependent susceptibility may be calculated with the addition of a response function, $g(r,\omega)$, which dictates the way in which vortex pairs respond to the time-varying external flow field with angular frequency ω. In this way, Equation 1.37 gets modified for the dynamical theory in the form

$$\chi(r,\omega) = \int_{a_0}^{r} dr' \Gamma(r')\alpha(r')g(r',\omega). \tag{1.50}$$

The physical reason behind the inclusion of this response function has to do with the fact that the vortex-antivortex pairs, although wanting to polarize against the superflow, will not react instantaneously to an externally applied, time-varying superflow field. Instead, because of the existence of mutual friction between the pairs, pairs of larger separation will have a harder time responding to the alternating superflow. In fact, by solving a Fokker-Planck equation for the diffusive motion of the vortex pairs, a good approximation for the response function was obtained in terms of the vortex diffusion constant, D:

$$g(r,\omega) = \frac{1}{1 - i\frac{\omega r^2}{14D}}. \tag{1.51}$$

The relevant length scale that determines the finite-frequency broadening of the KT transition in this dynamical theory is the vortex diffusion length, r_D, which

is defined as

$$r_D = \sqrt{\frac{14D}{\omega}}. \tag{1.52}$$

In this sense, only pairs with a separation $r < r_D$ can respond to the oscillating flow field, while pairs with a separation $r > r_D$ cannot follow the motion of the drive and, thus, do not contribute to the polarizability. Notice from Equation 1.52 that the larger the driving frequency, the smaller the diffusion length. In essence, this important length scale introduces a cutoff for the KT recursion relations in Equations 1.48, leading to a broadened transition as seen in the experimental data in Figure 1.11.

Along with finite-frequency effects, the KT transition can also be broadened by finite-size effects, which are naturally seen when adsorbing helium onto substrates with geometries that are not necessarily flat. The vortex pairs are constrained to live on the geometry dictated by the substrate. For instance, on a sphere, the vortex pairs cannot be separated to infinity (contrary to the case on a flat substrate) due to the connected nature of the surface. In this sense, a cutoff is introduced into the KT recursion relations, resulting in a broadening of the transition. As mentioned previously, finite-frequency effects are dictated by the vortex diffusion length, r_D. However, if the size of the nominal spherical pore in the substrate is smaller than this diffusion length, then finite-size effects play the crucial role in the broadening. Figure 1.14, taken from Reference [43], showcases this broadening. Note that the superfluid fraction does not abruptly drop to zero in the finite-size-broadened curves. Rather, the decrease is very gradual as can be seen in the dashed tails of the 1 μm and 500 Å curves.

An interesting extension of these ideas is to consider the fact that in a packed powder, the powder grains can be connected to one another via small channels. A simplified model of such a situation is that of a jungle gym, shown in Figure

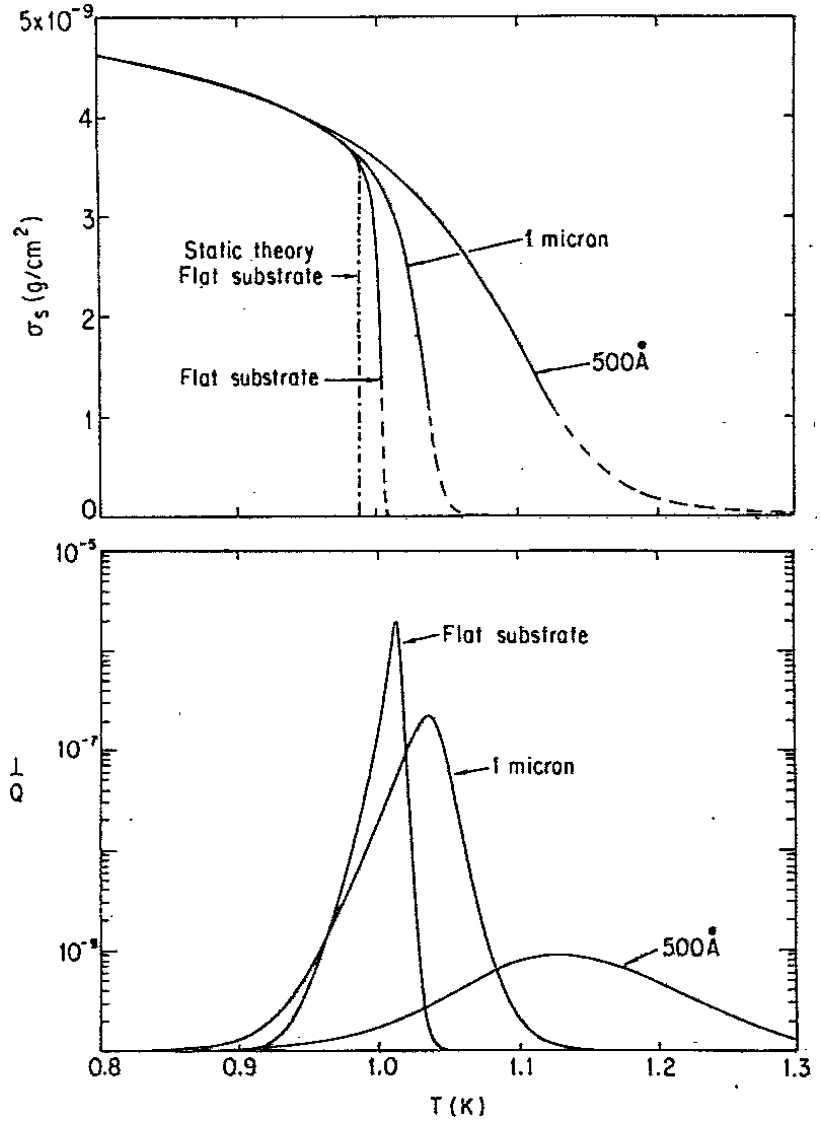

Figure 1.14: **An illustration of finite-size effects in a porous substrate of spherical pores from Reference [43].** The plots showcase the superfluid areal density, σ_s, and the attenuation, Q^{-1}, as functions of the temperature. The dotted-dashed line in the σ_s plot represents the static KT theory. The "flat substrate" curve represents the dynamic KT theory on a flat substrate. The remaining curves represent the KT theory on spheres of diameter 1 μm and 500 Å. Note the spread in the attenuation of the superfluid signal with decreasing pore size. The dashed lines indicate regions for which the assumption of a dilute collection of vortex pairs (used in the calculation of these curves) is no longer valid.

1.15. The goal of such a model was to develop a crossover of the superfluid phase transition from a two-dimensional regime into a three-dimensional one by implementing the notion of vortex strings as the elementary excitation. [44–46] As in the figure, an imaginary line is drawn through the cores of vortex pairs to develop the notion of the vortex string. When sufficiently below the phase transition point, only pairs of very small separation are excited, so that the strings are small in length. The excitation of pairs of such close proximity requires an energy that is logarithmic in the separation. As such, not much energy is required for the excitation of such a pair. However, to create a vortex string that connects a vortex pair by essentially looping around a pore—to which it is referred as a pore vortex in Reference [45]—requires an energy that is linear in the separation. On top of this linear profile, since the separation is already the size of a lattice spacing in the jungle gym, the energy cost is a lot more substantial. Thus, these pore vortices can only be excited at higher temperatures, when there is substantial screening from pairs of smaller separation and sufficient thermal energy. The costliness of exciting these long vortex strings essentially leads to a broadened KT transition. However, the superfluid density does drop more abruptly to zero than in the case of a single, unconnected pore[27] (see Figure 1.16), since these strings can eventually reach an infinite extent at $T_{\mathrm{c}} > T_{\mathrm{KT}}$ when enough thermal energy is present to macroscopically suppress the supercurrent.

The three-dimensional crossover of the KT transition in such multiply connected geometries motivated the promotion of this mechanism to account for the actual bulk-fluid phase transition at the λ point. The idea of this theory is to play on the fundamental importance of vortices in determining the phase transition, as initially suggested by Onsager [24] and Feynman [25]. In essence, the elementary excitation is taken to be vortex rings, which screen an applied superflow by polarizing against the flow with their own backflow (much like in the two-dimensional

[27] As can be seen from the dashed tails in the single-sphere model of the 1 μm and 500 Å curves in Figure 1.14.

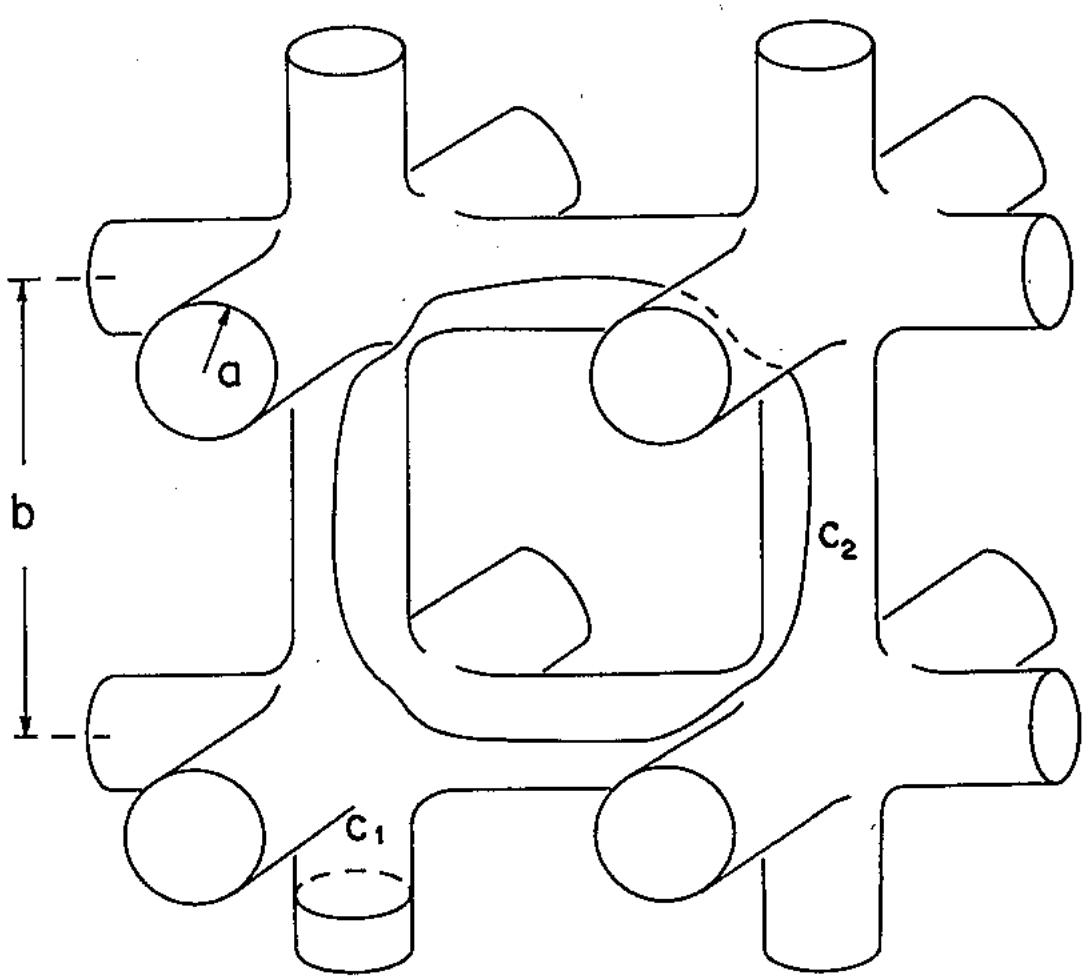

Figure 1.15: **The jungle-gym model of a multiply connected porous material.** In this model, the elementary excitation is taken to be a vortex string that is an imaginary line that runs through the cores of a given vortex-antivortex pair in a closed loop. The curve C_1 represents a vortex string that runs across vortex pairs that are in close proximity to one another. The curve C_2 represents a vortex string that is larger than the lattice spacing. The energy associated with a pair is far more costly for pairs whose separation is larger than the lattice spacing, which introduces a broadening of the KT transition. The diagram is taken from Reference [46].

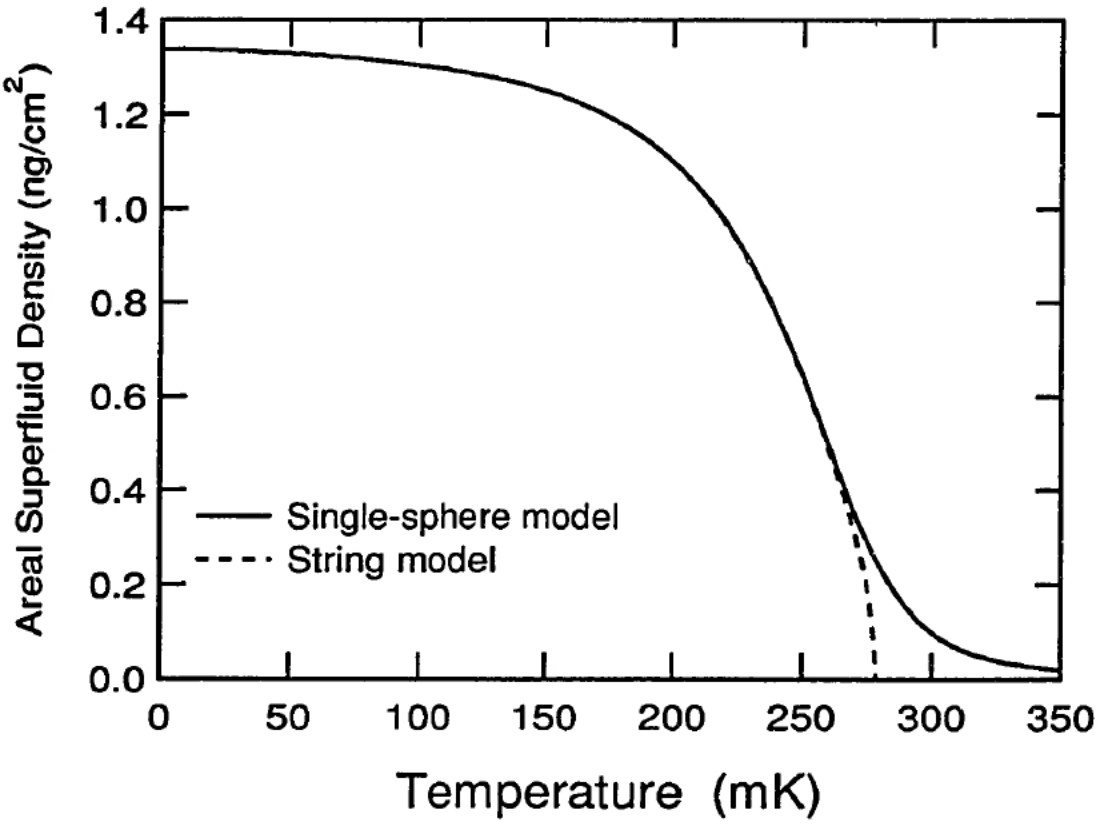

Figure 1.16: **Comparison of the KT transition of the vortex-string model to the single-sphere model.** The two models display the broadening of the KT transition; however, as seen in Figure 1.14, note the rounded tail of the single-sphere model, which showcases the gradual reduction of the superfluid fraction upon approaching T_c. The vortex-string model has a much more abrupt reduction in the superfluid density due to the production of infinite strings. Although the local geometry is limiting, the channels connecting the pore spaces allow for an actual vortex-unbinding transition. The plot is taken from Reference [41].

case). [47] The average diameter of such loops increases upon approaching T_λ from below, while the diameter diverges at the transition temperature. These loops are built up from the smallest of rings.[28] Agreement with these notions has been seen in Type-II superconductors, with a vortex-loop-unbinding transition agreeing with the results of the simulation study. [48]

1.7 Two-Fluid Hydrodynamics

Before discussing sound modes that are present in the two-fluid model of He II, it is important to first develop the fluid equations. Recall, upon including time dependence, that the macroscopic wave function for the superfluid has the form

$$\psi(\vec{r},t) = \psi_0(\vec{r},t)e^{i\theta(\vec{r},t)} = \sqrt{\nu_{\rm s}(\vec{r},t)}e^{i\theta(\vec{r},t)}. \tag{1.53}$$

As such, the condensate wave function must obey a (non-relativistic) time-dependent Schrödinger equation

$$i\hbar\frac{\partial\psi}{\partial t} = -\frac{\hbar^2}{2m^*}\nabla^2\psi + \bar{V}(\vec{r})\psi, \tag{1.54}$$

where m^* is some effective mass, which is related to the ^{4}He mass (m_4), and $\bar{V}(\vec{r})$ is some potential energy that takes into account the interactions between the superfluid particles in some macroscopic sense. As stated before, parameters—such as the phase of the wave function, θ, as well as the superfluid density, $\nu_{\rm s}$—should be slowly varying functions of position[29] so that a thermodynamic approach to the flow of superfluid atoms should be sufficient. In this sense, the average potential energy $\bar{V}(\vec{r})$ is treated as such a thermodynamic function. Surely, not much has been said about this potential as a whole, and some thermodynamics is needed in order to delve further into the properties of this potential energy.

[28] These smallest of rings can be taken as Landau's rotons.

[29] Exceptions include near a vortex core or at a boundary, such as a wall.

In the treatment, this average potential energy should still be present when the superfluid is at rest. So, if a reversible change is applied to this fluid, then the First Law of Thermodynamics states that

$$d\bar{V} = TdS - Pd\mathcal{V} + \mu d\mathcal{N}, \tag{1.55}$$

where T is the temperature, S is the entropy, P is the pressure, $\mathcal{V}$ is the volume, μ is the chemical potential, and $\mathcal{N}$ is the number of particles. These thermodynamic parameters together provide information about the system itself. Notice that the chemical potential is given by the relation

$$\mu = \left(\frac{\partial \bar{V}}{\partial \mathcal{N}}\right)_{S,\mathcal{V}}, \tag{1.56}$$

where the subscripts S and $\mathcal{V}$ next to the parentheses refer to the reminder that the entropy and volume are kept fixed upon taking this derivative relative to particle number.

In order to obtain the total energy of the superfluid, the kinetic energy $\mathcal{T}$ must also be considered, so that the total energy E is given by:

$$E = \mathcal{T} + \bar{V}. \tag{1.57}$$

Since superflow involves no dissipation, then the total energy in a reversible change of the system will remain constant. So, if such a change from a state A to a state B is performed, then using Equation 1.57 it is found that

$$0 = \Delta E = \Delta \mathcal{T} + \left[\left(\frac{\partial \bar{V}}{\partial \mathcal{N}}\right)_{S,\mathcal{V}}^{(\mathrm{B})} - \left(\frac{\partial \bar{V}}{\partial \mathcal{N}}\right)_{S,\mathcal{V}}^{(\mathrm{A})}\right] \Delta \mathcal{N}. \tag{1.58}$$

As a result,

$$\frac{\Delta \mathcal{T}}{\Delta \mathcal{N}} = -\left(\mu^{(\mathrm{B})} - \mu^{(\mathrm{A})}\right), \tag{1.59}$$

which implies that a change in kinetic energy of the superfluid is the direct result of a net flow of superfluid particles in response to an imbalance in chemical potential. In this sense, the chemical potential for a fluid at rest describes the potential energy per particle of the superfluid. Thus, for each superfluid atom, a direct adaptation of Equation 1.54 for this result gives rise to the condensate wave function to obey

$$i\hbar\frac{\partial\psi}{\partial t} = -\frac{\hbar^2}{2m_4}\nabla^2\psi + \mu\psi. \tag{1.60}$$

Using Equation 1.53, one sees that:

$$i\frac{\partial\psi}{\partial t} = e^{i\theta}\left(-\psi_0\frac{\partial\theta}{\partial t} + i\frac{\partial\psi_0}{\partial t}\right),$$

and

$$\nabla^2\psi = e^{i\theta}\left\{\nabla^2\psi_0 - \psi_0\left(\vec{\nabla}\theta\right)^2 + i\left[\psi_0\nabla^2\theta + 2\left(\vec{\nabla}\theta\right)\cdot\left(\vec{\nabla}\psi_0\right)\right]\right\}.$$

Plugging these results into Equation 1.60, one finds:

$$\begin{aligned}\hbar e^{i\theta}\left(i\frac{\partial\psi_0}{\partial t} - \psi_0\frac{\partial\theta}{\partial t}\right) = &-\frac{\hbar^2}{2m_4}e^{i\theta}\left\{\nabla^2\psi_0 - \psi_0\left(\vec{\nabla}\theta\right)^2 + i\left[\psi_0\nabla^2\theta + 2\left(\vec{\nabla}\theta\right)\cdot\left(\vec{\nabla}\psi_0\right)\right]\right\} \\ &+ e^{i\theta}\mu\psi_0.\end{aligned}$$

This equation has both a real part and an imaginary part which decouple into two separate equations. The real part reveals:

$$-\hbar\psi_0\frac{\partial\theta}{\partial t} = -\frac{\hbar^2}{2m_4}\left[\nabla^2\psi_0 - \psi_0\left(\vec{\nabla}\theta\right)^2\right] + \mu\psi_0$$

while the imaginary part reveals:

$$\hbar\frac{\partial\psi_0}{\partial t} = -\frac{\hbar^2}{2m_4}\left[\psi_0\nabla^2\theta + 2\left(\vec{\nabla}\theta\right)\cdot\left(\vec{\nabla}\psi_0\right)\right].$$

Upon rearrangement of the real part and using Equations 1.14 and 1.20, and the fact that the mass density of the superfluid component can be written as

$$\rho_{\rm s} = m_4 \nu_{\rm s}, \tag{1.61}$$

one finds

$$\hbar \frac{\partial \theta}{\partial t} = -\left(\mu + \frac{1}{2} m_4 v_{\rm s}^2\right) + \frac{\hbar^2}{2m_4} \frac{\nabla^2 \left(\sqrt{\rho_{\rm s}}\right)}{\sqrt{\rho_{\rm s}}}. \tag{1.62}$$

Furthermore, if the imaginary part is massaged a bit using Equations 1.14 and 1.20, it is found that:

$$\frac{\partial \psi_0}{\partial t} + \frac{1}{2}\psi_0 \vec{\nabla} \cdot \vec{v}_{\rm s} + \vec{v}_s \cdot \left(\vec{\nabla}\psi_0\right) = 0,$$

so that since

$$\vec{\nabla}\psi_0 = \frac{1}{2}\frac{\vec{\nabla}\nu_{\rm s}}{\sqrt{\nu_{\rm s}}}$$

and

$$\frac{\partial \psi_0}{\partial t} = \frac{1}{\sqrt{\nu_{\rm s}}}\frac{\partial \nu_{\rm s}}{\partial t}$$

then it can be seen that

$$\frac{\partial \nu_{\rm s}}{\partial t} + \vec{\nabla} \cdot (\nu_{\rm s} \vec{v}_{\rm s}) = 0. \tag{1.63}$$

However, multiplying through by m_4 in Equation 1.63 and defining the mass current as

$$\vec{j}_{\rm s} \equiv \rho_{\rm s} \vec{v}_{\rm s}, \tag{1.64}$$

the equation of continuity of the superfluid is then derived[30]:

$$\frac{\partial \rho_{\rm s}}{\partial t} + \vec{\nabla} \cdot \vec{j}_{\rm s} = 0. \tag{1.65}$$

[30]Of course, in the absence of sources and sinks.

In light of previous assumptions, if the superfluid mass density is treated as a slowly varying function over macroscopic distances, the last term on the right-hand side of Equation 1.62 can be neglected. Taking gradients of both sides of this equation and using Equation 1.20, the local rate of change of the superfluid velocity is then given by:

$$m_4 \frac{\partial \vec{v}_{\rm s}}{\partial t} = -\vec{\nabla}\left(\mu + \frac{1}{2} m_4 v_{\rm s}^2\right). \tag{1.66}$$

Noting that

$$\frac{1}{2}\vec{\nabla}\left(v_{\rm s}^2\right) = \frac{1}{2}\left[2\left(\vec{v}_{\rm s}\cdot\vec{\nabla}\right)\vec{v}_{\rm s}\right] = \left(\vec{v}_{\rm s}\cdot\vec{\nabla}\right)\vec{v}_{\rm s},$$

then Equation 1.66 becomes

$$\frac{D\vec{v}_{\rm s}}{Dt} \equiv \frac{\partial \vec{v}_{\rm s}}{\partial t} + \left(\vec{v}_s\cdot\vec{\nabla}\right)\vec{v}_{\rm s} = -\frac{1}{m_4}\vec{\nabla}\mu, \tag{1.67}$$

where the operator D/Dt is called the material (or particle) derivative in fluid mechanics[31]. Equation 1.67 is the equation of motion for the superfluid.

This superfluid equation of motion may be expressed in terms of the pressure and temperature gradients as well. Recall from thermodynamics the Gibbs free energy, defined by the relation

$$G \equiv \mathcal{E} - TS + P\mathcal{V}. \tag{1.68}$$

[31]This derivative comes from elementary fluid mechanics. Fluid mechanics consists of two perspectives: the particle (or Lagrangian) formalism and the field (or Eulerian) formalism. For solving problems, the Eulerian description is the most useful, in which collections of particles are described by some effective particle field. However, in describing the time evolution of a fluid element in the field description one is effectively treating the fluid field as a particle. The correct way to describe this evolution in the Eulerian framework is to introduce the material derivative defined as:

$$\frac{D}{Dt} = \frac{\partial}{\partial t} + (\vec{v}\cdot\nabla)$$

where the first term describes the local rate of change of the fluid element, while the second term describes how the fluid element changes from one spatial location to another (i.e., it describes advection). Here, $\vec{v}$ is the velocity of the fluid element.

Taking differentials of both sides of Equation 1.68 and using the First Law of Thermodynamics, it is then found that

$$dG = \mu d\mathcal{N} - SdT + \mathcal{V}dP, \tag{1.69}$$

from which it can be shown that

$$\mathcal{N}\mu(P,T) = G(\mathcal{N},P,T). \tag{1.70}$$

Achieving a change in μ upon keeping $\mathcal{N}$ fixed, Equation 1.70 reveals that

$$\mathcal{N}d\mu = \left(\frac{\partial G}{\partial P}\right)_{\mathcal{N},T} dP + \left(\frac{\partial G}{\partial T}\right)_{\mathcal{N},P} dT, \tag{1.71}$$

from which (upon use of Equation 1.69) it can be seen that

$$\vec{\nabla}\mu = \frac{\mathcal{V}}{\mathcal{N}}\vec{\nabla}P - \frac{S}{\mathcal{N}}\vec{\nabla}T. \tag{1.72}$$

Upon noting that $\mathcal{N}m_4/\mathcal{V} = \rho$ is the total fluid density and

$$s \equiv \frac{S}{\mathcal{N}m_4} \tag{1.73}$$

is the specific entropy (i.e., entropy per unit mass), then Equation 1.67 reads

$$\frac{D\vec{v}_{\rm s}}{Dt} = -\frac{1}{m_4}\vec{\nabla}\mu = -\frac{1}{\rho}\vec{\nabla}P + s\vec{\nabla}T. \tag{1.74}$$

So far only the equations that govern the superfluid have been considered. Of course, in this two-fluid hydrodynamics, the normal-fluid component must also be factored into the mix. The total mass current (containing both superfluid and normal-fluid components) is given by

$$\vec{j} = \rho_{\rm s}\vec{v}_{\rm s} + \rho_{\rm n}\vec{v}_{\rm n}, \tag{1.75}$$

and the total density is given by Equation 1.9. By the principle of the conservation of mass, it is known that $\vec{j}$ and ρ must necessarily satisfy a continuity equation:

$$\frac{\partial \rho}{\partial t} + \vec{\nabla} \cdot \vec{j} = 0. \tag{1.76}$$

Furthermore, the normal fluid is the component that carries the entropy in the fluid. Of course, entropy may be generated by the inherent viscosity in the normal component. However, if the velocity of the normal fluid is kept low, then this entropic contribution is negligible. Therefore, in this low-velocity limit[32], a continuity equation for the entropy may also be written down, since the total entropy of the system is conserved due to the reversible nature of the normal-fluid and superfluid flow in this limit. Noting that the entropy density is given by ρs and, thus, the entropy current density is given by $\rho s \vec{v}_{\mathrm{n}}$ (since the normal fluid carries the entropy), then the equation for the conservation of entropy reads:

$$\frac{\partial (\rho s)}{\partial t} + \vec{\nabla} \cdot (\rho s \vec{v}_{\mathrm{n}}) = 0. \tag{1.77}$$

The final piece of the puzzle is to discuss how the mass-current gets accelerated. In the low-velocity limit, a Navier-Stokes equation may be employed[33]. If it is assumed that the flow of the liquid is incompressible (i.e., the normal-fluid and superfluid densities do not depend on position), then

$$\frac{D}{Dt} (\rho_{\mathrm{s}} \vec{v}_{\mathrm{s}} + \rho_{\mathrm{n}} \vec{v}_{\mathrm{n}}) = \frac{D\vec{j}}{Dt} = -\vec{\nabla} P, \tag{1.78}$$

which qualitatively states that gradients in pressure dictate a change in the mass-current flow properties.[34]

[32] If this limit is not taken, then one must also be concerned about thermal dissipation due to viscosity, which occurs at a rate proportional to $\vec{\nabla} \left(v_\nu^2 \right)$, with ν the total number density.

[33] Navier-Stokes equations arise from applying Newton's Second Law to a fluid element in order to describe the time evolution of flow. Accelerations of such flows are given by pressure gradients.

[34] If the low-velocity limit was not taken, then one would need to include thermal losses due to

In summary, the following four equations describe the two-fluid hydrodynamics of He II in the low-velocity limit:

$$\frac{D\vec{v}_{\rm s}}{Dt} = -\frac{1}{m_4}\vec{\nabla}\mu \tag{1.79a}$$

$$= -\frac{1}{\rho}\vec{\nabla}P + s\vec{\nabla}T \tag{1.79b}$$

$$\frac{D}{Dt}\left(\rho_{\rm s}\vec{v}_{\rm s} + \rho_{\rm n}\vec{v}_{\rm n}\right) = -\vec{\nabla}P \tag{1.79c}$$

$$\frac{\partial\left(\rho s\right)}{\partial t} + \vec{\nabla}\cdot\left(\rho s\vec{v}_{\rm n}\right) = 0 \tag{1.79d}$$

$$\frac{\partial}{\partial t}\left(\rho_{\rm s} + \rho_{\rm n}\right) + \vec{\nabla}\cdot\left(\rho_{\rm s}\vec{v}_{\rm s} + \rho_{\rm n}\vec{v}_{\rm n}\right) = 0. \tag{1.79e}$$

1.8 Sound Modes in Superfluid Helium

The interplay between the normal-fluid and superfluid components of He II leads to rather exotic types of sound waves. In this section, the wave equations for first, second, and third sound will be developed from the Hydrodynamic Equations 1.79 obtained in Section 1.7. The existence of fourth and fifth sound will also be discussed, but without much rigor.

To begin, it is fitting to extract a more useful form for Equations 1.79b and 1.79c. Assuming low-enough velocities—in order to avoid dissipative terms as well as nonlinear turbulence corrections—multiplying through by $\rho_{\rm s}$ in Equation 1.79b, results in the following relation:

$$\rho_{\rm s}\frac{D\vec{v}_{\rm s}}{Dt} = -\frac{\rho_{\rm s}}{\rho}\vec{\nabla}P + \rho_{\rm s}s\vec{\nabla}T. \tag{1.80}$$

Subtracting this relation from Equation 1.79c, a similar equation is obtained for (essentially) the normal fluid:

the viscous nature of the normal fluid. In this case, a term of the form $\eta_{\rm n}\nabla^2\vec{v}_{\rm n}$ must be added to the right-hand side of Equation 1.78. Here, $\eta_{\rm n}$ represents the normal-fluid viscosity.

$$\rho_{\rm n}\frac{D\vec{v}_{\rm n}}{Dt} = -\frac{\rho_{\rm n}}{\rho}\vec{\nabla}P + \rho_{\rm s}s\vec{\nabla}T. \tag{1.81}$$

In deriving the first- and second-sound modes, nonlinear effects are neglected. Thus, the appropriate approximations are made for the application of linear acoustics[35] and the advective term in the material derivative of the normal-fluid and superfluid velocities is thrown away (as this term is inherently nonlinear). So, the following sets of equations define the beginning of the derivation of these sound modes:

$$\rho_{\rm s}\frac{\partial\vec{v}_{\rm s}}{\partial t} = -\frac{\rho_{\rm s}}{\rho}\vec{\nabla}P + \rho_{\rm s}s\vec{\nabla}T \tag{1.82a}$$

$$\rho_{\rm n}\frac{\partial\vec{v}_{\rm n}}{\partial t} = -\frac{\rho_{\rm n}}{\rho}\vec{\nabla}P + \rho_{\rm s}s\vec{\nabla}T \tag{1.82b}$$

$$\frac{\partial(\rho s)}{\partial t} + \vec{\nabla}\cdot(\rho s\vec{v}_{\rm n}) = 0 \tag{1.82c}$$

$$\frac{\partial}{\partial t}(\rho_{\rm s}+\rho_{\rm n}) + \vec{\nabla}\cdot(\rho_{\rm s}\vec{v}_{\rm s}+\rho_{\rm n}\vec{v}_{\rm n}) = 0. \tag{1.82d}$$

In what follows, the assumption of incompressibility will be relaxed, because density gradients will actually play a crucial role in deriving the desired sound modes. Adding Equations 1.82a and 1.82b, upon neglecting terms like $\vec{v}_{\rm i}(\partial\rho_{\rm i}/\partial t)$ (for ${\rm i} = {\rm s}, {\rm n}$)[36] so that

$$\rho_{\rm i}\frac{\partial\vec{v}_{\rm i}}{\partial t} = \frac{\partial(\rho_{\rm i}\vec{v}_{\rm i})}{\partial t} - \vec{v}_{\rm i}\frac{\partial\rho_{\rm i}}{\partial t} \approx \frac{\partial(\rho_{\rm i}\vec{v}_{\rm i})}{\partial t}, \tag{1.83}$$

this approximation scheme then leads to

[35] In other words, one writes $\rho = \rho_0 + \delta\rho$, $s = s_0 + \delta s$, $P = P_0 + \delta P$, $T = T_0 + \delta T$ where $\delta x \ll x$.

[36] Since

$$\vec{v}_{\rm i}\frac{\partial\rho_{\rm i}}{\partial t} = \vec{v}_{\rm i}\frac{\partial(\rho_{0{\rm i}}+\delta\rho_{\rm i})}{\partial t} = \vec{v}_{\rm i}\frac{\partial\rho_{0{\rm i}}}{\partial t} + \vec{v}_{\rm i}\frac{\partial(\delta\rho_{\rm i})}{\partial t} = \vec{0} + \vec{v}_{\rm i}\frac{\partial(\delta\rho_{\rm i})}{\partial t} = \vec{v}_{\rm i}\frac{\partial(\delta\rho_{\rm i})}{\partial t}$$

is negligibly small for the chosen approximation scheme.

$$\frac{\partial \vec{j}}{\partial t} = -\vec{\nabla} P. \tag{1.84}$$

Taking divergences of both sides of Equation 1.84 and substituting in the mass-conservation equation (Equation 1.82d), one finds:

$$\frac{\partial^2 \rho}{\partial t^2} = \nabla^2 P. \tag{1.85}$$

Now, to make further progress, solve for $\vec{\nabla} P$ in Equation 1.82a and plug into Equation 1.84 to obtain

$$\frac{\partial \vec{j}}{\partial t} = \rho \frac{\partial \vec{v_{\rm s}}}{\partial t} - \rho s \vec{\nabla} T.$$

Then, upon utilizing the approximation in Equation 1.83, it is found that

$$\rho_{\rm n} \frac{\partial}{\partial t} \left(\vec{v}_{\rm n} - \vec{v}_{\rm s} \right) = -\rho s \vec{\nabla} T. \tag{1.86}$$

Notice from Equation 1.86 that a temperature gradient is able to set up relative motion between the two fluids that changes in time. Furthermore, combining Equations 1.82c and 1.82d, and neglecting second-order terms in the same way as done before, one also arrives at the equation:

$$\vec{\nabla} \cdot \left(\vec{v}_{\rm n} - \vec{v}_{\rm s} \right) = -\frac{\rho}{\rho_{\rm s} s} \frac{\partial s}{\partial t}, \tag{1.87}$$

which, upon combination with Equation 1.86 results in the following equation:

$$\frac{\partial^2 s}{\partial t^2} = \frac{\rho_{\rm s}}{\rho_{\rm n}} s^2 \nabla^2 T. \tag{1.88}$$

If one now expresses the pressure and temperature as functions of entropy and density

$$dP = \left(\frac{\partial P}{\partial \rho} \right)_s d\rho + \left(\frac{\partial P}{\partial s} \right)_\rho ds$$

$$dT = \left(\frac{\partial T}{\partial \rho}\right)_s d\rho + \left(\frac{\partial T}{\partial s}\right)_\rho ds,$$

then Equations 1.85 and 1.88 become:

$$\frac{\partial^2 \rho}{\partial t^2} = \left(\frac{\partial P}{\partial \rho}\right)_s \nabla^2 \rho + \left(\frac{\partial P}{\partial s}\right)_\rho \nabla^2 s \tag{1.89a}$$

$$\frac{\partial^2 s}{\partial t^2} = \frac{\rho_\mathrm{s}}{\rho_\mathrm{n}} s^2 \left[\left(\frac{\partial T}{\partial \rho}\right)_s \nabla^2 \rho + \left(\frac{\partial T}{\partial s}\right)_\rho \nabla^2 s\right] \tag{1.89b}$$

which may be solved upon looking for plane-wave solutions of the form:

$$\rho = \bar{\rho} + \rho' e^{i\omega(t - z/c)} \tag{1.90}$$

$$s = \bar{s} + s' e^{i\omega(t - z/c)} \tag{1.91}$$

Here, the wave has been chosen to propagate in the z direction[37], with c the speed of propagation and ω the angular frequency of propagation. Defining

$$c_1^2 \equiv \left(\frac{\partial P}{\partial \rho}\right)_s \tag{1.92a}$$

$$c_2^2 \equiv \frac{\rho_\mathrm{s}}{\rho_\mathrm{n}} s^2 \left(\frac{\partial T}{\partial s}\right)_\rho \tag{1.92b}$$

then, upon plugging in the plane wave solutions into Equations 1.89, the following equations, which must be solved simultaneously, are obtained:

$$\begin{array}{l} \left[\left(\frac{c}{c_1}\right)^2 - 1\right] \rho' - \left(\frac{\partial P}{\partial s}\right)_\rho \left(\frac{\partial \rho}{\partial P}\right)_s s' = 0 \\ \left(\frac{\partial T}{\partial \rho}\right)_s \left(\frac{\partial s}{\partial T}\right)_\rho \rho' - \left[\left(\frac{c}{c_2}\right)^2 - 1\right] s' = 0 \end{array}, \tag{1.93}$$

[37]Transverse waves cannot propagate in a fluid because there simply is no mechanism for driving motion perpendicular to the propagation of the wave. Indeed, in the case of ordinary sound waves propagating in air, it is absolutely nonsensical to imagine such a sound wave propagating in a particular direction but creating density fluctuations in the perpendicular direction. Thus, a direction is simply picked for the propagation of the sound wave in the liquid helium.

or, in matrix form:

$$\begin{pmatrix} \left[\left(\frac{c}{c_1}\right)^2 - 1\right] & -\left(\frac{\partial P}{\partial s}\right)_\rho \left(\frac{\partial \rho}{\partial P}\right)_s \\ \left(\frac{\partial T}{\partial \rho}\right)_s \left(\frac{\partial s}{\partial T}\right)_\rho & -\left[\left(\frac{c}{c_2}\right)^2 - 1\right] \end{pmatrix} \begin{pmatrix} \rho' \\ s' \end{pmatrix} = \begin{pmatrix} 0 \\ 0 \end{pmatrix}. \tag{1.94}$$

A solution exists for Equation 1.94 if and only if

$$\det \begin{pmatrix} \left[\left(\frac{c}{c_1}\right)^2 - 1\right] & -\left(\frac{\partial P}{\partial s}\right)_\rho \left(\frac{\partial \rho}{\partial P}\right)_s \\ \left(\frac{\partial T}{\partial \rho}\right)_s \left(\frac{\partial s}{\partial T}\right)_\rho & -\left[\left(\frac{c}{c_2}\right)^2 - 1\right] \end{pmatrix} = 0. \tag{1.95}$$

Performing this determinant, one finds:

$$\left[\left(\frac{c}{c_1}\right)^2 - 1\right]\left[\left(\frac{c}{c_2}\right)^2 - 1\right] = \left(\frac{\partial P}{\partial s}\right)_\rho \left(\frac{\partial \rho}{\partial P}\right)_s \left(\frac{\partial T}{\partial \rho}\right)_s \left(\frac{\partial s}{\partial T}\right)_\rho. \tag{1.96}$$

Recognizing that the right-hand side of Equation 1.96 (with $\mathcal{C}_P$ and $\mathcal{C}_\mathcal{V}$ the specific heat capacities at constant pressure and constant volume, respectively) is given by

$$\left(\frac{\partial P}{\partial s}\right)_\rho \left(\frac{\partial \rho}{\partial P}\right)_s \left(\frac{\partial T}{\partial \rho}\right)_s \left(\frac{\partial s}{\partial T}\right)_\rho = \frac{\mathcal{C}_P - \mathcal{C}_\mathcal{V}}{\mathcal{C}_P},$$

and the fact that these specific heats are very nearly equal to each other in He II, one may write:

$$\left[\left(\frac{c}{c_1}\right)^2 - 1\right]\left[\left(\frac{c}{c_2}\right)^2 - 1\right] \approx 0. \tag{1.97}$$

As a result of Equation 1.97, it can then be seen that what was defined as c_1 and c_2 in Equations 1.92 are in fact the sound speeds that solve the matrix equation (Equation 1.94). Incidentally, the first-sound speed is given by

$$c_1 = \sqrt{\left(\frac{\partial P}{\partial \rho}\right)_s}, \tag{1.98}$$

while, upon recognizing the fact that

$$\mathcal{C}_P = T\left(\frac{\partial s}{\partial T}\right)_\rho,$$

the second-sound speed is given by

$$c_2 = \sqrt{\frac{\rho_\mathrm{s}}{\rho_\mathrm{n}}\frac{Ts^2}{\mathcal{C}_P}}. \tag{1.99}$$

First sound corresponds to the propagation of waves as seen in sound waves (namely, pressure and density oscillations in the fluid). This sound mode has the normal-fluid and superfluid components oscillating in phase. However, second sound is vastly more exotic, because it is actually a temperature wave that relies on the superfluid to normal-fluid ratio. Incidentally, second sound is killed at the lambda point due to the fact that the superfluid density goes to zero when approaching T_λ from below (i.e., from lower temperatures). This sound mode has the normal-fluid and superfluid components oscillating out of phase. Because of this and the consequences of Figure 1.7, where there is a net inflow of superfluid, the temperature is lower; where there is a net outflow of superfluid, the temperature is higher. Indeed, it is because of this that second-sound is actually a temperature wave in the bulk fluid. This property is rather extraordinary, as classical fluids cannot support temperature waves due to the diffusive nature of heat transport in such systems. The existence of second-sound is but one of the many properties of superfluidity that truly showcases liquid helium's nature as a quantum fluid.

There also exist more exotic sound modes. Fourth sound is a manifestation of first sound when the normal fluid is completely immobilized. This may be done by exciting pressure oscillations in He II inside a container filled with a packed powder. [49] The minuscule capillaries present in the packed powder only allow for oscillations in the superfluid fraction, while the normal-fluid fraction remains viscously clamped. The speed of fourth sound is given by

$$c_4 = \sqrt{\frac{\rho_s}{\rho}} c_1. \tag{1.100}$$

Again, the fourth-sound speed goes to zero at the λ point due to the presence of the superfluid fraction in Equation 1.100, which itself goes to zero at T_λ.[38] Fifth sound is what fourth sound becomes when pressure oscillations become forbidden (see Footnote 38). Its speed is given by:

$$c_5 = \sqrt{\frac{\rho_n}{\rho}} c_2. \tag{1.101}$$

Fifth sound can be detected if a cell is only partially filled with helium. [50] Notice that the fifth-sound speed also goes to zero since the second-sound speed goes to zero upon approaching T_λ. Figure 1.17 summarizes how these sound speeds vary as functions of the temperature. For further discussion of first, second, fourth, and fifth sound, see Reference [51].

The final sound mode of interest is third sound, which solely involves the propagation of the superfluid fraction in a thin film of liquid helium adsorbed onto a substrate. The simplest case of third-sound propagation occurs on a completely flat substrate. A schematic of the mechanism behind third sound propagation is displayed in Figure 1.18.

The normal fluid remains viscously clamped to the substrate because the film thickness of the helium film is much, much smaller than the viscous penetration depth. As a result, only the superfluid fraction is allowed to move. However, as mentioned in the latter part of Section 1.6, a superfluid film can only be supported once a critical film thickness is achieved at a given temperature. In other words, in the ideal case of a flat substrate with a static flow, the temperature of the

[38] Actually, this is not quite correct. The fourth-sound speed is given by

$$c_4 = \sqrt{\frac{\rho_s}{\rho} c_1^2 + \frac{\rho_n}{\rho} c_2^2},$$

so that it also depends on the normal-fluid fraction and the speed of second sound.

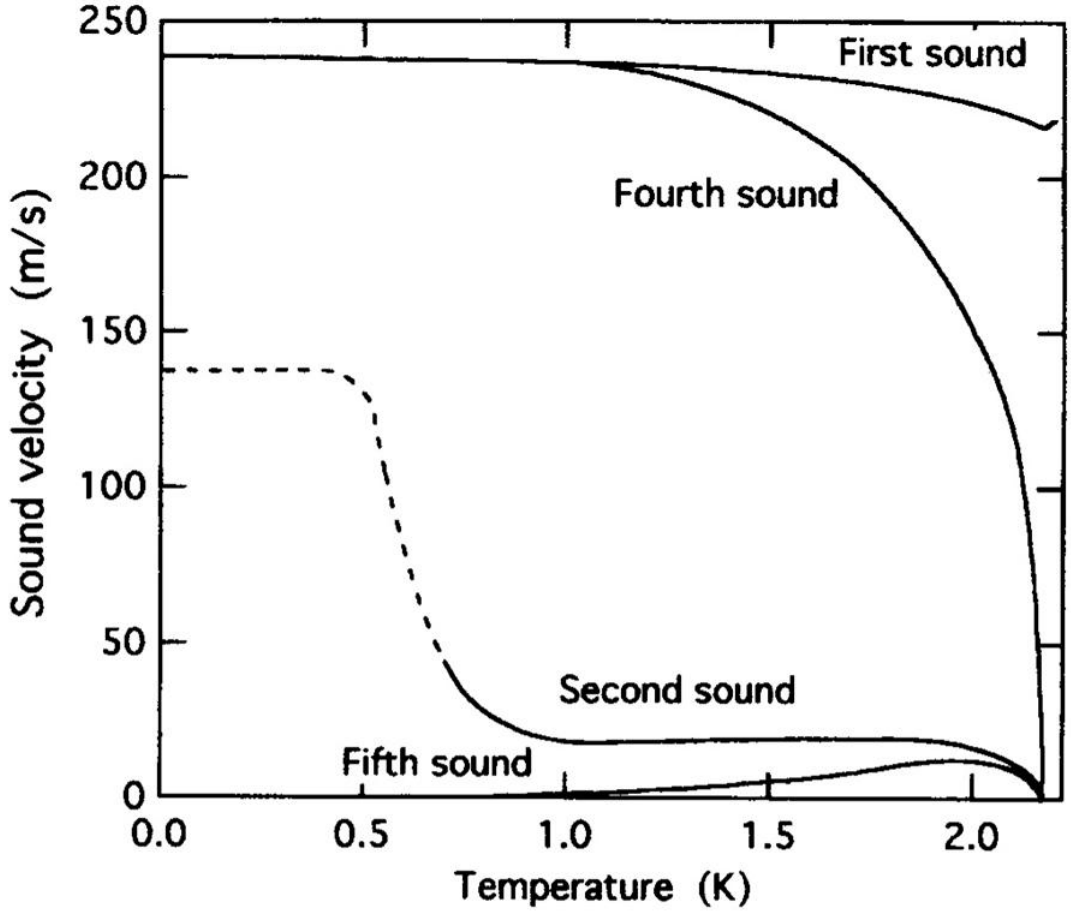

Figure 1.17: **Speeds of the various sound modes of He II as functions of the temperature.** Note that all of the sound modes go to zero at the λ point except for first sound. However, there is a kink in the first-sound speed at T_λ, which is a signature of the continuous phase transition that takes place in the bulk fluid, as the discontinuity occurs when one more derivative is taken with respect to the temperature when approaching the transition temperature. The speed of second sound is dashed below about 0.8 K because it is unobservable in practice. [51]

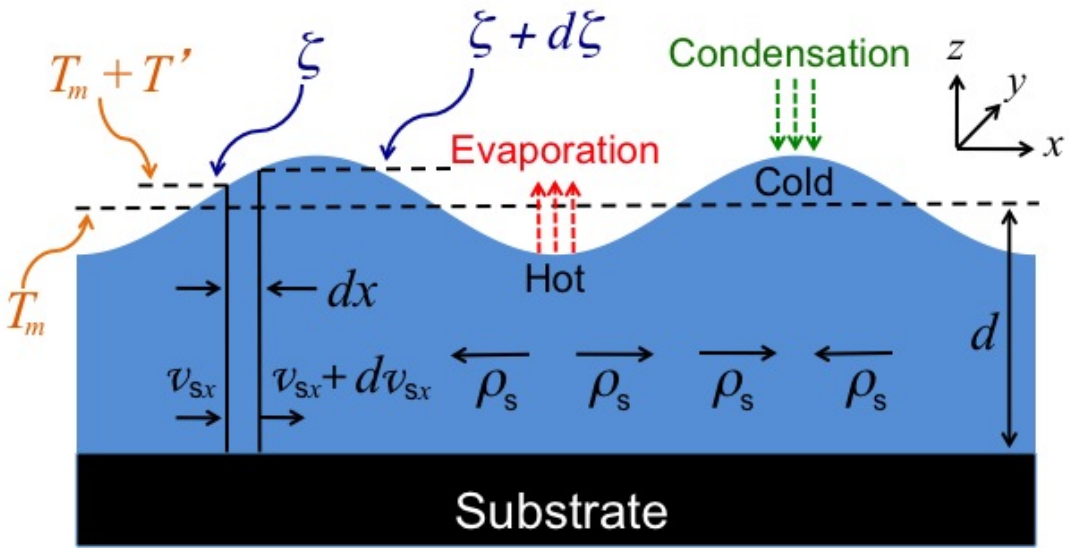

Figure 1.18: **Third-sound propagation in a thin film of helium adsorbed on a flat substrate.** The superfluid component is the only component that can move, since the normal component is viscously clamped to the substrate. In other words, the viscous penetration depth is much larger than the film depth, so that propagation of the normal fluid parallel to the substrate is forbidden. It is assumed that $\zeta \ll d$. The mean temperature is denoted T_m, and the temperature at film thickness ζ is $T_m + T'$.

film must be below T_{KT} for the particular film thickness under question if such a surface wave is to be detected.[39]

Recall from classical fluid mechanics that a shallow-water wave has a propagation speed that depends only on the gravitational acceleration (i.e., the derivative of the gravitational potential with respect to distance), g, and the depth of the water, d. When the wavelength of the surface wave becomes appreciably small, surface-tension effects must also be considered, so that the speed of the shallow-water wave becomes

$$c_{\mathrm{w}} = \sqrt{\frac{g}{k} + k\sigma_{\mathrm{w}}\rho_{\mathrm{w}}}\,\tanh(kd), \tag{1.102}$$

where $k = 2\pi/\lambda$ is the wave number, σ_{w} is the surface tension of water, and ρ_{w} is the (mass) density of water. In the long-wavelength limit, one can Taylor-expand the hyperbolic-tangent function and ignore the surface-tension contribution. In such a case, Equation 1.102 gets vastly simplified:

$$c_{\mathrm{w}} = \sqrt{gd}. \tag{1.103}$$

For superfluid helium, Equation 1.103 gets slightly modified in this long-wavelength limit due to a necessary dependence on the superfluid fraction. It has been pointed out that in a thin film of helium, it is not the gravitational force that acts as the restoring force, but rather the forces responsible for the formation of the film. [52] The primary potential that is responsible for thin films of helium is the van der Waals (vdW) potential. For a flat substrate, the vdW force (per unit mass) is given by

[39] When finite-frequency and/or finite-size effects are prevalent, a signal can be obtained above T_{KT} due to the rounding of the transition. Under these circumstances, the temperature must be below T_{c}, which is the transition temperature for the presence of a superfluid fraction in the film.

$$\mathcal{F}_{\text{vdw}} = \left[\frac{\partial}{\partial\zeta}\left(-\frac{\alpha}{\zeta^3}\right)\right]_{\zeta=d}, \tag{1.104}$$

where the normal direction to the substrate is labeled by ζ. Here, α is a constant that is dependent on the substrate material. The larger the value of α, the stronger the vdW bond between the helium atoms and the substrate. Furthermore, the superfluid fraction gets tacked on to the adaptation of Equation 1.103 for third sound in superfluid helium.

Although such an adaptation seems simple enough, the actual third-sound wave is not only a thickness wave, but also a temperature wave. Just as in the discussion of fourth sound before, in regions where there is a net inflow of superfluid (i.e., where there is a mound in Figure 1.18), the local temperature is lower because of the consequences of Figure 1.7.[40] However, where there is a net ouflow of superfluid (i.e., where there is a valley in Figure 1.18) in a specific region, then the local temperature is higher because the superfluid fraction in that region is lower. Thus, the peaks of the thickness wave are cold while the troughs of the wave are hot. This is why third sound is also a temperature oscillation.

Not only is third sound different than shallow-water waves in this manner, it is also different in the sense that there is not only a restoring force due to just pressure differences, but also a restoring force due to thermal gradients. As can be seen from Figure 1.18, where the superfluid flows the temperature is actually colder. This is very different from a classical fluid, which will typically flow from cold regions to hot regions (as dictated by the Second Law of Thermodynamics).[41] This peculiarity in the superfluid flowing from hot regions to cold regions is known as the thermomechanical effect. However, note that this in itself also contributes

[40] Remember, the normal fluid is viscously clamped, so that a local maximum in the thickness of the film necessarily contains more superfluid than a local minimum. With a larger superfluid fraction, the temperature is lower in such mounds.

[41] However, there is no inherent violation of this law, as the superfluid carries no entropy, so that such a process is ideally a reversible process.

to a restoring force, as mounds will eventually turn into valleys with the outflow of the superfluid fraction from a mounded region.

Moreover, at temperatures where the vapor pressure is appreciable (typically around or above 1 K), there is an inherent attenuation of the wave. Indeed, note that since the valleys in Figure 1.18 are the hottest region in the film, there is more evaporation of the film from those regions. Also, since the peaks are the coldest regions, there is a heightened amount of condensation that takes place there. This will cause a decay in the sound propagation.

So far, the discussion about third sound has been strictly qualitative. To make things more quantitative, a derivation of this sound speed is desired. The derivation follows the work of Atkins [49]. It will be assumed that the thickness oscillations are small amplitude[42] so that nonlinear effects are negligible. The picture that will be used in this derivation is Figure 1.18, in which the chosen coordinate system has the superfluid propagating along the x axis. The motion will be symmetric at any value of y, so that, for the sake of convenience, the analysis of fluid elements will assume a unit length in that direction.

The rate of evaporation of the film, $dm/dt = \dot{m}$, is given (in units of g/s) by [53]

$$\dot{m} = \varepsilon \sqrt{\frac{M_4}{2\pi RT}} \left(\frac{dP}{dT} \right)_{\text{v.p.c.}} T' = kT', \tag{1.105}$$

where $\varepsilon \approx 1$ is the evaporation coefficient, M_4 is the molecular mass of ^{4}He, $R = 8.31 \times 10^7$ erg/mol$\cdot$K is the gas constant, and $(dP/dT)_{\text{v.p.c.}}$ is the slope of the ^{4}He vapor-pressure curve. Here, the factor k has absorbed everything but the temperature fluctuation T', which is taken relative to the mean temperature T_m. Upon looking at the slab of infinitesimal length dx and including the evaporation rate $\dot{m}$, the conservation of mass requires

[42] In other words, the deviation in the thickness is much, much smaller than the film thickness.

$$\rho\frac{\partial\zeta}{\partial t}+\rho_{\mathrm{s}}d\frac{\partial v_{\mathrm{s}x}}{\partial x}+kT'=0, \tag{1.106}$$

where, on the left-hand side, the first term looks at the variation of the film thickness as a function of time, while the second and third terms describe that thickness variation, respectively, as being caused by a flux of superfluid entering or exiting the region and by a loss or gain of film from evaporation or condensation effects. Moreover, because of the temperature difference across regions, a heat-flow analysis must also be done on the slab. With $\mathcal{C}$ the specific heat of the fluid and L the specific latent heat of vaporization, this analysis leads to

$$\rho\mathcal{C}d\frac{\partial T'}{\partial t}-\rho_{\mathrm{s}}d\frac{\partial v_{\mathrm{s}x}}{\partial x}sT+kLT'=0, \tag{1.107}$$

where, on the left-hand side, the first term looks at temperature variations in the slab as a function of time, while the second and third terms describe that temperature variation, respectively, as being caused by variations of the superfluid fraction as the supercurrent flows into or out of a region and by heat flow into or out of the film as the film evaporates or undergoes condensation. Finally, because of the free surface in the film, there is a pressure-release boundary condition that provides a description of the pressure change at a point within the film as

$$\delta P=\left(\frac{dP}{dT}\right)_{\text{v.p.c.}}T'+\rho\mathcal{F}_{\mathrm{vdw}}\zeta=\gamma T'+\rho\mathcal{F}_{\mathrm{vdw}}\zeta, \tag{1.108}$$

where, on the right-hand side, the first term looks at the pressure change on account of the changing temperature (using the vapor pressure curve γ), while the second term comes from the vdW potential set forth by the substrate.

From the linearized hydrodynamic equation describing the acceleration of the superfluid component (Equation 1.82a), one finds:

$$\begin{aligned}\frac{\partial \vec{v}_{\mathrm{s}}}{\partial t} &= -\frac{1}{\rho}\vec{\nabla}P + s\vec{\nabla}T \\ \frac{\partial v_{\mathrm{s}x}}{\partial t} &= -\frac{1}{\rho}\frac{\partial(\delta P)}{\partial x} + s\frac{\partial T'}{\partial x} \\ &= -\frac{1}{\rho}\left(\gamma\frac{\partial T'}{\partial x} + \rho\mathcal{F}_{\mathrm{vdw}}\frac{\partial \zeta}{\partial x}\right) + s\frac{\partial T'}{\partial x},\end{aligned}$$

where the third line follows from using Equation 1.108. Rearranging the terms in this line, the time variation in the superfluid velocity may be written as

$$\frac{\partial v_{\mathrm{s}x}}{\partial t} = -\mathcal{F}_{\mathrm{vdw}}\frac{\partial \zeta}{\partial x} + \left(s - \frac{\gamma}{\rho}\right)\frac{\partial T'}{\partial x}. \tag{1.109}$$

Assuming plane-wave solutions[43] for $v_{\mathrm{s}x}$, ζ, and T', and plugging this ansatz into Equations 1.106, 1.107, and 1.109, the phase speed of the traveling wave, known as the third-sound speed $c_3 \equiv \omega/k$, must then satisfy the following equation:

$$c_3^2 = \frac{\rho_{\mathrm{s}}}{\rho}\mathcal{F}_{\mathrm{vdw}}d + \frac{\rho_{\mathrm{s}}}{\rho}sT\left[\frac{\left(s - \frac{\gamma}{\rho}\right) - i\frac{k\mathcal{F}_{\mathrm{vdw}}}{\rho\omega}}{\mathcal{C} - i\frac{kL}{\rho\omega d}}\right].$$

Although the bulk fluid density ρ_{s} has consistently been used throughout this derivation, it is more correct to consider the average of this superfluid density across the film thickness $\langle\rho_{\mathrm{s}}\rangle$. So, the substitution $\rho_{\mathrm{s}} \to \langle\rho_{\mathrm{s}}\rangle$ is made, as this takes into account nonuniform variations of the superfluid density near the boundaries (due to healing effects), as well as the fact that the entire film is not a liquid. Taking the evaporation coefficient $\varepsilon = 1$, then the imaginary terms in the numerator and denominator are large compared to the real terms if the angular frequency $\omega \lesssim 10^3$ rad/s. Under such circumstances, the third-sound speed becomes

[43] In other words, for $\Xi = \Xi(x)$, a traveling wave solution of the form

$$\Xi(x) = \Xi_0 e^{i(kx-\omega t)}.$$

$$c_3^2 = \frac{\langle \rho_s \rangle}{\rho} \mathcal{F}_{\text{vdw}} d \left(1 + \frac{sT}{L} \right). \tag{1.110}$$

In this study, the entropy term in Equation 1.110 is small in the range of temperatures considered. For example, at 1.5 K, $sT/L \approx 0.01$ and decreases with decreasing temperature. It is effectively zero around 1 K since the superfluid fraction carries no entropy and is practically unity at such temperatures, as shown in Figure 1.7. Thus, the third-sound speed for a helium film adsorbed on a flat substrate at sufficiently low temperatures is given by

$$c_3^2 = \frac{\langle \rho_s \rangle}{\rho} \mathcal{F}_{\text{vdw}} d. \tag{1.111}$$

The film-thickness-averaged superfluid density, $\langle \rho_s \rangle$, may be written in terms of the bulk density, ρ_s [54] as

$$\langle \rho_s \rangle = \rho_s \left(1 - \frac{D_{\text{dead}}}{d} \right), \tag{1.112}$$

where D_{dead} is known as the dead layer, which is the part of the film that is not superfluid. Indeed, the pressures for the initially adsorbed helium atoms are larger than 25 atm on account of the dependence of the vdW potential on the cube of the distance from the substrate. Thus, the helium nearest to the substrate should be in its solid state, so that there is certainly no superfluid present there. Moreover, because of healing effects, the macroscopic wave function describing the superfluid cannot possibly reach its maximal value from a boundary where it must be zero due to continuity constraints in the wave function and its spatial derivative. As a result, upon transitioning from the vapor above and the solid below the liquid film, a finite length must be traversed in order to even be able to deposit a nonzero superfluid fraction within the liquid film. Above the dead layer, the superfluid density can safely be taken as the value it would assume within the bulk fluid, so

long as the helium film is not substantially compressed. [55] So, the third-sound speed in Equation 1.111 can be written as

$$c_3^2 = \frac{\rho_s}{\rho}\mathcal{F}_{vdw}(d - D_{dead}). \tag{1.113}$$

Since third-sound is a wave in a thin film of superfluid helium, it can also be used as a probe to observe the KT transition. [42] Figure 1.19 shows third-sound data taken on a flat surface using the substrate CaF_2, which has been adapted from data in Reference [56]. Because it is a thickness/temperature wave, third sound can be excited mechanically or thermally. Chapter 2 will elaborate more on these techniques. In Figure 1.19, the detection was made using a time-of-flight method, where a heat pulse results in the excitation of a signal which is then detected on the other end using a receiver. Knowing the time difference between the source signal and the detected signal, as well as the distance between the source and the receiver, allows for the determination of the sound speed. Note that the hash-marks in the figure essentially represent an abrupt drop in the superfluid fraction, where there was no substantial rounding in the transition. Finite-frequency effects are still prevalent in the measurements, but do not result in a gradual drop since the signal was probably buried in the noise due to the attenuation of vortices as well as desorption effects. However, note the flat trend of the sound speed immediately after the hash-mark of a given plot. This represents the finite-frequency broadening to some extent, since if the superfluid fraction reached its maximum value at the transition point, the sound speed would have decreased from the signal onset on account of the drop in the vdW restoring force with added film. A rounded transition can be seen in Figure 3.5, which is primarily due to finite-size effects on the Multi-wall Carbon Nanotube (MCNT) powder.

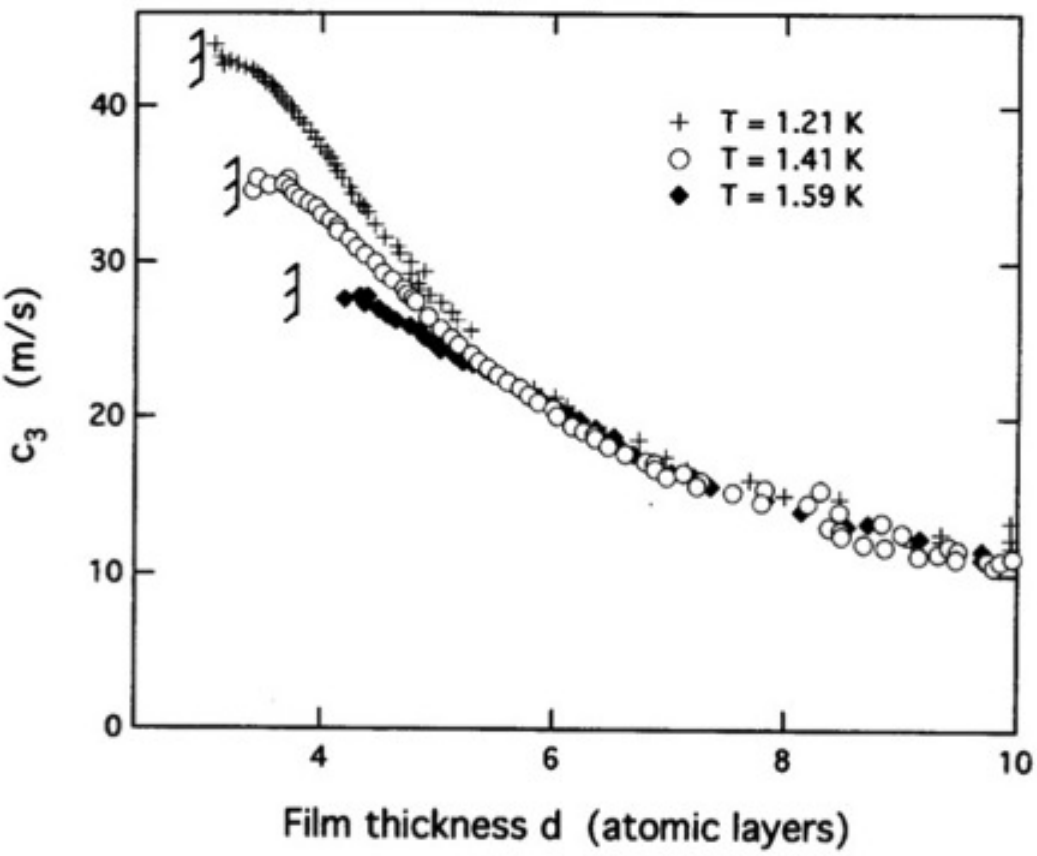

Figure 1.19: **Experimental observation of third-sound on the flat substrate of CaF_2.** The plot is taken from data in Reference [56]. There is no observed signal at temperatures below the hash-marks for each plot of c_3 as a function of the film thickness, where 1 layer $\approx$ 3.6 Å. Note that the higher the temperature, the larger the initial film thickness required to form a superfluid layer. Moreover, the larger the temperature, the smaller the sound speed since the film is thicker and, thus, the vdW restoring force is smaller.

CHAPTER 2

Experimental Setup

An acoustical investigation was undertaken to observe the onset of superfluidity on Multi-wall Carbon Nanotubes (MCNTs). The third-sound signal was excited in a cavity packed with a powder of these nanotubes. The measurements were made on two separate cryostats using the same cell. The high-temperature cryostat made use of liquid ^{4}He as the refrigerant, where the liquid helium was dumped into a dewar and then pumped on by a large mechanical pump to reduce temperatures down to a baseline of 1300 mK. The low-temperature cryostat made use of a dilution refrigerator which circulated a ^{3}He-^{4}He mixture to operate between 150 mK and 800 mK. The forthcoming sections will describe details regarding the experimental cell, the employed gas-handling systems, as well as the propagation and detection of third sound in this study.

2.1 The Experimental Cell

Figure 2.1 presents the components used to construct the vacuum-sealed cell which was used as a third-sound, annular (racetrack) resonator. Initially the nanotubes were packed directly into the copper racetrack without the Plexiglas housing. An experimental run at 1300 mK on this system resulted in no detection of a third-sound signal until sufficiently thick films were formed, nearing the saturated vapor pressure. It was believed that the third-sound temperature wave became diffusive in its macroscopic propagation on account of the powder being in direct thermal contact with the copper, and thus creating a thermal short through the thermally

conducting nanotubes. As a result, a Plexiglas insert was machined in order to shield the nanotubes from the copper. Although temperature equilibration would be an issue for short time scales with high vacuum within the cell, this should not have been a major issue for the employed method of taking data in this study, with equilibration times on the order of tens-of-minutes to an hour—particularly when a sufficient helium film had been deposited.

The instrument cap, shown in Figure 2.1c, houses grooves for bolometers—which sense the oscillating temperature associated with the third-sound wave—and heaters—which excite the temperature wave. Two specific bolometers were used: one was a 200-Ω Allen-Bradley carbon resistor, while the other was a 33-Ω variety. The 200-Ω resistor has a very strong temperature coefficient, rising from about 2 kΩ at 4.2 K to around 100 kΩ at 1300 mK. This provided the bolometer with a very steep dV/dI profile, allowing for very sensitive detection of resistance changes due to temperature fluctuations administered from the resonating third-sound standing wave. The amplitude of the temperature wave is on the order of 10 - 100 μK. [57] In the range of temperatures over which the data was taken—150 - 1300 mK—the 200-Ω bolometer provided great sensitivity, with a dV/dI profile that never saturated.

The bolometers were immobilized within the grooves of the instrument cap using epoxy[1], and the side of each bolometer facing the nanotube powder was sanded off to expose the carbon element. The response of each bolometer was monitored by biasing it with a 1-μA current from a voltage-divided battery. The outputted voltage oscillations were then run through a preamplifier[2], set to a gain of 5000, followed by a low-noise filter[3], and then entered a data-acquisition box which digitized the signal to then analyze with LabView. The LabView program performed a Fast-Fourier Transform (FFT) on the incoming time-domain signal,

[1]Emerson and Cuming Stycast 1266.
[2]Stanford Research Systems Model SR560 Low-Noise Preamplifier
[3]Stanford Research Systems Model SR650 Dual-Channel Filter

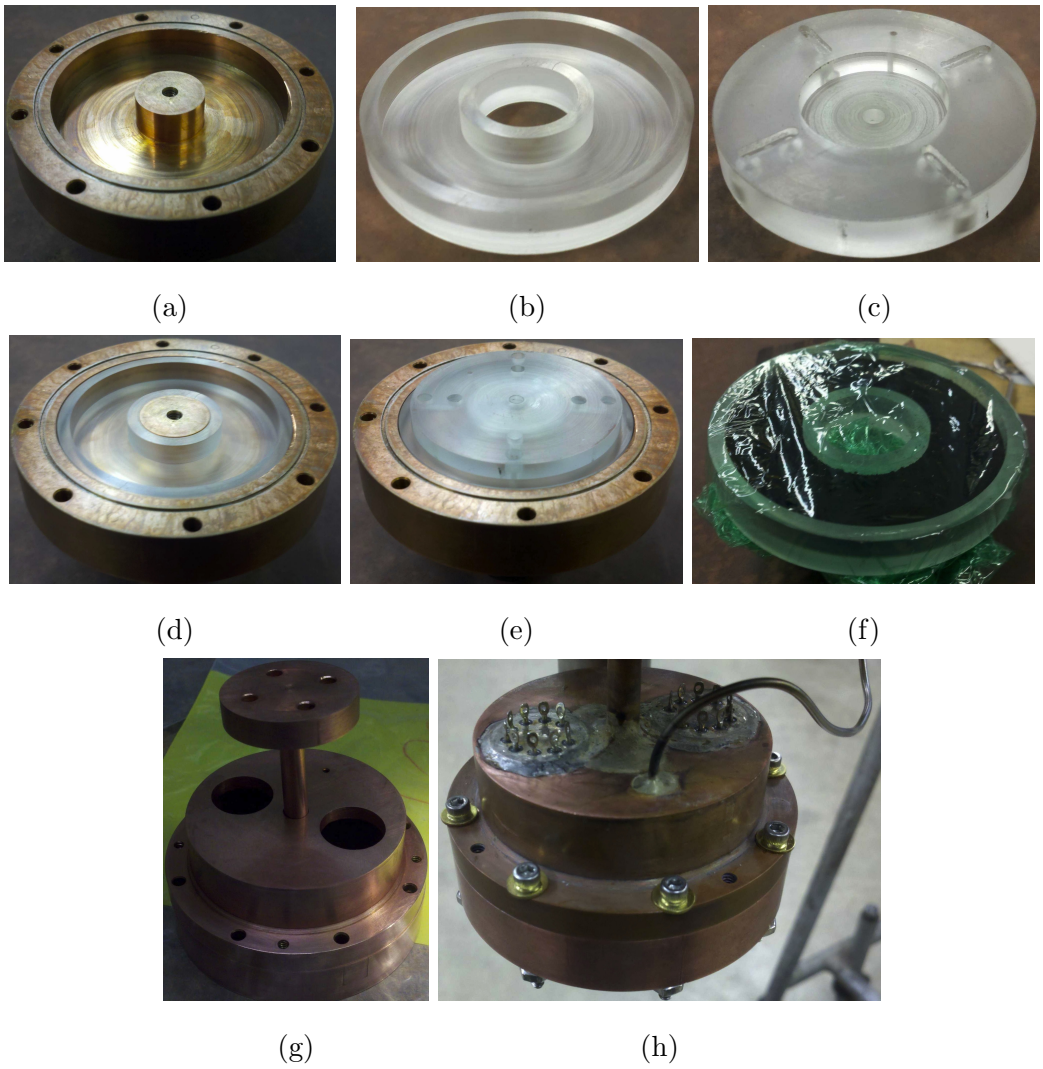

Figure 2.1: **Cell components and construction.** (a) Copper racetrack. (b) Plexiglas racetrack that houses the packed nanotube powder. The i.d. of the gap is 0.814", the o.d. is 1.776", and the depth is 0.190". (c) Nanotube instrument cap. The grooves at 0 ° and 90 ° house bolometers, while the ones at 180 ° and 270 ° house heaters. (d) Plexiglas racetrack in the copper racetrack. (e) Instrument cap placed on top of the racetrack assembly. (f) Packed MCNTs in Plexiglas racetrack. The powder is packed in a single helping. The depth of the powder volume is 0.126". The plastic wrap is taken off when installed. (g) Cell enclosure assembly. The large holes are for soft-soldering hermetically sealed electrical crowns, while the smalle hole is for hard-soldering a 1/16" SS fill line. (h) The assembled cell.

which it then converted to a frequency-domain signal for observing resonance peaks in the third-sound wave.

The two remaining grooves on the instrument cap were made into heaters. Two leads snapped off from a resistor were secured with epoxy and made to protrude slightly below the groove. Carbon paint[4] was then used to connect the leads to form a resistor with typically 0.5 - 2.0 kΩ of resistance at room temperature.

Since nanotubes also have the capability of electrical conduction, precautions were taken to insulate the heaters and the bolometers from shorting out to the nanotubes, particularly since these elements were made flush with the instrument cap facing the nanotubes. The proposed solution to this problem was to use three stacked nuclepore filters[5] to just cover each of the grooves. These filters had a nominal pore diameter of 0.2 μm. The barrier of filters would allow contact between the helium adsorbed on the nanotube powder and the helium coating the pores in the filters, while electrically insulating the heaters and bolometers from the MCNT powder. The contribution to the third-sound signal coming from the filters—which themselves could propagate a third-sound signal and have been extensively studied under such circumstances [58, 59]—would be minimal, both because of the negligible amount of helium coating the porous membranes, and because a signal coming from the pores within these membranes would have to be detected over the length of the carbon element within the bolometer (which cannot happen since the bolometer is not a point detector). Thus, the detected signal must be a result of third-sound resonances within the nanotube powder.

Since third sound is a temperature wave in the superfluid helium film, one standard method of excitation is to make use of a heater pulse. The classic method would be a time-of-flight measurement [56], where a heater pulse is generated and then detected using a bolometer. Knowing the dimensions of the flight path

[4]SPI brand carbon conductive paint (colloidal graphite in isopropanol).
[5]Whatman Nuclepore polycarbonate track-etched membranes.

and the time difference between the generated and detected pulses would then warrant a calculation of the speed. Another method would be to run an AC current through the heater and then sweep in frequency in order to find the resonances. [60] This is a method that was employed in the experiments performed on the MCNT powder; however, there is a drawback to the use of a heater. On the one hand, a larger input current would certainly result in a larger-amplitude signal, which is desirable for sensitively detecting with the use of a bolometer. However, putting in too much of a current comes at the cost of possibly boiling off the film, proving to be detrimental to the detection of the superfluid onset. Being sensitive to the onset is already made difficult due to the attenuation put forth by the unbinding of the vortex-antivortex pairs at the transition temperature. [38] As such, inputting extra dissipation in the form of film desorption from the excitation of the third-sound wave makes it difficult to sensitively detect the onset using this heater-driven method. [49, 53, 61, 62]

Although heater drive was used occasionally in the excitation of third-sound, the primary method of excitation—particularly in the vicinity of the onset region—was purely mechanical. Two methods of mechanical excitation were employed. The first method was solely employed on the high-temperature system (see Section 2.3 for further details regarding this system), which was used to study the adsorbed film at 1300 mK. The experimental cell, in Figure 2.1h, was rigidly clamped to a cryostat that was inserted into a dewar. The cryostat's top flange was bolted to the bolt circle at the neck of the dewar. Thus, there was a mechanically rigid connection between this flange and the cell. To induce the thickness wave in the film, the flange was lightly and repeatedly hit using a hammer. The vibrations induced on that topmost flange put forth a free oscillation that ran through the various rigid tubes feeding electrical and gas lines to the very bottom of the cryostat. Eventually these vibrations made the cell oscillate at the bottom of the cryostat, inducing the third-sound resonance. The necessary frequencies

were present in these free oscillations as dictated by the Fourier decomposition of a pulse. In this sense, a frequency "sweep" was performed on the cell, and the resonance frequencies were then detected by the bolometer. When a resonance in the heater signal was detectable, it was verified that the mechanical vibrations were indeed exciting the third-sound wave, as both excitations were then used to generate the same resonance response at a given film thickness.

The position on the flange at which the hammer was hit repeatedly made a difference for the strength of the signal detected. For instance, the standing-wave structure may be induced in such a way that the bolometer may sit at a node. Moreover, the placement of the hits may not be generating a large-enough response in the amplitude of the free oscillations running to the experimental cell. Thus, on the basis of trial and error, some sweet spots were determined to better investigate the signal. However, exciting the wave from different spots on the top flange made no marked difference for the resonant frequency of the standing-wave.

As can be imagined, exciting the wave in this manner was not perfect. Indeed, this method of excitation was certainly not localized and did tend to generate stray resonances. These resonances were a combination of mechanical resonances from within the cryostat, as well as microphonics from the jiggling of the various wires running down to the experimental cell. Since the third-sound signal depends on temperature and the adsorbed helium film thickness, it was easy to filter the real signal from such stray signals, as these stray signals were static and rarely shifted in frequency. Sometimes the stray signals would be in the way of the third-sound signal as it moved in frequency as a function of temperature or film thickness. However, the amplitude of the stray signals was usually much smaller than the amplitude of the third-sound resonance, allowing for the proper separation of the real signal from the fake ones. This separation was made even clearer due to the relatively large quality factor, Q, of the third-sound resonance in comparison to the stray ones.

Although this method was very useful for investigating the resonance response of the superfluid film at high temperature, it was useless for lower temperatures. When running the systems at these temperatures with the help of a dilution refrigerator[6], there was no resonance response whatsoever from using this technique, partly because the cryostat/dewar assembly was held up using a vibration-isolation system, making it more difficult to focus the free oscillations to move through the cryostat. Moreover, ramping up the hitting strength was detrimental to the fridge, as it typically resulted in the jumping around of the temperature at the various stages at which the temperature was being monitored.

Because of this shortcoming, a more localized oscillation was employed to make the cell the primary vibrating component on the cryostat. Thus, a magnet-in-coil shaker (which will henceforth be called the "shaker") was made from scratch to attach to the cell to help induce center-of-mass oscillations. These oscillations would help produce the thickness waves in the helium film, similar to how a trough of water can be oscillated to lead to the formation of shallow-water waves. Figure 2.2 showcases the construction of this shaker. The coil was constructed from superconducting copper wire wound separately on two ends of a machined Plexiglas housing. The coils on either half of the shaker were epoxied to hold the them in place. The superconducting nature of the coils was useful in the operation of the shaker to help minimize the heat load on the cryostat while running a current through the wires. The absence of coils in the region where the two halves join (via a bolt circle) provided enough of a gradient in the solenoidal magnetic field to drive the magnet that was also centered at the adjoining region of the two halves. The magnet was held in place with two springs that were sandwiched on either side of the magnet. On either end of the shaker was a threaded hole that allowed for the screwing of a nylon screw that runs through SS bars that kept the shaker tightly in place underneath the cell. These SS bars were threaded at

[6]The details of this system will be spared until Section 2.3.

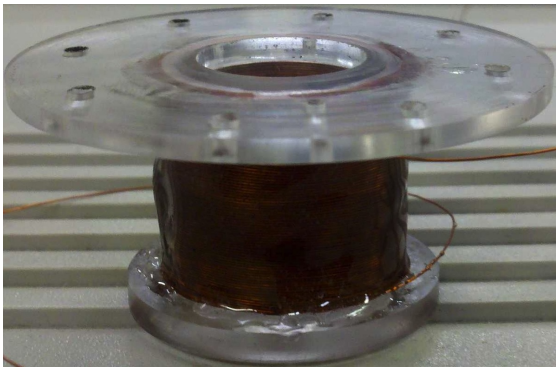

(a)

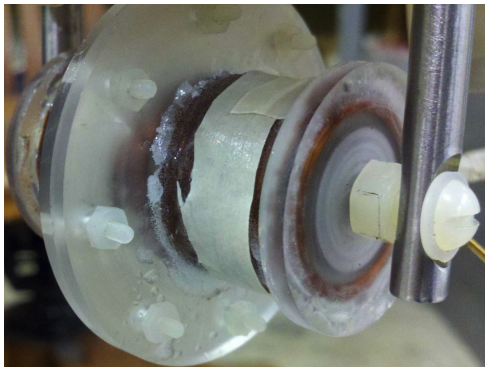

(b)

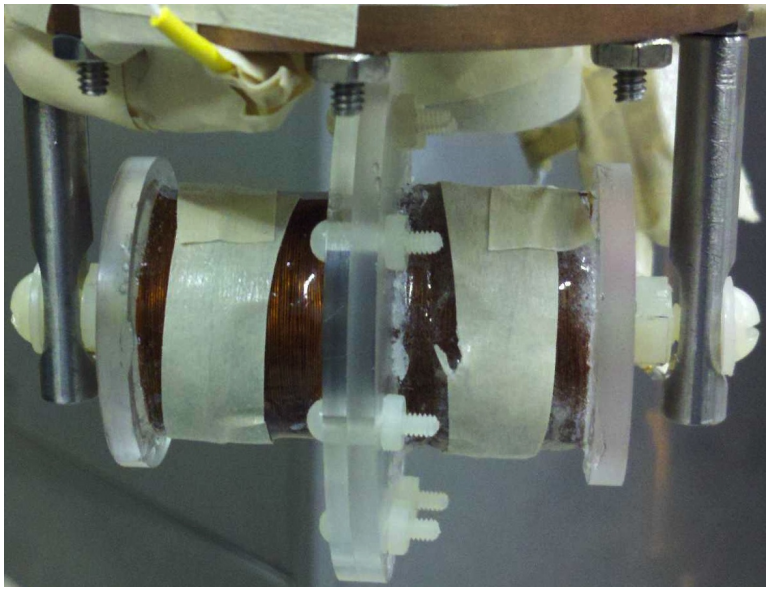

(c)

Figure 2.2: **Shaker construction and placement.** (a) One half of the shaker. The bolt circle allows for fusing the other symmetric half. The coil is made of copper and the hole houses the Neodymium magnet and springs. (b) A close-up of the shaker while mounted. The two halves keep two springs on either side of the centered magnet compressed. (c) The shaker is attached using diametrically opposite SS bars that get screwed into protruding 4-40 screws that are part of the cell's bolt circle (used to compress the cell's indium O-ring). The nylon screws on the left and right ends run through holes in each SS bar and get screwed into threads on either end of each half of the shaker to keep it firmly in place.

the top to screw into diametrically opposite, protruding 4-40 SS screws that were part of the cell's bolt-circle[7]. To summarize the components of the experimental cell, a cross-sectional schematic of the experimental cell and shaker assembly is presented in Figure 2.3.

The shaker was used in a run on the high-temperature system as a proof of principle. It worked very well, particularly since the cooling power of this system was practically unaffected by the drive amplitude of the magnet. This was mainly because the shaker and the cell were in direct contact with the liquid helium bath, which itself was at the operating temperature of the cell.[8] However, there was a considerable heat load on the dilution refrigerator, most likely due to the poor thermal contact with the magnet within the shaker. The idea was to keep the thermal conductivity between the cell and the shaker as low as possible in order to inhibit the transfer of heat generated from the shaking of the magnet. However, this also meant that the thermal gradient from the shaker to the cell (and other parts of the refrigerator) would be large since cooling down the cell would not necessarily cool down the shaker assembly. As such, there was an unmitigated heat load on the cell. Moreover, barring heating from the actual vibration of the magnet, the magnet itself would have taken a long time to cool down to low temperatures in the first place. It was believed that part of the reason why the base temperature was sufficiently above the known capability of the refrigerator was due to this. Thus, even though having little thermal contact with the shaker was helpful[9], it also limited the cooling power of the refrigerator.

Often times—particularly near the superfluid onset, or at points in the third-sound profile where there was considerable attenuation—the shaker was driven

[7]The cell's bolt-circle uses 4-40 SS screws to merge the two copper pieces that form the experimental cell together ((see Figure 2.1h), and compress the indium O-ring used to seal the cell at low temperature.

[8]Sparing specific details to Section 2.3, this was achieved by pumping directly on the liquid helium in the bath space using a high-throughput, high-speed pump.

[9]Mainly to reduce the heat load on the fridge and to provide it with a manageable rate of heat transfer.

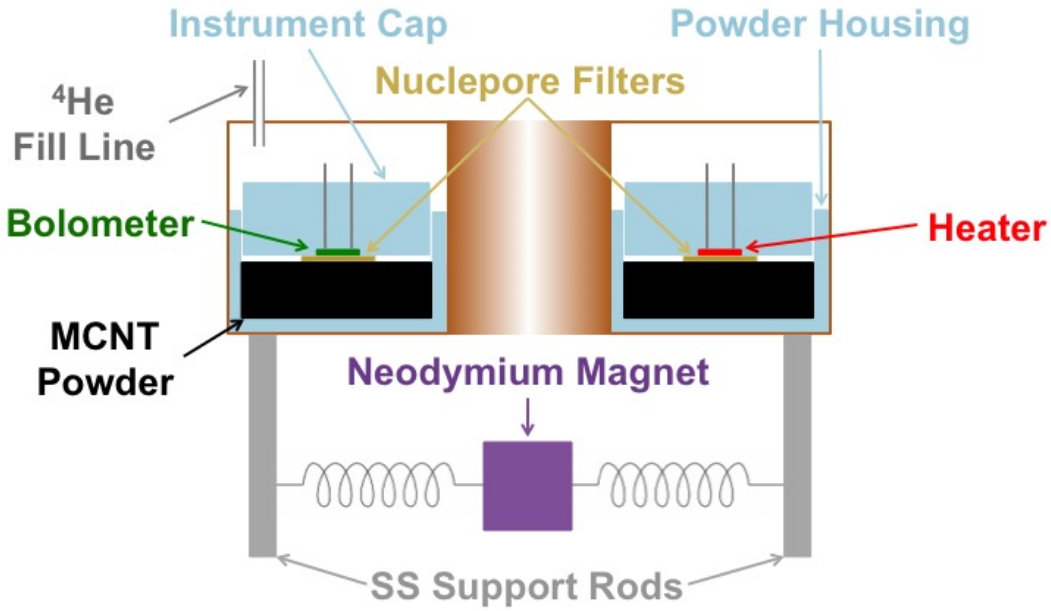

Figure 2.3: **Cross-sectional schematic of the experimental cell and shaker assembly.** The lowest-frequency mode in the resonator will be the whispering-gallery mode that travels along the circumference of the cavity, as the azimuthal degree of freedom has the largest dimension in the cavity. The shaker induces center-of-mass oscillations in the cell, resulting in the sloshing of the helium film to produce the third-sound wave mechanically. The heater may also be used for excitiation by inducing a heat pulse to get the coherent temperature wave to begin propagating across the film. The cell is made of copper, while the instrument cap and the MCNT-powder housing are made of Plexiglas.

at higher amplitudes to try to raise the third-sound signal above the noise for proper detection. This proved detrimental to the cooling power of the fridge, as the fridge assembly was rigidly connected to the cell assembly. Again, the rigid connection was helpful as it was in very good thermal contact with the coldest portion of the dilution fridge. However, this rigidity also led to the shaking of the fridge components, which made the fridge operate in a manner that was certainly not part of its list of immunities to external issues.

2.2 The Nanotube Powder

The nanotube powder was a MCNT powder purchased from Cheap Tubes, Inc. High-quality nanotubes have been known to be rather expensive, particularly five years prior to this report, which was when the samples were bought. Although the nanotubes from this company were not particularly desirable based on the lack of uniform orientation, vast diameter distribution, and overall quality of the tubes[10], this was not an issue for the experiments conducted in this study as they were intended to observe the specific constraints that the atomic-scale, cylindrical geometry would enforce on thin films of superfluid helium. In other words, as long as the powder was overwhelmingly composed of cylinders, the results under these experimental conditions would not have wavered much.

The manufacturer claimed that the powder consisted of MCNTs with outer diameters ranging from 8 - 15 nm. As can be seen in the various SEM images in Figures 2.4 and 2.5, the packed powder that was used consisted of many large grains, ranging from 5 - 30 μm across, which persisted across macroscopic length scales.[11] The tubes were several microns long, although the exact lengths were difficult to determine since the tubes were tangled and braided together while

[10] As would be the case for studying electronic transport properties, where the use of pristine, highly oriented tubes is necessary.

[11] Only for the thickest films would this overarching grain structure play a role. More will be said later in this report.

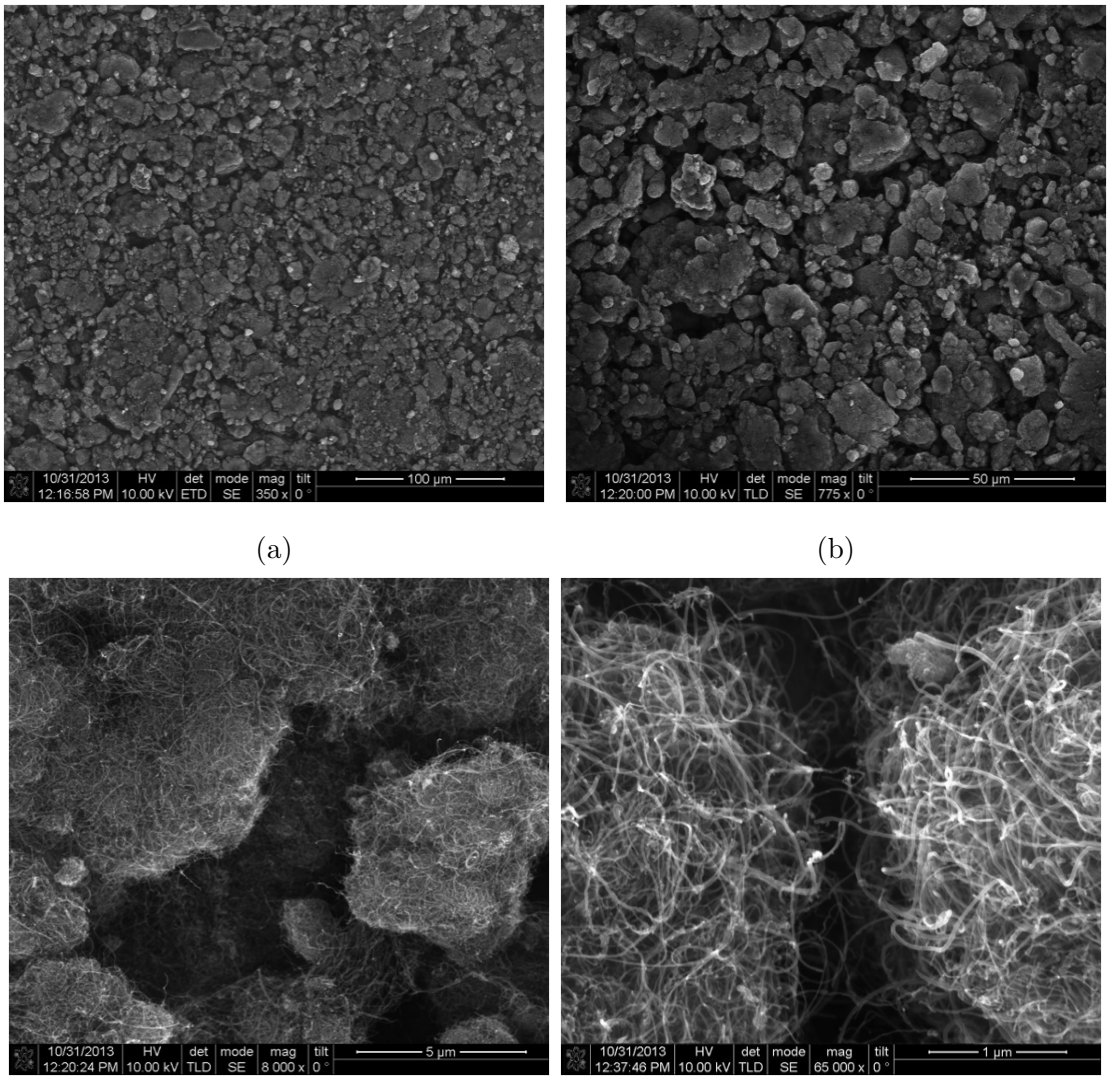

Figure 2.4: **SEM images with progressive zoom.** (a) The MCNT powder. Note the grain structure across macroscopic length scales. (b) A further zoom into the region shown in image (a). (c) A zoom into a few of the grains present in image (b). Note the spaghetti-like structure becoming apparent. (d) A further zoom into the region between two specific grains.

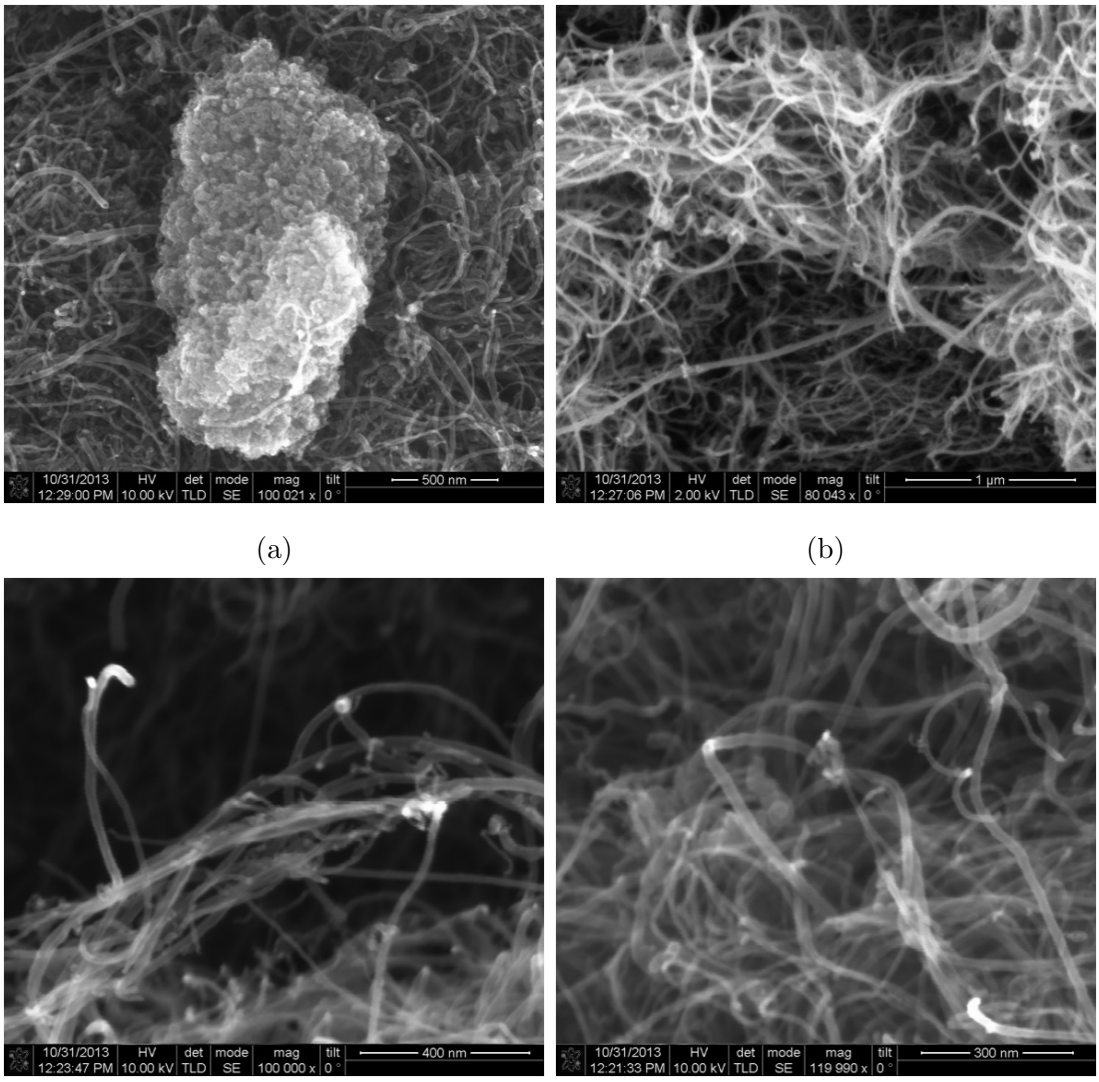

Figure 2.5: **SEM images of the MCNT powder at the smallest length scales.** (a) An amorphous carbon impurity within the forest of tubes. (b) A closer look at the forest. (c) A closeup of some tangled and wavy tubes. Note the standing tube at the top left. Although it terminates, the other end's termination point is unclear. It is at least 0.5 µm in its protrusion. (d) A further closeup of some bent and kinked tubes.

exhibiting twists, kinks, and bends. Impurities were also identified[12], some of which were catalyst particles that were used in the production of MCNTs via the Chemical Vapor Deposition (CVD) method. Other impurities were amorphous collections of carbon atoms. Neglecting the presence of some catalyst particles and amorphous carbon blobs, the powder was relatively clean and was almost entirely composed of tubes.

Although the SEM (Scanning Electron Microscope) images provided some insight into the structure of the powder, it was also necessary to characterize the internal structure of the MCNTs. For this, TEM (Transmission Electron Microscope) grids were utilized to take TEM micrographs of a sample of this powder. The powder used on the grids was not sonicated, so that the images displayed the powder in the form in which it was received from the manufacturer. It is believed that the inherent damage resulted from the poor conditions in which the tubes were grown in the manufacturing process. Figures 2.6 and 2.7 display some of these images. From the sample of images compiled, the tubes were, contrary to what was stated by Cheap Tubes, 10 - 30 nm in their diameter. It was also determined from these micrographs that the tubes consisted of hollow cores and that they did exhibit damaged outer layers. Although some of the images in the TEM micrographs showcased both open- and closed-ended tubes, the distribution profile of the tubes with regard to the nature of their endcaps was totally unclear.[13]

[12]The identification was done using Energy Dispersive X-Ray Spectroscopy (EDS). While performing microscopy using electrons (such as in TEM), the primary electron beam can be used to interact with atoms in the sample, causing shell transitions in the elements that are being bombarded by the beam. From the energy characteristics of the emitted X-rays from these shell transitions, the parent element may be determined uniquely. This is the essence of the EDS technique.

[13]The author is grateful to B. Chris Regan and his graduate student, William (Billy) Hubbard, who took a very generous amount of time and utilized their own resources to take these beautiful SEM and TEM images of the powder used in this study.

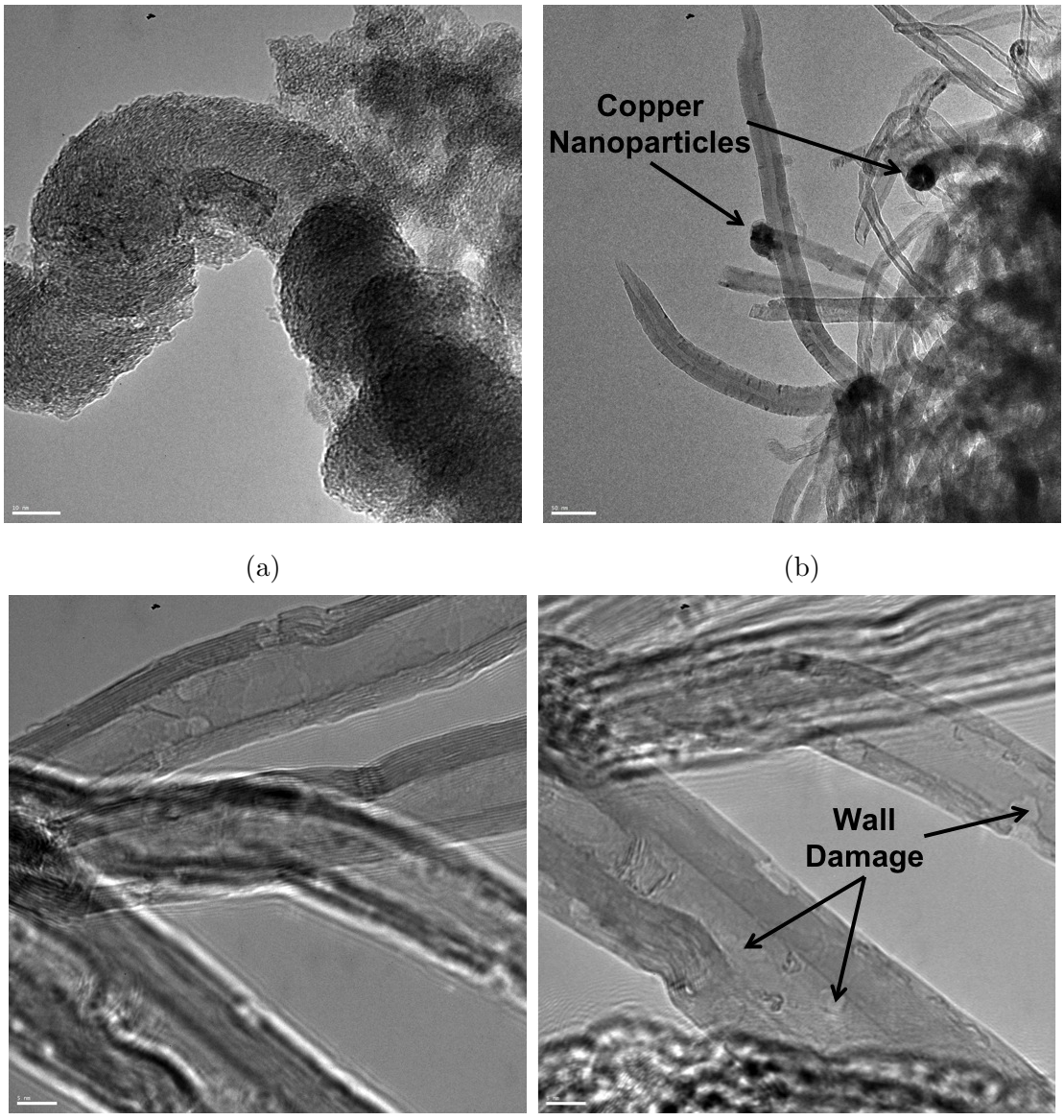

(a) (b)

(c) (d)

Figure 2.6: **TEM images detailing MCNT powder contents.** (a) An amorphous carbon structure. (b) Copper nanoparticles stuck at the tip of a couple of tubes, consistent with the tip-growth model of CVD MCNT production. (c) Some MCNTs in closer detail. Using the length scale provided in the image, the tubes have approximately a 15-nm o.d. and a 5-nm i.d. (d) The presence of wall damage is evident upon viewing regions in the structure that exhibit lighter shades, signifying a larger transmission coefficient in the detected electron beam.

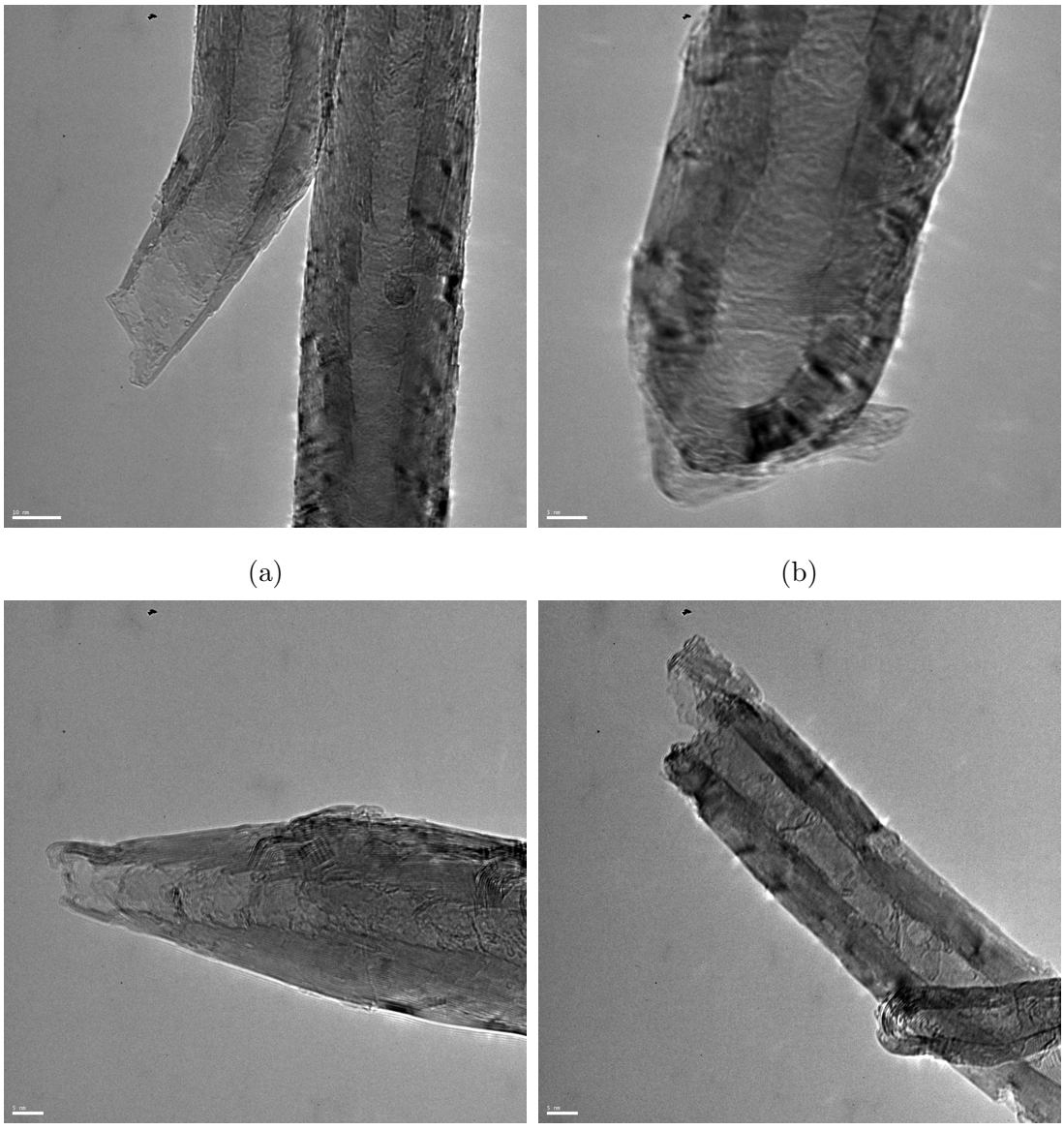

(a) (b)

(c) (d)

Figure 2.7: **More focused TEM images of the MCNT powder detailing wall and end structure.** (a) Closeup characterizing the inner wall structure of some tubes. Note the bamboo-joint structure. The number of walls vary along the tube's length. The left-hand tube is kinked and open. (b) An example of a closed MCNT. The endcap is possibly a hemispherical buckyball. (c) An example of an open tube with a narrowing diameter toward its tip. (d) Another example of an open tube, severely disfigured at its end.

2.3 Low-Temperature Systems

The experiments on the packed MCNT powder were performed using two separate low-temperature systems. This section will describe, in brief detail, the gas-handling system used for metering helium into the experimental cell, as well as the cooling mechanisms for the temperatures at which the sample was studied.

A gas-handling system was implemented to allow for filtering[14] the ^{4}He gas through a Liquid Nitrogen (LN) cold trap, and for sensitively metering in shots of the gas to be adsorbed onto the cold MCNT powder. Figure 2.8 is a schematic of the gas-handling system used for this purpose. The helium gas was purified using the LN trap twice: once while being pushed into the reserve keg of the system and once more while being forced into the experimental cell. To have better control over the number of helium atoms added to the experimental cell, the reserve keg was closed off at valve C_2. Valve C_5 remained closed to prevent bypassing the cold trap, while valve C_8 remained closed unless cleaning of the accumulated cold trap impurities was in order with the use of the shown pump assembly. The diffusion pump was typically used not for the cleaning of the cold trap—which was typically heated with heater tape to more easily desorb the impurities—but rather to pump on the experimental cell. Prior to each run, the experimental cell was flushed with helium gas multiple times to displace impurities, such as air, from the MCNT powder. The flushing also served to check for leaks at room temperature and 77 K to make sure the cell was properly sealed. The diffusion pump would be put in series with the LN-cooled cold trap to prevent the backflow of impurities from the pump (such as oil) from contaminating the cell and the lines leading up to it.

Valve C_7 would be opened to let helium into the experimental cell. The number of helium atoms could then be obtained by using the ideal-gas law and knowing

[14]Unpurified helium gas from compressed-gas cylinders was driven into a reserve keg on board the gas-handling system.

the pressure difference in the tubes when a shot of helium was added to the experimental cell. The pressure difference would be measured using the Wallace & Tiernan pressure gauge attached to the system. With the presence of liquid nitrogen cooling the cold trap, the effective volume of the gas-handling tubes (with valves C_3, C_4, and C_6 open, and the rest closed) was 336 cm^3. Being limited by the resolution of the Wallace & Tiernan gauge, the least amount of helium atoms that could be added to the experimental cell under these conditions was about 5×10^{19} atoms. This minimum number of atoms was small enough to build up the film thickness on the MCNT powder with more-than-adequate resolution, as will be seen upon presentation of the results.

Initially, experiments were performed using a system with a base temperature of approximately 1250 mK. This system is shown in Figure 2.9. The system did not have a 1-K pot, but instead made use of a high-throughput, high-speed pump[15] to directly pump on the liquid helium to reduce the whole bath space down to the desired temperature. The dewar operated in the absence of a nitrogen jacket. Instead, it was cooled by the rising helium vapor that was forced through a narrow gap below the neck of the dewar. The cryostat made use of closed-cell foam to establish this gap. For more information on the design of dewars, consult Reference [63]. The cell was in direct contact with the bath. Although this system had immense cooling power—withstanding 10-mW heating sources while maintaining its base temperature—it was very limited in its practicality, requiring a 20-L transfer every 24 hours, as well as the stopping and restarting of the experiment to allow for transferring liquid helium and pumping back down again to the base temperature, which would take 3 - 4 hours. The gas-handling system was hooked up to the fill line of this basic cryostat. The base temperature was limited by the pump's pumping speed and throughput, as well as the heat-leaks present (predominantly via radiation and conduction). These experiments

[15]The pump was located in a separate room to allow for noise and vibration isolation.

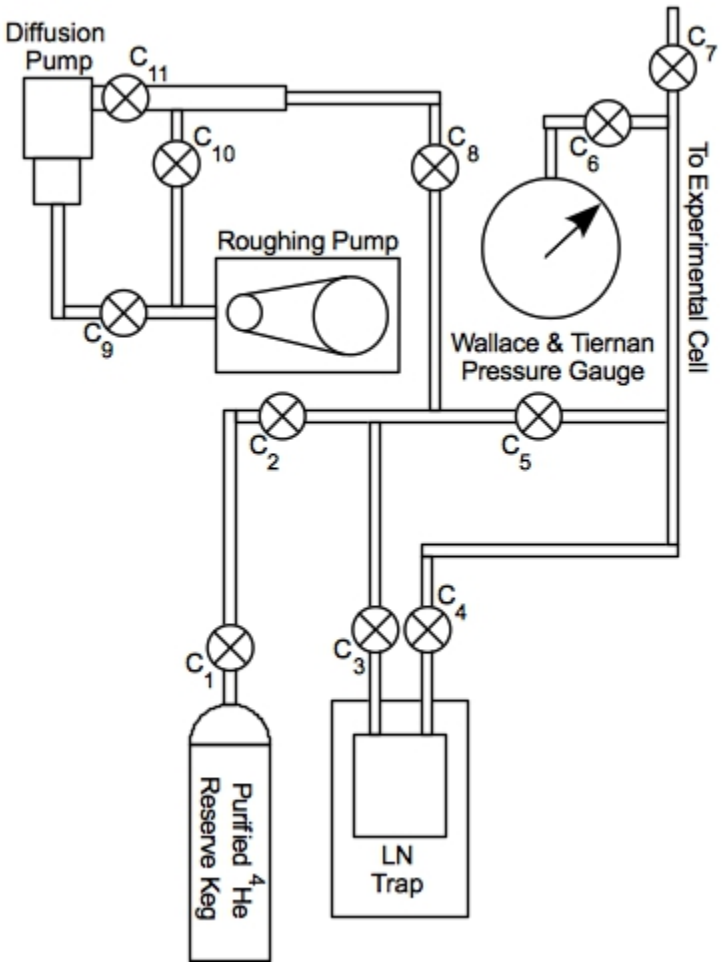

Figure 2.8: **Gas-handling system for the experimental cell.** The purified helium gas was not metered into the cell while open to the reserve keg, as this would have allowed little control over building up the adsorbed film of helium in fine thickness intervals. Instead, the tube volume between valves C_2 and C_7 (running through the cold trap) was used while having valve C_6 open to monitor the pressure before and after each shot of helium. Valve C_5 remained closed to ensure the ^{4}He gas traveled through the cold trap for further purification before being admitted into the cell. The effective volume was 336 cm^3.

Figure 2.9: **High-temperature system.** This system consists of a dewar with a pump line attached to its neck. The pumping line is about 3" in diameter. A high-throughput pump is used to pump directly on the liquid helium dumped into the dewar. The experimental cell is in direct thermal contact with the liquid-helium bath. The cryostat inserted into the dewar is a very basic configuration of gas lines and electrical feed-through tubes that run directly to the experimental cell located at the bottom of the cryostat. These tubes are thin-walled, SS tubes with radiation baffles that help limit radiative and conductive heat transfer into the dewar.

were performed at 1300 mK, to which will be referred as "high temperature."

The experimental cell was then mounted on a low-temperature system with exactly the same cell gas-handling system. This low-temperature system made use of a dilution refrigerator upon which the experimental cell was mounted. A panoramic picture of the laboratory showcasing the experimental setup is shown in Figure 2.10. This system was capable of reaching a base temperature of 50 mK. However, with a problematic sealed pump, a large heat load from the experimental cell and excitation mechanism (to be discussed later), as well as a likely loss of ^{3}He

Figure 2.10: **Panoramic picture of the low-temperature assembly.** From left-to-right: Cell gas-handling system; Multi-level, portable shelving with temperature controllers and monitors, signal filter, pressure gauge, function generator, and oscilloscope; Vibration-isolation system with dewar; Pumping and filling lines for fridge, vacuum can, 1K pot, and dewar; Leak-detector and diffusion-pump assembly (behind the silver liquid-helium storage dewar); Portable ^{3}He-^{4}He storage assembly with sealed pump.

as a result of the pump issues, the lowest attainable temperature with this setup was 200 - 250 mK while running the experiment. On small spurts the system was able to go below 200 mK—very rarely reaching 100 mK—but it was not possible to run at such temperatures while exciting the signal.

Dilution refrigerators harness a ^{3}He-^{4}He mixture as the refrigerant. As can be seen in Figure 2.11, the mixture spontaneously phase separates below 860 mK. [64] In the figure, the ^{3}He concentration is represented as

$$x = \frac{\nu_3}{\nu_3 + \nu_4},$$

where ν_3 is the ^{3}He concentration in the mixture and ν_4 is the ^{4}He concentration. Note that there must be a nonzero concentration of ^{3}He in order for the phase separation to occur in the first place. In order to cool down to the lowest temperatures, this concentration must also be just right. The appropriate concentration can be attained using a gas-handling system to increase or decrease the ^{3}He com-

ponent during the operation of the dilution refrigerator, which can be done rather easily.

In a dilution refrigerator, the mixing chamber is where the phase separation should ideally occur. Since ^{3}He is a spin-$\frac{1}{2}$ fermion, then it obeys the Pauli exclusion principle. For this reason, and because of its lighter mass, the phase separation is such that the ^{3}He-rich phase lies on top of the ^{4}He-rich phase under the effect of a gravitational field. Within the mixing chamber, the situation looks as shown in Figure 2.12. Since ^{3}He has a higher vapor pressure than ^{4}He—particularly below 1.0 K when ^{4}He effectively has zero vapor pressure—it is impossible to cool by evaporation with the use of ^{4}He alone. As such, the dilution refrigerator works on the basis of cooling by evaporation by reducing the ^{3}He concentration from the phase boundary present in the mixture. To pull the ^{3}He atoms, a high-vacuum pump is utilized to pump on the still of the dilution-refrigerator assembly, which only consists of ^{3}He. This still space is in direct contact with the capillary tube that dips below the phase boundary, as shown in Figure 2.12. By pumping on the still, an osmotic pressure difference is set up between the dilute ^{3}He phase and the rich phase. [65] It is through this osmotic pressure difference that cooling by evaporation of the ^{3}He atoms from the rich phase can occur. Of course, to operate the refrigerator continuously, an appropriate rate of refilling must occur to continuously supply ^{3}He atoms to replenish the rich phase. Thus, if the rate of replenishment is equal to the rate of evaporation, then one can effectively sit at a specific temperature as dictated by the phase diagram in Figure 2.11. Since the primary isotope running through the gas-handling lines of the refrigerator is ^{3}He, then to modify the amount of ^{3}He in the refrigerant, one simply has to pull out ^{3}He from the reserve keg or push ^{3}He into the keg. Thus, the operating temperature of the dilution refrigerator may be tuned. This, in essence, describes how the continuous-cycle dilution refrigerator operates.

In order to properly operate the low-temperature system, four separate plumb-

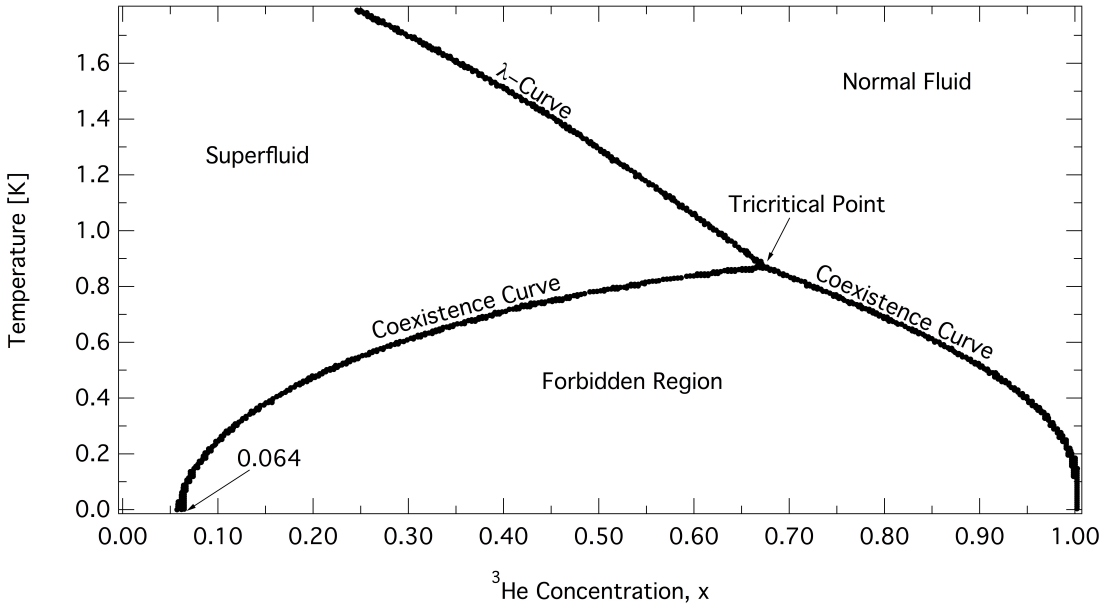

Figure 2.11: **Phase diagram of the ^{3}He-^{4}He mixture under its own vapor pressure.** The plot represents the temperature as a function of the ^{3}He concentration. The regions of normal fluid and superfluid refer to the ^{4}He isotope, as the superfluid transition for ^{3}He occurs below 2.49 mK [1, 2], which is superfluous to point out for the purposes of this diagram. The tricritical point indicated is at 860 mK. Upon going down in temperature and reaching the coexistence curve, a spontaneous phase separation occurs between the ^{3}He and ^{4}He in the mixture. Under a gravitational field, the ^{3}He-rich component is on top of the ^{4}He-rich component because of its lower density (owed to its lighter mass and its need to obey fermionic statistics).

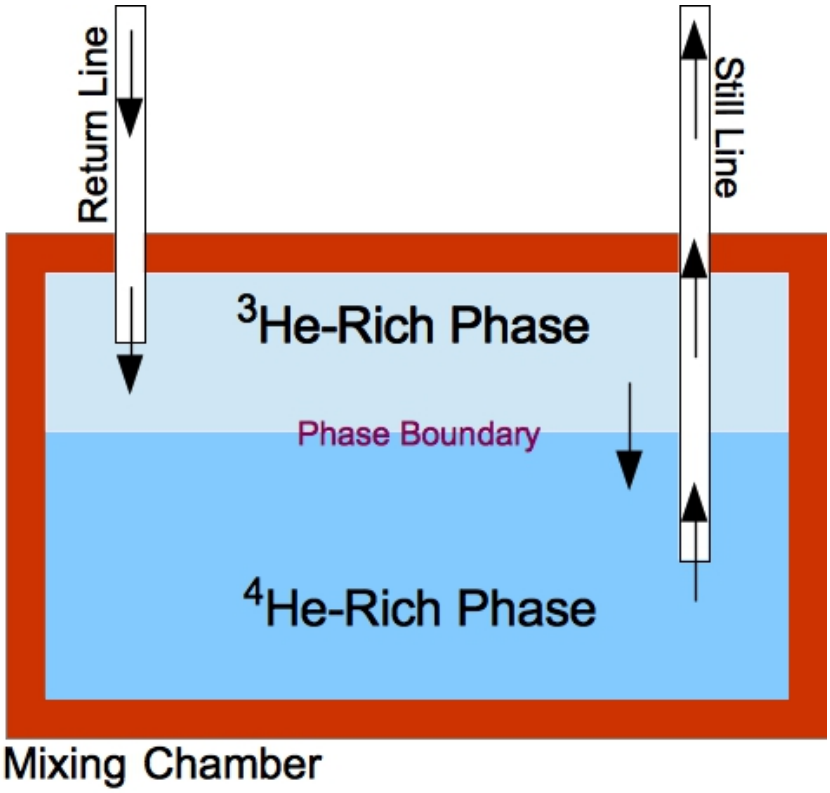

Figure 2.12: **Cooling by evaporation within the mixing chamber.** Below 860 mK the ^{3}He-^{4}He mixture phase separates into a ^{3}He-rich phase and a ^{4}He-rich phase. The osmotic pressure difference between the phases pulls ^{3}He atoms from the rich phase, through the phase boundary, and out into the still. The return line replenishes the mixing chamber with ^{3}He, thus allowing the dilution refrigerator to operate in a continuous cycle.

ing lines were used to prepare, start, and properly run the dilution refrigerator in a continuous cycle. Figure 2.13 is a schematic detailing the fridge gas-handling system, as well as the lines used to access the dewar, 1K pot, and vacuum can. The following few paragraphs will detail the operation of these plumbing lines as it pertains to maintaining, starting up, and ultimately running the dilution refrigerator by referring to this schematic.

2.3.1 Cleaning the Mixture

The ^{3}He-^{4}He mixture—also known as the "mash"—was stored in a reserve keg. To ensure the purity of the mash, it was necessary to clean the mixture, as even the slightest bit of impurity would have plugged the lines leading into the mixing chamber, the most sensitive portion of which was the fridge impedance. This impedance was meant to properly limit the flow of the ^{3}He that replenished ^{3}He supply that was cooled by evaporation within the mixing chamber. Too large a flow would have made the rate of replenishment much more than the rate of evaporation, in which case the base temperature would have been much higher than desired, as set forth by the phase diagram of the mixture in Figure 2.11. On the other hand, too slow a rate of replenishment would have not been able to keep up with the evaporation rate necessary to cool to the lowest temperatures. Thus, a delicate balance was in order. This fridge impedance was a foot-long segment of Cu-Ni capillary tubing[16]—with a 20-mil outer diameter and roughly a 10-mil inner diameter—with a #9 guitar string stuck through the entire length of the capillary. When tested at room temperature, the value of the impedance through this line was 2×10^{11} cm^{-3}. The same length of line without the guitar string stuck through it had an impedance that was roughly two orders-of-magnitude less. With such a high impedance, the slightest impurity (such as hydrocarbon remnants) would have plugged the fridge line at liquid-helium temperatures.

[16]Cu-Ni was used in order to easily be able to soft-solder it at either end in a leak-tight fashion.

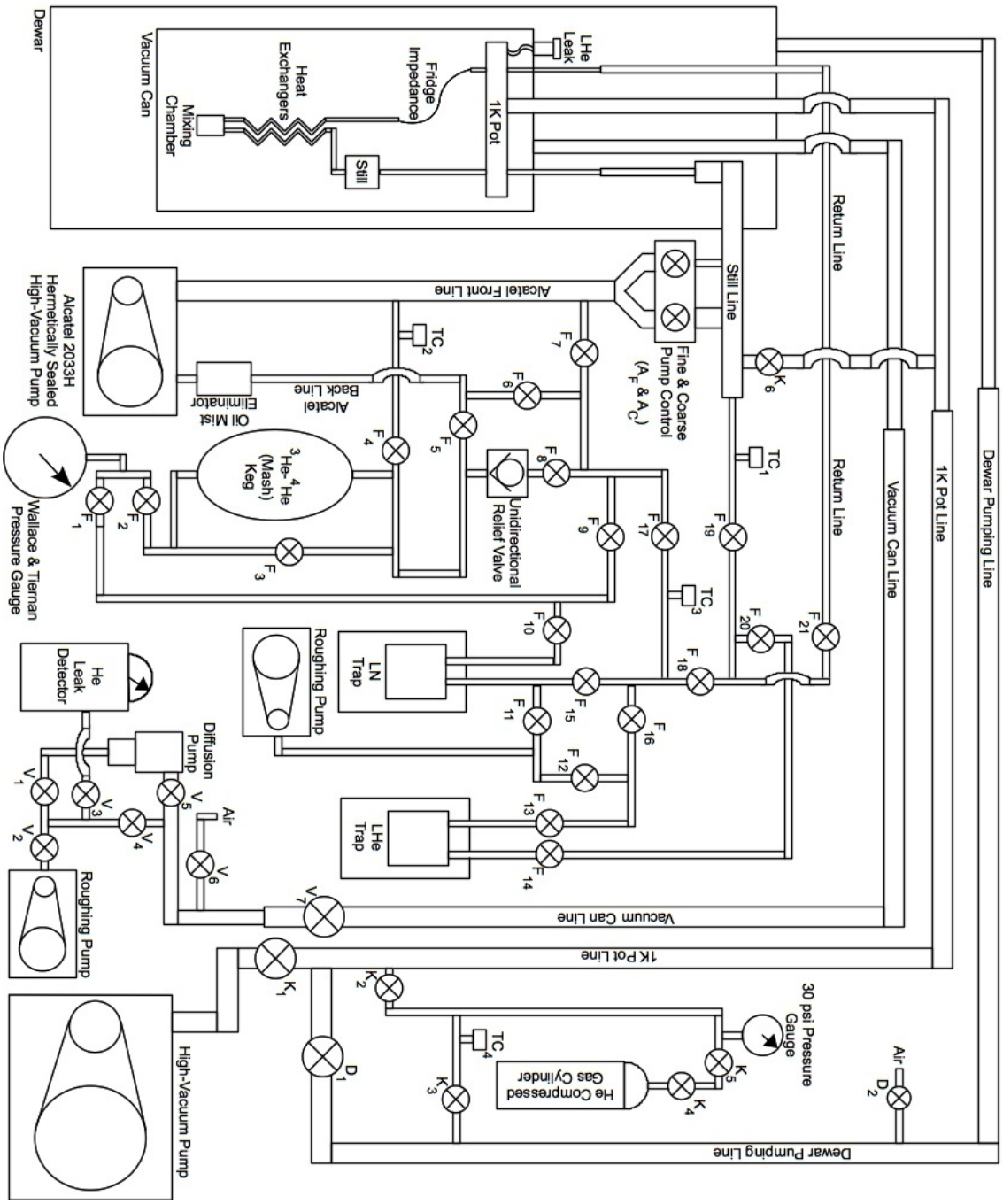

Figure 2.13: **Fridge pumping, filling, and cooling system.** The valves are denoted by F_i for the Fridge line, V_i for the Vacuum-can line, and K_i for the 1K-pot line. There are Thermocouple (TC) gauges that monitor pressures in important areas. Refer to the text for further discussion and details.

In order to clean the mixture, the mash was driven using its own pressure into the LN and LHe traps slowly in order to ensure the proper cooling of the mash while in direct thermal contact with the cold traps. The valve-opening sequence began from taking the mash out of the bottom of the reserve keg and circulating it through the cold traps as follows: $F_2 \rightarrow F_1 \rightarrow F_{10} \rightarrow F_{11} \rightarrow F_{12} \rightarrow F_{13} \rightarrow F_{14} \rightarrow F_{20} \rightarrow F_{18}$. The fact that the mash had reached to valve F_{17} could be monitored using the ThermoCouple (TC) gauge TC_3 that would result in a sudden increase in pressure. Afterwards, valve F_{17} would be opened while running the Alcatel 2033H. Allowing ample time for the pump to warm up, valve F_7 would slowly be opened. The mash would then exit the exhaust and enter into the Oil Mist Eliminator, which simply housed a porous material through which the exhaust gas was forced to move. The filter's purpose was to provide an extra safeguard against allowing impurities (such as the hydrocarbons from the oil) to get mixed up with the mash. To prevent the possibility of this happening, it was imperative to impose the additional safeguard of cleaning the mix through the LHe cold trap, as certain hydrocarbons, as well as hydrogen, cannot be appropriately filtered using the porous zeolite within the cold traps unless the traps were cooled to LHe temperatures. Finally, the exhaust gas was then forced back into the top of the reserve keg by opening valve F_5. With sufficient backing pressure from the exhaust (which can be monitored by occasionally closing valve F_1 and reading the Wallace & Tiernan Gauge), the circulation can be continued indefinitely. Once circulated for a sufficient amount of time, F_2 can be closed to stop the supply of mash from the bottom of the reserve keg. The Alcatel can then be used to pump out all of the open lines to return all of the mash back into the reserve keg. Progress of the cleaning of the lines can be monitored using the gauges TC_2 and TC_3. Once the pressure read-outs reached low values, all lines to the reserve keg can be closed. Valves F_{11} and F_{12} can be used for allowing the roughing pump to clean the LN and LHe traps while exposing the traps to room temperature.

Artificial heating, either with an industrial heat gun or heater tape, was used to ensure all the deposits trapped by the zeolite were properly released to then be captured by the pump.

2.3.2 Cleaning the Fridge Lines

Although the procedure outlined in Section 2.3.1 was used to clean the mixture, it was also important to flush the lines running through the fridge from the still and return sides to clean out impurities within the fridge, particularly when a cool-down was unsuccessful due to the measurement of undesired flow rates through the fridge. The valve-opening sequence began again from taking the mash out of the bottom of the reserve keg, circulating it through the cold traps, and dumping it into the still side of the refrigerator as follows: $F_2 \rightarrow F_1 \rightarrow F_{10} \rightarrow F_{11} \rightarrow F_{12} \rightarrow F_{13} \rightarrow F_{14} \rightarrow F_{20} \rightarrow F_{19}$. Valve F_{19} was just barely cracked open to allow for the cooling of the mash running through the cold traps. Monitoring the pressure with the Wallace & Tiernan gauge allowed for recognizing when there was no longer any more mash being driven into the still from the reserve keg's own pressure. It was not necessary to dump in all of the reserve keg's mash supply, as the desire was to simply rid of the impurities of the fridge with sufficient mash. As such, the reserve keg was closed off. In order to detail the circulation through the fridge, assume now that all the valves have been closed. First, the valve A_F (the Fine valve on the Alcatel pump control) was cracked open to begin pumping on the still side of the fridge. This then began accumulating mash on the exhaust side of the Alcatel. The valve opening sequence to circulate the mash and run it through the cold traps to rid of the fridge impurities was as follows: $F_6 \rightarrow F_9 \rightarrow F_{10} \rightarrow F_{11} \rightarrow F_{12} \rightarrow F_{13} \rightarrow F_{14} \rightarrow F_{20} \rightarrow F_{21}$. Opening F_{21} allowed for pushing the mash back into the fridge lines through the fridge impedance to then be pumped out by the Alcatel from the still side. This process then allowed for the circulation of the mash which could be continued indefinitely, so long as the backing pressure was

large enough to drive the mash back into the fridge. The backing pressure can be monitored using the Wallace & Tiernan by opening valve F_1 and comparing it to the value read by TC_2, which was directly connected to the front side of the Alcatel. Once it was deemed to have circulated enough, the mash could then be placed back into the reserve keg. It was then important to pump out all the lines through which the mash was streamed. To pump out the still line, the coarse valve can eventually be opened to speed up the process of recovery. For good measure, it was best not to rely on the recovery of the mash in the return line from the still side. As such, opening valves F_{19} and F_{21} to expose to the Alcatel front side helped in the speedy recovery.

Cleaning the fridge lines required a reasonable impedance from the fridge impedance. If the impedance was too high, the repeated circulation of the mash might not have properly cleaned these lines, even though whatever had crystallized within the impedance at low temperature would have been returned to a fluid state at room temperature while the cleaning was taking place. If improvements were not seen from this process of circulation, then the best course of action would have been to altogether replace the fridge impedance.

2.3.3 Flow Testing the Fridge

Flow testing the refrigerator at room temperature and at 77 K was an integral part of assessing the needed flow to ensure the proper operation of the dilution refrigerator once cooled down to the required operating temperature. To perform flow tests at either of these temperatures, the mash again would be driven with its own pressure through the cold traps. The mash would then slowly be dumped into the still side of the fridge as in the valve-opening sequence outlined in Section 2.3.2. Once the pressure equilibrated and no more mash was being driven into the still side, valve F_1 or F_2 were closed—depending on whether the pressure in the keg or the pressure in the fridge gas-handling lines needed to be read—in order to

isolate the reserve keg. Valve F_{19} was closed, while the sequence of valves $F_7 \rightarrow F_{17} \rightarrow F_{18} \rightarrow F_{21}$ were opened to allow the Alcatel to pump out the contents of the return line on the return side of the fridge as well as the contents leading up to TC_3, which was to be used to test the flow of the mash from the still side of the fridge to the return side via the fridge impedance. Once TC_3 reached its lowest value in pressure, valve F_{17} was closed off to monitor the pressure rise in order to see if the fridge impedance showed signs of blockage. The mixture would then be collected again by pumping all lines through which the mash was streamed and dumping the exhaust side of the Alcatel back into the reserve keg.

2.3.4 Starting and Running the Fridge

The following few paragraphs outline the procedure for starting the fridge from room temperature. Although it will be indicated exactly when flow tests and leak checks are to be done in the process, the assumption will be that the measurements come out favorable so that cooling down to the base temperature of the dilution fridge is warranted.

Pre-cooling the dewar was a necessity, as it would be a waste to use liquid helium to cool down all of the contents within the dewar to 4.2 K by using the liquid helium itself as the cooling agent. With a low latent heat of vaporization and a high, per-liter cost compared to nitrogen, it is more economical to pre-cool the system using LN. The vacuum can was evacuated prior to placing the dewar around the cryostat to check for leaks in the indium O-ring used to seal the vacuum can. This was done by first using the roughing pump to remove the air in the can up to a reasonably low pressure (below 100 mTorr) by opening $V_2 \rightarrow V_4 \rightarrow V_7$. Valve V_2 was then closed and V_3 was opened to use the leak-detector assembly to pump down the vacuum-can line below 10 mTorr using its own diffusion pump.

The 1K-pot line was evacuated using the high-vacuum pump by opening valve

K_1. Valve K_2 was then opened to evacuate the line leading up to the 30-psi pressure gauge to get a true reading of zero pressure on the gauge. Valves K_1 and K_2 were then closed. Prior to the dumping of the liquid nitrogen into the dewar's bath space, the 1K pot was pressurized to about 5 psi using helium from a compressed gas cylinder. Valves K_4 and K_5 were opened and the pressure was monitored using the 30-psi pressure gauge in series with these lines. Valve K_2 was then opened and valve K_4 was adjusted to read a 5-psi pressure increase from when the line was evacuated. The 1K-pot line was pressurized in order to have a constant outflow of He gas from the LHe leak that runs from the bath space, into the vacuum can, and into the 1K pot.[17] This outflow of He gas provided a displacement of any remnants of air or other impurities from infesting the pores of the leak. The presence of such impurities would inevitably crystallize, particularly below 77 K when the liquid helium was dumped into the bath space. This would prove catastrophic to the running of the fridge, as the fridge relied heavily on the 1K pot to cool the mash down to 1 K to more easily allow the navigation to the phase-separated regime as can be seen in the phase diagram in Figure 2.11.

Upon pressurizing the 1K pot, LN was then dumped into the bath space. The level of the LN was kept slightly below the vacuum can's bolt circle and monitored by noting the spike in a resistance bolometer taped to the desired level outside of the vacuum can. The dewar was left to sit overnight after transferring the LN. The following day, the leak detector was again connected to the vacuum can to check for leaks. The dewar was then pressurized with ^{4}He gas to push out the remaining LN that had not evaporated overnight. The gas would also serve to check for leaks through the vacuum can (mainly through the indium O-ring which

[17]When LHe filled the bath space, the leak from the bath space would slowly fill the small volume within the 1K pot. To cool the pot down to 1 K, the high-vacuum pump would be used to pump on the liquid within the pot, thus cooling the 1K pot by evaporation. The LHe leak consisted of a packed powder that slowly allowed the LHe from the bath to trickle into the pot volume to replenish the liquid that had been evaporated using the high-vacuum pump. The 1K pot served as the cooling stage responsible for reducing the temperature of the mash from 4.2 K to 1 K.

was usually the culprit). Leaks in the fridge lines would be addressed when a flow-test was performed again on the fridge as detailed in Section 2.3.3. Leaks in the experimental cell would be addressed by flushing the cell with He gas from the gas-handling system. A flow-test was also performed on the leak into the 1K pot. To perform this, the dewar was pressurized again to 1 ATM using compressed ^{4}He gas hooked up to valve D_2. Valves K_4 and K_5 were then closed while K_1 was opened (with K_2 still left open) to pump out the 1K-pot line of the ^{4}He gas that was used to pressurize the pot. Valve K_1 was then closed and the pressure rise from the LHe leak was monitored through TC_4.

To prepare for transferring LHe into the bath space of the dewar, the 1K pot was pressurized to 5 psi again, but with the valves K_4, K_5, and K_2 closed off after the line was fully pressurized. The evacuated vacuum can was then pressurized slightly with a small volume of air by plugging the air outlet next to valve V_6, opening valves V_6 and V_7, closing both valves, unplugging the air outlet, and then repeating this process once more. This small amount of air would serve as an exchange gas to cool the innards of the vacuum can (i.e., the main components of the fridge) to 4.2 K upon dumping LHe into the bath. Since the dewar was already pressurized from performing the 1K-pot flow test, exposing the dewar to the atmosphere would not allow air to leak into the bath space. Taking advantage of this, liquid helium would then be transferred into the bath space, requiring roughly 80 liters of the liquid to inundate the bath space up to the top of the belly of the dewar. Only a couple of hours were required to allow the exchange gas to cool the fridge down to 4.2 K, which was easily monitored using resistance bolometers placed at the various stages of the fridge (one on the 1K pot, one on the still, three on the heat exchangers of the still and return lines, and two on the mixing chamber). The exchange gas was then evacuated by initially warming up the diffusion-pump assembly attached to the vacuum-can line while running the roughing pump. Valves V_5, V_1, and V_2 were opened, while V_7 was slowly opened

to pump out the vacuum can. The system was left pumping overnight to ensure complete evacuation of the exchange gas. Having a sufficient amount of exchange gas left over would render the refrigeration process ineffective, as there would be a constant thermal short from the bath space to the fridge. This would put a large heat load on the 1K pot, preventing the mash from phase separating.

Upon eliminating the exchange gas, valve V_7 was closed off and the diffusion pump was shut down. Valve K_1 was then slightly cracked open to begin pumping on the 1K pot, thus letting LHe to start filling the 1K-pot volume through the LHe leak. The mix was then partially dumped into the still, as in Section 2.3.2, by driving the mash using the pressure in the reserve keg.[18]

In order to dump all of the contents of the reserve keg when the keg pressure could not drive any more mash into the fridge lines, the following procedure was implemented. Valve F_4 was opened to the Alcatel's front to pump the remaining contents of the reserve keg into the exhaust line of the pump. This built up the back pressure to allow driving this volume of mash through the cold traps and into the still. The valve-opening sequence was as follows: $F_6 \rightarrow F_9 \rightarrow F_{10} \rightarrow F_{11} \rightarrow F_{12} \rightarrow F_{13} \rightarrow F_{14} \rightarrow F_{20} \rightarrow F_{19}$. Once the mash was emptied from the keg—verified by monitoring the Wallace & Tiernan gauge with F_2 open and F_1 closed—valve F_4 was closed off. The backing pressure was monitored by opening F_1 (with F_2 closed) to read out using the Wallace & Tiernan gauge. Upon dumping into the still side, the mash was circulated by pumping on the still using the front of the Alcatel by slowly opening A_F and then slowly opening A_C to increase pumping power. This would then complete the closed loop allowing for the circulation of the mash, with the Alcatel front side pumping directly on the still and the Alcatel back side pushing the mash back through the cold traps and into the return line

[18]It was found that leaving the mash in the fridge lines after the flow test at 77 K was also acceptable in starting up the fridge, so long as the mash was thoroughly cleaned of impurities. Nonetheless, the mash can still be driven a bit from the pressure in the room-temperature reserve keg, since the pressure of the mash in the fridge lines would be much lower than when originally admitted at 77 K due to the substantially reduced temperature.

to replenish the ^{3}He in the mixing chamber. Ideally, phase separation would occur in the mixing chamber, in which case the fridge cooling will be optimal. With the phase separation prevalent, ^{3}He would be the isotope being circulated through the gas-handling lines. To improve cooling power, a heater attached to the still may be turned on to increase the vapor pressure of the ^{3}He supply in the still, allowing for a larger osmotic pressure difference to drive the ^{3}He across the phase boundary, leading to a lowered concentration of ^{3}He within the ^{4}He-rich phase, and, thus, lowering the temperature according to the phase diagram of the mash in Figure 2.11. If the ^{3}He concentrations were found to be too high, some of the circulating ^{3}He can be deposited back into the reserve keg by briefly opening and closing valve F_5.

CHAPTER 3

Results, Analysis, and Discussion

Aside from interesting layering effects that are prevalent in the adsorbed helium film on graphitic substrates such as MCNTs—which will be described in detail in this chapter—the main motivation for studying superfluidity on the cylindrical geometry is to probe a potential crossover of the KT transition into one dimension. The way in which this can be done is if the relevant length scale in the helium film approaches the relevant length scale of the substrate. The original KT transition was theoretically predicted [39] in superfluid films [40] and experimentally observed in third-sound [42] and torsion-oscillator [37, 66, 67] measurements when looking at films on a flat substrate. In this sense, there was no relevant length scale of the substrate to which to compare a relevant helium-film length scale, so that the transition cannot be anything but two dimensional. However, studies on more exotic substrates such as, among others, Vycor glass [68], Nuclepore [59, 69], and aluminum-oxide powders [43] showcase a rounded transition which more appropriately indicates some form of crossover into a three-dimensional geometry, particularly if the relevant pores in the studied substrate form a multiply-connected surface. [44–46] Under such circumstances (as discussed in Section 1.6), when the vortex string size is comparable to the nominal pore size, then the thermodynamic phase transition is essentially three dimensional.

Instead of crossing over from 2D to 3D, one can, instead, jump from 2D to 1D. Such a crossover is dictated by the vortex-core size, a_0. In other words, if the vortex-core size becomes comparable to the smallest length-scale in the substrate

geometry—in the case of the MCNT powder, the diameter—then the transition is effectively one dimensional. There have been experiments investigating just such a 1D transition [70–72], and this study aimed to further probe this interesting crossover. To be able to achieve a vortex-core size comparable to the MCNT powder's nominal diameter, it is necessary to attain very thin superfluid films. Indeed, it has been shown that in the continual thinning of the superfluid film, the vortex core size can be made to increase considerably, with a value close to 100 Å below 100 mK on aluminum-oxide powders. [73, 74] Such a core size would be comparable to the nominal diameter in the MCNT powder. Nonetheless, the stable, baseline temperature that this study was able to achieve was no less than 200 mK, for which the core size would roughly be half the diameter of the nanotubes. In any case, no such signatures of a 1D crossover were seen at these investigated temperatures.

3.1 Raw Data and Resonance Analysis

As mentioned in Section 2.1, the signal generated from the bolometer within the experimental cell was amplified, filtered, and run into LabView to transform the time-domain voltage into the frequency domain to pinpoint the resonance profile of the third-sound signal. Typical raw data generated from the bolometer is presented in Figure 3.1. The boxes on the very left of each FFT trace indicate the amount of helium added into the cell. This measurement is denoted "Fill" and it stems from noting the pressure difference in the tubes of the cell gas-handling system (as described in the beginning of Section 2.3), which is directly related to the number of helium atoms admitted into the cell. The FFT profiles are stacked on top of one another to help in the tracking of the third-sound peak as a function of fill, with the fill increasing upon going higher in the stack. The signal is around 106.5 Hz at a fill of 481 mmHg, and continues down to lower frequencies,

ending at about 83 Hz at 612 mmHg. The peaks at 93.5 Hz and 109.5 Hz are stray resonances, which clearly do not vary as a function of fill. For instance, it is easy to decipher the third-sound resonance from the fake resonance at a fill of 542 mmHg. Indeed, as the third-sound resonance reaches 93.5 Hz, its profile overshadows the profile of the uninteresting peak, in line with what was described in Section 2.1.

For accumulating and analyzing the data, WaveMetric's Igor Pro graphical-analysis program was utilized. The analysis of the data amounted to fitting the peaks with a Lorentzian[1] The frequency of each fitted peak was taken as the resonant frequency for that particular FFT profile. Furthermore, the width of the fitted peak was also utilized to compute the quality factor (or Q) of the resonance using

$$Q = \frac{f_{\text{res}}}{\Delta f}, \tag{3.1}$$

where f_{res} is the resonant frequency and Δf is the full-width at $1/\sqrt{2}$ of the maximum[2]. The uncertainties for the resonant frequency and the width were statistical, solely based upon the ability for the fitting function to represent the trend in the

[1]This function is the appropriate one, as this system is a damped, driven oscillator that is presumed to be linear, and therefore of the harmonic type. The resonance amplitude for the differential equation

$$\ddot{x} + \beta\dot{x} + \omega_0^2 x = \alpha_0 \cos(\omega t)$$

has the solution $x(t) = A\cos(\omega t - \delta)$ with

$$A^2 = \frac{\alpha_0^2}{(\omega_0^2 - \omega^2)^2 + 4\beta^2\omega^2}$$

and

$$\delta = \arctan(\frac{2\beta\omega}{\omega_0^2 - \omega^2}).$$

The phase shift δ describes the lag that the drive has with respect to the response, with resonance occurring when $\delta = \pi/2$. The amplitude A is a Lorentzian in the driving angular frequency ω. For sufficiently low damping (with $\beta \ll \omega_0$), the resonance occurs exactly at the natural angular frequency ω_0. As always, the frequency used in the scanning of the resonance is $f = \omega/2\pi$.

[2]The full-width at half-maximum is reserved for the intensity spectrum. The raw data was outputting the amplitude spectrum. The intensity is proportional to the square of the amplitude.

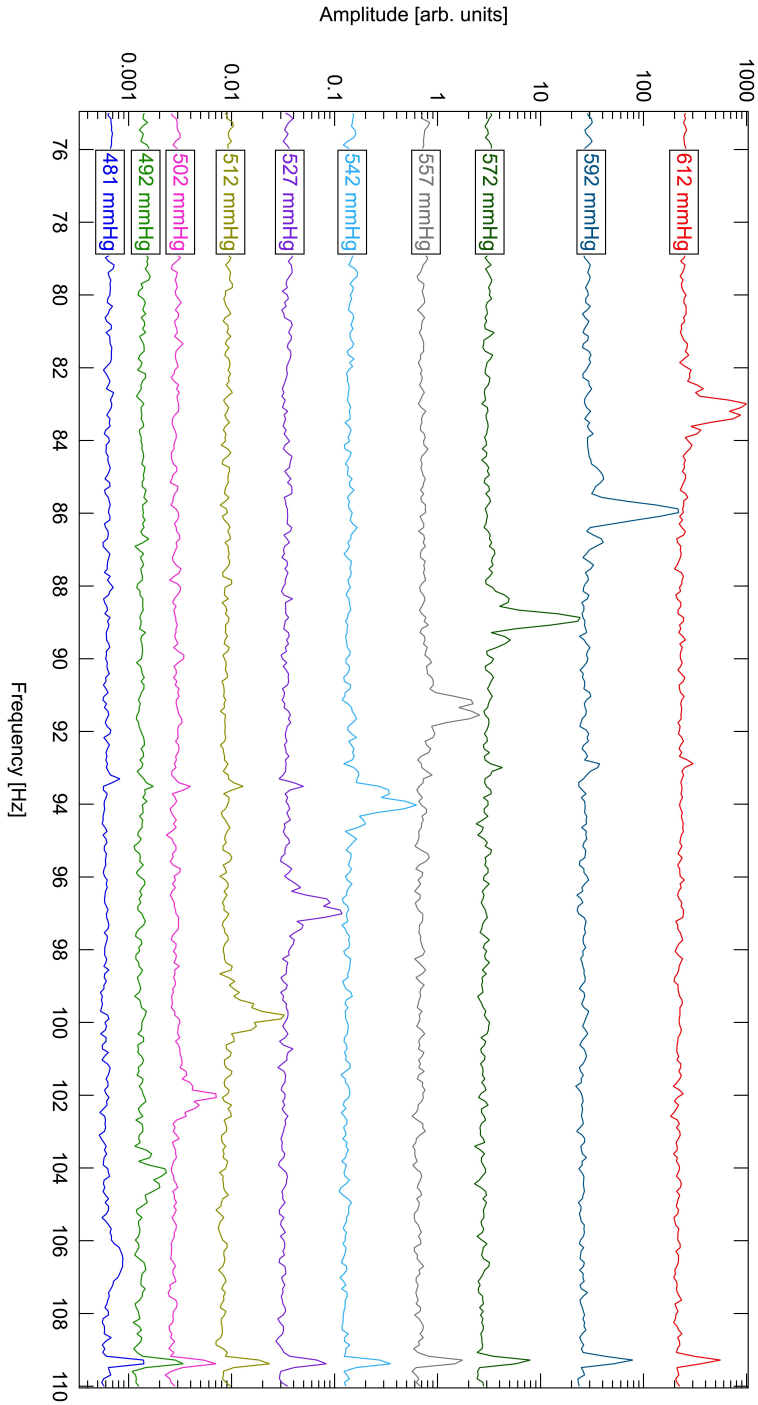

Figure 3.1: **Raw data at 1300 mK using heater drive.** The plot shows the tracking of a third-sound signal as a function of the amount of helium added into the cell. The boxes on the left-end of each trace denote the helium fill. A larger fill corresponds to a thicker adsorbed film. Here, c_3 decreases as the fill increases.

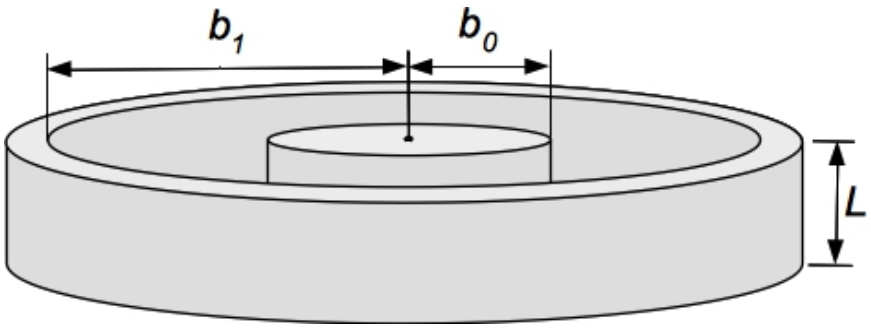

Figure 3.2: **Schematic of the annular resonator.** As mentioned in Figure 2.1, the dimensions are $b_0 = 0.407$", $b_1 = 0.888$", and $L = 0.126$", with L representing the actual depth of the MCNT powder.

data points as in minimizing the chi-squared value. These uncertainties were then used to propagate an error for the Q for each resonance.

The peaks in Figure 3.1 correspond to the third-sound speed; however, the values are in terms of the frequency. In order to convert these into an actual speed, the resonance structure must be calculated within the Plexiglas annulus that houses the packed MCNT powder, as shown in Figure 3.2. To do this, the wave equation,

$$\nabla^2 T = \frac{1}{c_3^2}\frac{\partial^2 T}{\partial t^2}, \tag{3.2}$$

was solved to account for the azimuthal, radial, and axial degrees of freedom[3] in which the temperature wave may propagate macroscopically. Using the ansatz

$$T(r, \theta, z, t) = T_0 f(r) g(\theta) h(z) e^{i\omega t}, \tag{3.3}$$

the wave equation is solved subject to "rigid" boundary conditions in the axial and

[3]The Laplacian in cylindrical coordinates was used:

$$\nabla^2 = \frac{1}{r}\frac{\partial}{\partial r}\left(r\frac{\partial}{\partial r}\right) + \frac{1}{r^2}\frac{\partial^2}{\partial \theta^2} + \frac{\partial^2}{\partial z^2}$$

.

radial directions—in which it is assumed that the temperature wave is at a node when it reaches the boundaries as the superfluid ceases to exist at the boundaries—and periodic boundary conditions in the azimuthal direction. Mathematically, the boundary conditions amount to restricting

$$\begin{aligned} \left.\frac{\partial T}{\partial r}\right|_{r=b_0,b_1} &= 0, \\ \left.\frac{\partial T}{\partial z}\right|_{z=0,L} &= 0, \\ T(\theta) &= T(\theta + 2\pi). \end{aligned} \tag{3.4}$$

Plugging in the ansatz, dividing through by T and rearranging, the wave equation reduces to

$$\frac{r^2}{f}\frac{\partial^2 f}{\partial r^2} + \frac{r}{f}\frac{\partial f}{\partial r} + \frac{1}{g}\frac{\partial^2 g}{\partial \theta^2} + \frac{r^2}{h}\frac{\partial^2 h}{\partial z^2} + \frac{\omega^2}{c_3^2}r^2 = 0. \tag{3.5}$$

To employ the separation of variables properly, the azimuthal and axial terms are set equal to suggestive constants. The ordinary differential equation in the azimuthal direction is written as

$$\frac{1}{g}\frac{d^2 g}{d\theta^2} = -m^2, \tag{3.6}$$

with the general solution

$$g(\theta) = G_1 \cos(m\theta) + G_2 \sin(m\theta).$$

Subjecting this solution to the azimuthal boundary condition in Equations 3.4, the azimuthal solution becomes

$$g(\theta) = G\cos(m\theta), \qquad (m = 0, 1, 2, \ldots). \tag{3.7}$$

Moreover, the ordinary differential equation in the axial direction is written as

$$\frac{1}{h}\frac{d^2h}{dz^2} = -k_z^2, \tag{3.8}$$

with the general solution

$$h(z) = H_1\cos(k_z z) + H_2\sin(k_z z).$$

Subjecting this solution to the axial boundary condition in Equations 3.4, the axial solution becomes

$$h(z) = H\cos(k_z z) = H\cos\left(\frac{n_z\pi}{L}z\right), \qquad (n_z = 0, 1, 2, \ldots). \tag{3.9}$$

Using Equations 3.6 and 3.8, plugging into Equation 3.5 and rearranging, Bessel's differential equation is found for the radial direction:

$$r^2\frac{d^2f}{dr^2} + r\frac{df}{dr} + \left[\left(\frac{\omega^2}{c_3^2} - k_z^2\right)r^2 - m^2\right]f = 0. \tag{3.10}$$

The general solution consists of the cylindrical Bessel function ($J_m(k_r r)$) and the Neumann function ($N_m(k_r r)$):

$$f(r) = F_1 J_m(k_r r) + F_2 N_m(k_r r). \tag{3.11}$$

Subjecting this solution to the radial boundary condition in Equations 3.4, it is seen that the Neumann function must be kept. The Neumann function is known to blow up as $r \to 0$. However, because of the annular nature of the resonator, the Neumann function is finite for $r \in [b_0, b_1]$. However, the boundary condition subjects the functions to the condition that

$$\left(\frac{\partial J_m(k_r b_0)}{\partial r}\right)\left(\frac{\partial N_m(k_r b_1)}{\partial r}\right) - \left(\frac{\partial N_m(k_r b_0)}{\partial r}\right)\left(\frac{\partial J_m(k_r b_1)}{\partial r}\right) = 0, \tag{3.12}$$

where the derivative with respect to r for each function is taken and then evaluated at the radial boundaries b_0 and b_1. For each value of m, this condition provides the values of k_r that satisfy it. With k_r obtained from finding the roots of Equation 3.12 and k_z derived from Equation 3.9, the frequency $f = \omega/2\pi$ at which the third-sound resonance occurs may then be related to the third sound speed, c_3, via the condition

$$c_3 = \frac{2\pi f}{\sqrt{k_r^2 + k_z^2}}. \tag{3.13}$$

As a note, Equation 3.13 is taken as the definition of k_r. This equation was used to convert the raw resonant-frequency data into the speed of third sound for all accumulated data points.

However, the conversion from the experimental frequency to the experimental third-sound speed is not necessarily the true third-sound speed. Since this surface wave is propagating across a powder of MCNTs—which not only contains the smaller scale grains of the actual tubes, but also the larger scale grains of the collections of tubes, as in Figure 2.4—the experimental speed will be smaller than the theoretical speed. Indeed, the theoretical speed, as in Equation 1.113, only considers propagation on a smooth surface without the presence of grains. As the wave propagates across the grainy substrate, it imparts momentum to the substrate, resulting in a reduction of the sound speed. As such, an index of refraction must be quoted to treat this reduction:

$$n_3 = \frac{c_3^{(\mathrm{th})}}{c_3^{(\mathrm{exp})}}. \tag{3.14}$$

Thus, if there is a desire to output the true theoretical sound speed, the right-hand side of Equation 3.13 must be multiplied by this index of refraction.

To obtain this index of refraction, one needs to obtain a value for the surface tortuosity, $\chi_{2\mathrm{D}}$, which is a measure of the tortuous path that the fluid is forced

to follow when restricted to the surface of the pore-space in the powder. The value of this surface tortuosity can be obtained from measurements of the index of refraction. [75] In fact, the index of refraction of third sound can be written in terms of this surface tortuosity as

$$n_3^2 = \chi_{2\mathrm{D}}. \tag{3.15}$$

To obtain an expression for the surface tortuosity, information regarding the porosity, ϕ, of the powder must be known. If $\mathcal{V}_{\mathrm{open}}$ is the amount of open volume present within a packed powder and $\mathcal{V}_{\mathrm{tot}}$ is the total amount of volume occupied by the powder, then the porosity of the powder is given by the ratio

$$\phi = \frac{\mathcal{V}_{\mathrm{open}}}{\mathcal{V}_{\mathrm{tot}}}. \tag{3.16}$$

The porosity for this MCNT powder, using the dimensions provided in Figure 3.2, was found to be $\phi_{\mathrm{MCNT}} = 0.82$ upon using the density of an individual MCNT, $\rho_{\mathrm{MCNT}} = 2.1$ g/cm^3, which is essentially the density of graphite. [76] However, knowledge regarding the critical porosity, ϕ_{c}, is also essential. This critical value represents the pore-space percolation threshold. This threshold can be understood in the following way, described by Reference [77]. Imagine taking a porous solid and allowing it to become progressively denser. Increasing this density will change the way in which the channels connecting the pore spaces will be interconnected. Indeed, some of the interconnections will surely be choked off, while others may get displaced to the exterior of the defined powder volume. The essential idea is that as the density is increased, the number of paths connecting one side of the powder with the other will be reduced. The porosity at which there is no longer a connected path from one side of the powder to the other is called the critical porosity, which represents this percolation threshold. Thus, the surface tortuosity, $\chi_{2\mathrm{D}}$, can be calculated using the power-law [78]

$$\chi_{2D} = B\phi(\phi - \phi_c)^{-\beta}, \tag{3.17}$$

where B is a constant dependent on the porous material and β is some number. It is unclear exactly how the percolation threshold can be empirically discovered using a MCNT powder.

3.2 Film Thickness and Number Density Calibration

A difficulty in making measurements of the helium adsorption on substrates is that the vapor pressure becomes very small, particularly when reaching sub-Kelvin temperatures. This can be seen by noting the metrological data compiled in the International Temperature Scale of 1990 (ITS-90) [79], which made use of the ^{3}He vapor pressure, in favor of ^{4}He, for proper precision, particularly below 1 K. However, it is still possible to detect the pressure of ^{4}He gas at sub-Kelvin temperatures by making use of an *in-situ* gauge that capacitively detects pressures. The vapor pressure of ^{4}He at 700 mK is about 2 μmHg, so that the minimum resolution of such a gauge must be good to roughly 0.1 μmHg. At 500 mK, the vapor pressure is about 10 nmHg.

The ultimate goal of the experiments on which this report is based required cooling the MCNT powder sample to temperatures at which a vapor-pressure reading would be impossible, even with the use of an *in-situ* detection apparatus. To bypass this issue, the adsorption profile was obtained at 1300 mK, which would then be used to navigate the helium coverage on the MCNT powder at lower temperatures. For this navigation to be uniform across the high-temperature and low-temperature systems, the same cell was used with the same gas-handling system. As such, the data for these temperatures could be easily connected.

The vapor-pressure data at high-temperature was also useful for determining the film thickness adsorbed on the outer diameter of the MCNTs. It follows from

standard thermodynamics that the useful thermodynamic potential for analyzing the coexistence between the liquid film and the gaseous vapor under these experimental conditions is the Gibbs free energy. Indeed, the conditions were of constant temperature and pressure, for which the Gibbs-free-energy change is zero. The Gibbs-Duhem relation reveals the nature of the Gibbs free energy (G)—defined in Equation 1.68—as the chemical potential (μ) per particle ($\mathcal{N}$), as in Equation 1.70. Because $\Delta G = 0$ across the liquid-gas interface, then the chemical potential of the vapor must be equal to the chemical potential of the film at the interface. For a flat substrate, the van der Waals (vdW) potential (per particle) for a helium atom a distance z above the substrate takes the form

$$U_{\text{flat}}(z) = -\frac{\alpha}{z^3}, \tag{3.18}$$

where α is the coupling strength between the liquid particle and the specific substrate under question. Thus, the chemical-potential balance between the vapor and the liquid in the flat-substrate case takes the form

$$k_{\text{B}}T \ln\left(\frac{P_0}{P}\right) = \frac{\alpha}{z^3}, \tag{3.19}$$

where $k_{\text{B}} = 1.381 \times 10^{-16}$ erg/K, P_0 is the saturated vapor pressure at the temperature T, and P is the vapor pressure in the experimental cell.

For the purposes of this experiment, the relevant geometry onto which the helium adsorbed was a cylindrical one. The vdW potential (per particle) between a spherical particle and a long, solid cylinder of radius R is given by Kirsch [80] as

$$U_{\text{scyl}}(z) = -\frac{9\pi}{4}\alpha\frac{R^2}{(R+z)^5}F_1^2\left[\frac{5}{2}, \frac{5}{2}; 2; \frac{R^2}{(R+z)^2}\right], \tag{3.20}$$

where F_1^2 is the Gaussian hypergeometric function and z denotes the (radial)

position of the helium atom from the cylinder surface. However, to modify this slightly, Kirsch also provides an integral representation of the potential for cases in which the cylinder is not solid, but rather annular. This is more favorable based upon the MCNT images seen in Figure 2.7. Labeling the inner radius as R_{in} and the outer radius as R_{out}, the vdW potential for the cylinders under question takes the form

$$U_{\text{cyl}}(\alpha, R_{\text{in}}, R_{\text{out}}, z) = -\frac{9\pi\alpha}{4(R_{\text{out}}+z)^5}\int_{R_{\text{in}}^2}^{R_{\text{out}}^2} d(\xi^2) F_1^2\left[\frac{5}{2}, \frac{5}{2}; 1; \frac{\xi^2}{(R_{\text{out}}+z)^2}\right], \quad (3.21)$$

where ξ is measured from the center of the cylinder and covers the range of radial distances in a MCNT where the carbon atoms live (i.e., $\xi \in [R_{\text{in}}, R_{\text{out}}]$), and z denotes the position of the helium atom as measured from the outer radius of the cylinder.

On top of the modified vdW potential to which the helium atoms are subjected when adsorbing onto the MCNT, it also costs the helium atoms energy to maintain a curved surface when forming a liquid film while adsorbing onto the MCNTs, which have a very small radius of curvature. In other words, the effects of surface tension must also be factored in order to properly describe the chemical potential of the film. This is done by using the appropriate Kelvin equation to account for the change in vapor pressure that accompanies a curved liquid/vapor interface. The full chemical-potential balance for this cylindrical case, upon including surface tension effects, becomes

$$k_B T \ln\left(\frac{P_0}{P}\right) = -U_{\text{cyl}}(z) - \frac{\sigma m_4}{\rho(R_{\text{out}}+z)}, \quad (3.22)$$

where σ and ρ are the surface tension and mass density, respectively, of the liquid-helium film, and $m_4 = 6.646 \times 10^{-24}$ g is the mass of the ^{4}He atom. At $T = 1.300$ K, $\sigma = 0.3397$ dyne/cm, and $\rho = 0.1451$ g/cm^3. The pressures were

obtained by experimentally measuring the pressure difference between the bath and the cell (i.e., $\Delta P = P_0 - P$), and taking note of the bath pressure P_0 when the cell pressure was zero. Inputting the cell and bath pressures into Equation 3.22, the film thickness can be calculated.

The chemical-potential balance can be modified by noting that the preliminary film might not necessarily be in a liquid state when adsorbing directly onto the substrate. As can be seen in Figure 1.2, ^{4}He becomes a solid with roughly 25 bars of pressure applied around or below 1 K. The vdW attraction is strong enough to solidify these initially adsorbed helium atoms. As a result, the film is not a liquid until two initial solid layers are present on the graphitic substrate [81]. This then modifies the adsorption a bit, as the relevant liquid helium film is not adsorbing onto the substrate directly, but rather is adsorbing onto a pseudosubstrate of solid helium. Cheng and Cole [82] modeled a multilayer film by observing the vdW interaction of the liquid-helium film with the actual substrate (s), the solid-helium pseudosubstrate (ps), and the liquid adsorbate (a).[4] The multilayer film was modeled on a flat substrate, defining a solid region of thickness D_0 and a liquid region of thickness d'. The total film thickness is then $d = D_0 + d'$. The modified vdW potential of the newly adsorbed liquid atoms at a thickness d' above the solid layer in this multilayer film is then written as

$$U'_{\text{flat}}(d') = -\frac{\alpha_{\text{s}}}{(D_0 + d')^3} - \frac{\alpha_{\text{ps}}}{d'^3} + \frac{\alpha_{\text{ps}}}{(D_0 + d')^3} + \frac{\alpha_{\text{a}}}{d'^3}. \tag{3.23}$$

Upon removing a factor of d'^3 from each denominator in Equation 3.23, the form reduces to the Cheng and Cole modification reported in Reference [55]

$$U'_{\text{flat}}(d') = -\frac{\alpha(d')}{d'^3}, \tag{3.24}$$

with the definition

[4] This work by Cheng and Cole was described by Zimmerli *et al.* [55].

$$\alpha(d') \equiv \alpha_{\rm ps} - \alpha_{\rm a} + (\alpha_{\rm s} - \alpha_{\rm ps})\left(1 + \frac{D_0}{d'}\right)^{-3}. \tag{3.25}$$

At the time of this report, there is no evidence in the literature as to the modeling of a multilayer film on arbitrary geometries, and how such a model would change the vdW coupling parameter, α, for an adsorbed helium film on that geometry.[5] However, the result of the Cheng and Cole theory, at least based upon Reference [55], is that the modification accounts for an extra layer that would otherwise not be accounted for under the use of the Frenkel-Halsey-Hill (FHH) adsorption theory [83–85] . The essential idea of the FHH theory, as it applies to ^{4}He, is that each layer of helium coating a substrate is 3.58 Å. However, this theory presumes that the adsorbed helium film is structureless, so that this value for the layer thickness should really only be applied for a film adsorbing onto an amorphous substrate.[6] However, the structure of carbon atoms is anything but amorphous (as is the case in graphite), and the way in which the helium film adsorbs must be distinguished between amorphous and crystalline substrates. [86] Each concentric nanotube shell used to form the multiple layers of the MCNT is a curled-up graphene sheet, thus displaying a regularized honeycomb structure over macroscopic length scales. [87] In this sense, the adsorbed helium film on a carbon substrate can undergo, in essence, epitaxial growth—both as a liquid [55] and even as a solid [88]—exhibiting a multitude of phases as a function of coverage within each layer [89]. Such layer-by-layer growth is not limited to carbon substrates,

[5] A guess at doing this, based on what has been reported thus far, would be to use Equation 3.21 for each of the annular regions upon which the liquid film adsorbs. Taking into account the annular carbon substrate and the annular solid-helium substrate, a modification could possibly take the form

$$U'_{\rm cyl}(d') = U_{\rm cyl}(\alpha_{\rm s}, R_{\rm in}, R_{\rm out}, d') + U_{\rm cyl}(\alpha_{\rm ps}, R_{\rm out}, R_{\rm out} + D_0, d'),$$

since Equation 3.21 seems to suggest the effective potential to be the sum of the potentials in the different regions.

[6] Technically, it is a bit of a misnomer to apply the idea of "layers" to such an amorphous substrate, as the adsorbed film does not necessarily grow in layers. Indeed, the notion of layers on such disordered substrates is simply statistical in nature. However, this nomenclature is readily used throughout the literature.

but has been seen, for instance, on solid hydrogen substrates, which also exhibit regular crystalline structure. [90, 91]

Along with the crystalline order in graphitic substrates, the helium-carbon vdW interaction is rather strong compared to other substrates. [92] This fact is also important in setting the stage for the various exotic phases that are seen as a function of helium coverage within each layer, which has been studied very extensively over many decades [93–96], including recently in various computer simulations [97–99] in the wave of effort that was generated in the supersolid-helium craze [100].

The strength of the vdW interaction, along with the crystalline order in the substrate, sets the stage for the helium adsorption to be rather different than as described by the FHH model. The helium layers closest to the carbon substrate are highly compressed, and the layer thickness approaches the FHH value when the film is sufficiently thick. [55] The first and second (solid) layers have a density that is 1.5 and 1.1 times the usual density of bulk liquid helium, respectively. As a result, the first two layers have a total thickness of 4.42 Å, which—along with the less-compressed layers on top—amounts to the FHH model's under-representation of the number of layers by about one full layer. Taking this FHH modification into account and applying the chemical-potential balance in Equation 3.22 for the high-temperature results of this study, the superfluid onset was seen to occur between the fourth and fifth layer-completions for the study on the MCNT powder at 1.300 K. Since the indicative sign of layer completion came as a result of maxima in the third-sound profile as a function of coverage—to be discussed shortly—the fifth-layer completion occurred after the onset coverage for 1.300 K. This particular result was one of the two elements that dictated the coverage scale adopted for this study.

Although reporting coverage in terms of the unit of "layers" is common (e.g., Reference [95]), the literature for helium adsorption on Grafoil (e.g., References

[55,89,96]) more readily uses the unit of "areal number density" (i.e., the number of helium atoms per unit area of available surface). From the experiments by Zimmerli *et al.*, the second layer completes at a number density of 0.204 atoms/Å^2, while subsequent layers complete every 0.076 atoms/Å^2. This result was the second element used to establish the coverage scale in these findings, which was incorporated by using a calculation of the surface area of the MCNT powder that would complement these areal-number-density values at layer completion.

Both experimental [101] and theoretical [76] studies involving the structure of MCNTs readily showcase the uniform way in which these multi-wall tubes are built from a superposition of concentrically stacked Single-wall Carbon Nanotubes (SCNTs), irrespective of the diameter or length of the tubes. In these studies, the inter-shell separation in the MCNTs is taken to be exactly the same as the separation between adjacent graphene sheets in normal graphite, namely $d_{\mathrm{S-S}} = 3.40$ Å. Taking the specific surface area of a SCNT (i.e., the surface area per unit mass) as $s_{\mathrm{SCNT}} = 1315$ m^2/g—which is the same as the specific surface area of a single graphene sheet (determined by the carbon-carbon bond length and lattice structure of such a sheet) [102]—the surface area of a single MCNT with ν walls, an outer-diameter d_{out}, and length ℓ_{MCNT} is given by

$$M_{\mathrm{MCNT}} = \frac{1}{s_{\mathrm{SCNT}}} \pi \ell_{\mathrm{MCNT}} \left(\nu d_{\mathrm{out}} - 2 d_{\mathrm{S-S}} \sum_{i=1}^{\nu-1} i \right). \tag{3.26}$$

By weighing the Plexiglas resonator before and after packing the MCNT powder (i.e., the mass difference between Figures 2.1b and 2.1f without the plastic wrap), the mass of the powder was determined to be $M_{\mathrm{powder}} = 0.75$ g. Taking the surface area of a MCNT to be $S_{\mathrm{MCNT}} = \pi \ell d_{\mathrm{out}}$, the surface area of the powder[7] then becomes

[7]It is assumed that the available surface area for the adsorbed helium is limited to the outside of the nanotubes across the powder, for reasons to be discussed later.

$$S_{\text{powder}} = \frac{M_{\text{powder}}}{M_{\text{MCNT}}} S_{\text{MCNT}}, \tag{3.27}$$

which is independent of the (average) length ℓ_{MCNT} of each MCNT. In this expression, the outer diameter, d_{out}, and the number of walls, ν, in Equation 3.26 represent average quantities across the powder.

The surface area for adsorption on the cylindrical geometry changes as a function of the helium film thickness, since the circumference of a cylinder scales as the diameter. Thus, the surface area for each layer must be modified to take this effect into account. Implementing this correction to properly account for the helium coverage, the necessary values for the average outer diameter and wall number of each MCNT within the powder must be $d_{\text{out}} = 24$ nm and $\nu = 11$ walls, respectively, in order to satisfy the aforementioned coverage scale in Reference [55]. Although the value for the outer diameter seems to be consistent with the SEM and TEM images in Figures 2.5 and 2.7, the number of walls suggest an implied (average) inner diameter of $d_{\text{in}} \approx 17$ nm. This inner-diameter is seemingly at odds with the images in Figures 2.6c and 2.6d which suggest a value that is about a factor of two smaller.[8]

One of the reasons for assuming that the helium adsorption only takes place on the outside surface of the nanotubes is because of the extrapolation of the coverage scale in Reference [55] to low coverages. Indeed, having established the layer-completion values for the third, fourth, and fifth layers using the third-sound data in this study, in conjunction with the output of Equation 3.22 at 1300 mK, going down to zero coverage did not leave a surplus of helium atoms. In other words, this extrapolation took into account all of the helium atoms added to

[8] Albeit, those images are not necessarily a complete representation of the distribution of inner-diameter sizes, especially since the images could also be obscured by diffraction effects, as can be seen in the "fringes" upon closer inspection of Figures 2.6c and 2.6d. Such fringes amount to an overestimation of the number of walls when included in the counting scheme. Of course, it is unclear in such images exactly where the cutoff for the counting of the walls should be in the first place.

the cell in perfect correspondence with the suggested scale. Had an excess been present, it could have been concluded that these atoms adsorbed to the interior of the uncapped MCNTs. Even with a cylindrical pore-size as low as 1.8 nm, the helium atoms would not be deterred from adsorbing into such a cage, even when considering the high ^{4}He zero-point energy. [70] However, assuming any other value of d_{out} and ν would be incommensurate with the layer-completion values.

3.3 High-Temperature Results and Discussion

The adsorption isotherm for the helium film adsorbed on the MCNT powder at 1300 mK is shown in Figure 3.3. At low-enough temperatures, the completion of a layer will show up in the adsorption profile as steps, with a substantial pressure rise occurring beyond the completion and comparatively minimal pressure change on the verge of layer completion. Indeed, while the coverage is close to completing, the helium atoms adsorbed become immobilized, leading to a constancy in the vapor pressure. The step-like features come from this effect, as can be seen in the adsorption profile in Reference [103], which is shown in Figure 3.4. The use of the *in-situ* pressure gauge is a necessity to detect such small pressure changes at such low pressures, and to detect the step-like features in the adsorption profile at sub-Kelvin temperatures.

Figure 3.5 is a plot of the third-sound speed and Q as functions of the helium coverage for low coverages. The data points have been combined for the various excitation methods used to create the third-sound waves. The 0° and 90° vibrations refer to the repeated hitting of the topmost flange of the cryostat with a hammer at different locations on the circular flange, as discussed in Section 2.1. These sweet spots provided the best results throughout the course of the experiment. However the heater was less invasive in exciting resonances when the film was thick enough to suppress desorption in thermally driving third sound.

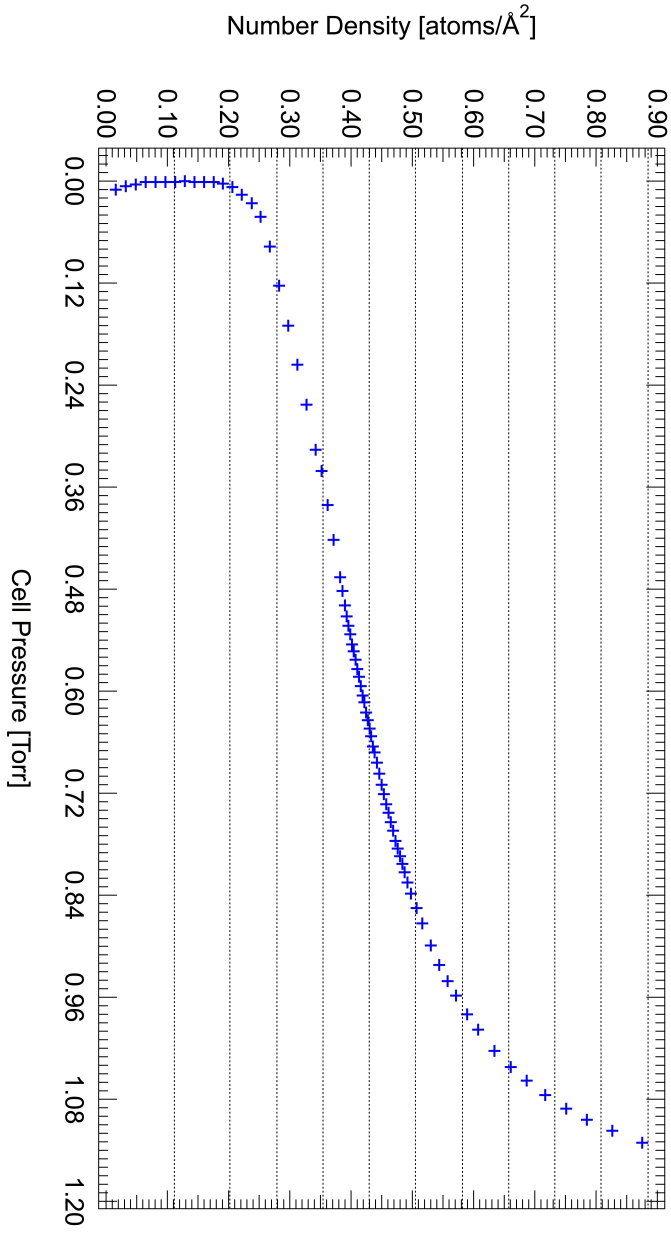

Figure 3.3: **Helium adsorption isotherm at 1300 mK.** Dashed, horizontal lines indicate layer completion. The spacing between layers becomes uniform beyond the 2nd-layer at 0.203 atoms/Å^2 since the film is no longer strongly compressed. The pressure begins to rise with coverage beyond the 2nd-layer completion, most notably indicating liquid-film deposition. The steep rise in the coverage around 1 Torr is the rise towards the SVP value of the bulk liquid.

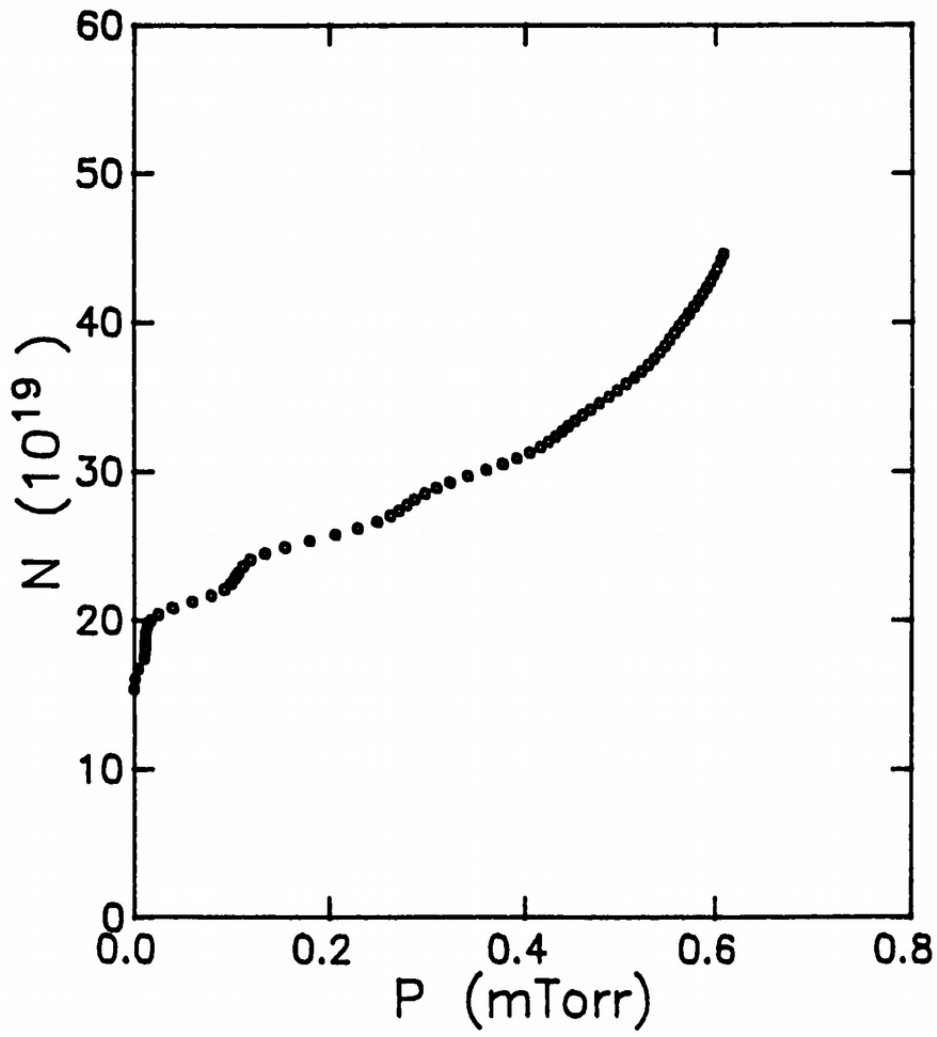

Figure 3.4: **Adsorption isotherm of ^{4}He on graphite foam at 640 mK.** The plot is from Reference [103], which showcases the number of helium atoms, N, admitted into the experimental space as a function of the pressure reading, P, on the *in-situ* pressure gauge. The step at 16.5×10^{19} atoms indicates the completion of the 3rd layer.

The rise to a maximum in c_3 is expected on account of finite-size broadening in the KT transition, as discussed in Section 1.6. Indeed, since the superfluid current is not completely screened by a true vortex-unbinding transition, the superfluid density does not abruptly drop to zero at T_{KT}. The reason there is a maximum in the sound speed stems from a competition between the superfluid density and the vdW attraction. On the one hand, increasing the film thickness from the superfluid transition temperature, T_{c}, makes the superfluid density gradually increase as the vortex-antivortex pairs have less of a screening effect as the film thickness is built up to larger values. On the other hand, the vdW potential is becoming smaller for the newly adsorbed film, as the film thickness is now larger and, thus, farther away from the substrate. The superfluid density increases more rapidly than the decrease in the vdW potential for the film, resulting in a maximum in the third-sound speed. Once the superfluid density reaches its maximal value, the reduction in the vdW potential dominates the c_3 profile, resulting in the reduction of the sound speed.

The third-sound profile sees a marked change at larger values of coverage, as is shown in Figure 3.6. This increase in the sound speed is probably attributed to the film's preferred condensation—at high-enough coverages—at regions where neighboring nanotubes touch, a schematic of which is presented in Figure 3.7. This effect, known as capillary condensation, has been studied in superfluid films adsorbed on Al_2O_3 powders consisting of spherical and ellipsoidal powder grains. [104] In this study, an increase in the sound speed was observed, which was explained by modeling the adsorbed film at the boundary where two grains touched. The surface-tension force was the dominant force at high-enough helium coverages, and it was responsible for increasing the sound speed on account of its anti-restoring nature.

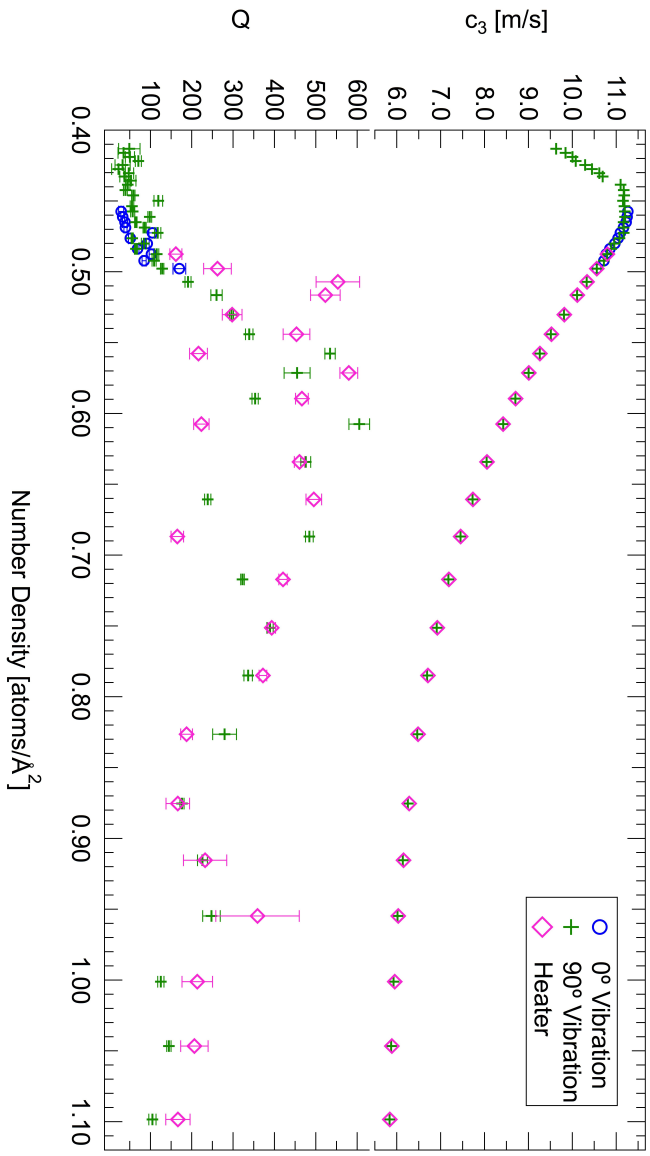

Figure 3.5: c_3 **and** Q **as functions of the** ^{4}**He coverage at 1300 mK on the MCNT powder.** The low Q near the superfluid onset indicates substantial attenuation due to topological excitations. The rise up to the maximum in c_3 represents the increase in the superfluid density as it is gradually built up from a lessened screening from the vortex-antivortex pairs above the critical onset film thickness. The reduction in the sound speed beyond the maximum is due to the reduction of the vdW potential. The onset coverage is taken as 0.413 atoms/Å^2.

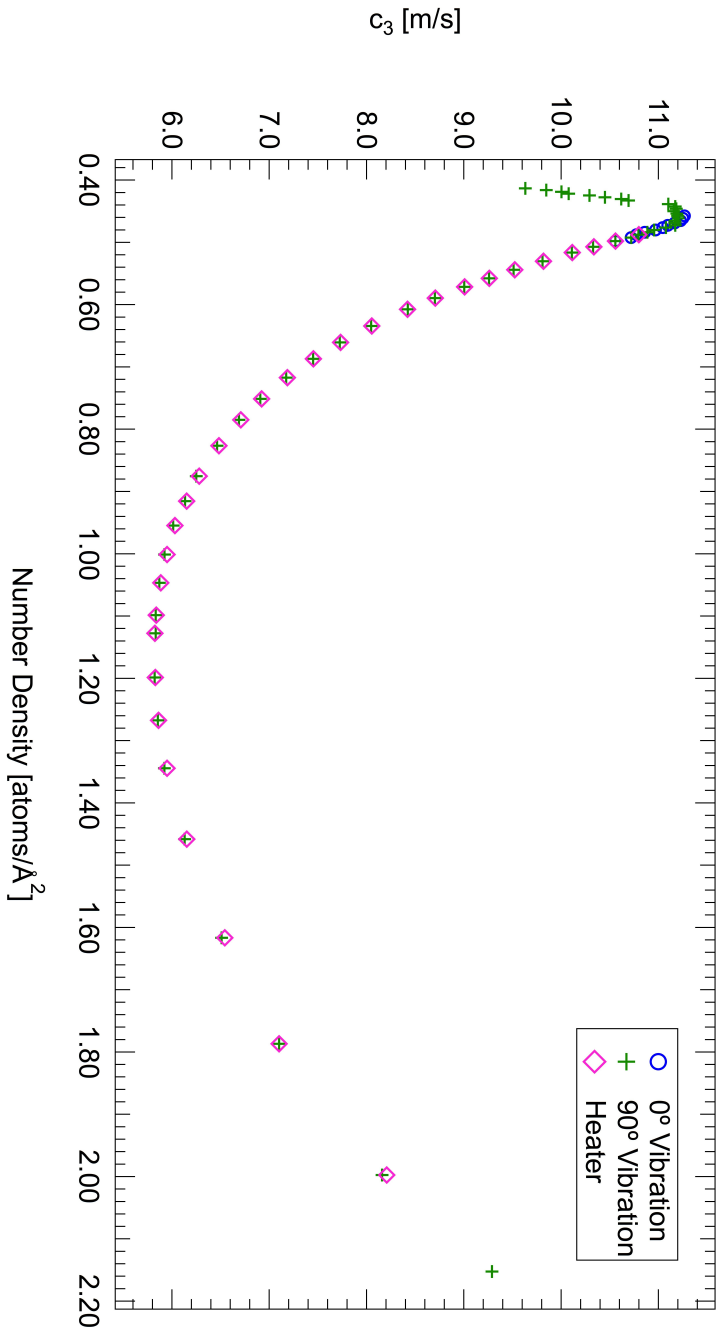

Figure 3.6: **Third-sound speed as a function of the ^{4}He coverage at 1300 mK on the MCNT powder.** After the decrease in c_3 due to the reduction of the vdW potential in the building up of the film, the speed begins to increase as modeled in Al_2O_3 powders in Reference [104]. This is likely due to capillary condensation where the MCNTs touch.

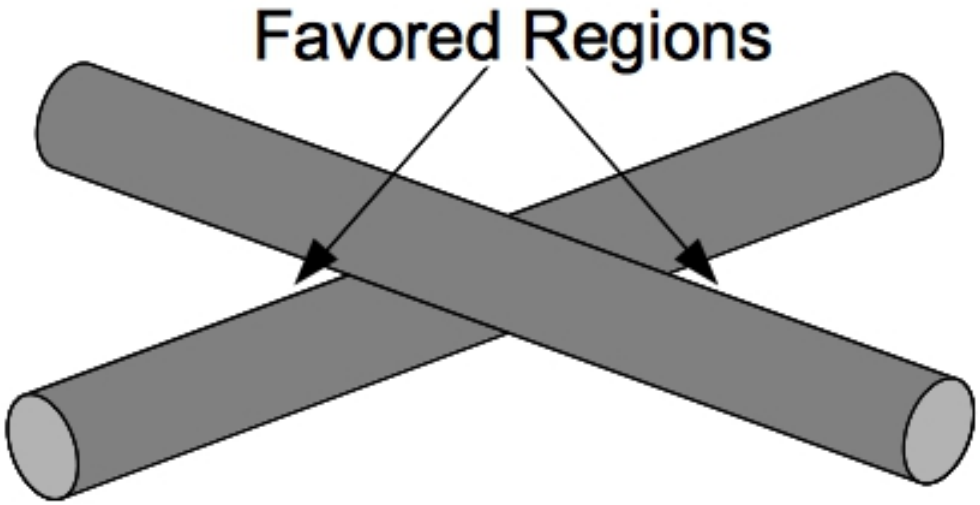

Figure 3.7: **Model for capillary condensation on the cylindrical geometry.** Although the nanotubes' outer region has an unfavorable curvature both due to a reduced vdW attraction and surface tension, the region between nanotubes presents a favorable, confining geometry to where helium atoms are likely to be drawn. The film thickness ceases to build up across the cylinders uniformly and is, instead, deposited into the regions where the tubes touch, resulting in an increase in the surface-wave's speed.

3.4 Low-Temperature Results and Discussion

Layering effects were not readily seen at 1300 mK, but at sub-Kelvin temperatures these effects were more prevalent. In particular, the profile of the third-sound speed displays oscillatory behavior, which is directly related to the hardening and softening of the adsorbed superfluid film, particularly between the 3rd and 5th layer-completion coverages. This behavior has been seen on graphite foam [55]—as shown in Figure 3.9—and modeled theoretically in a study of multilayer film growth on various substrates showing crystalline order [105]. This can be seen in Figure 3.8, which is a plot of the third-sound speed as a function of coverage at an approximately constant temperature of 250 mK.[9] The adsorbed helium film displays an oscillation in the (2D) isothermal compressibility [55, 89], defined by

$$K_T = \frac{1}{n^2 T} \frac{\partial n}{\partial \ln(P)},$$

where n is the (areal) ^{4}He number density, T is the temperature, and P is the pressure as measured by the *in-situ* gauge. Indeed, when the film hardens when getting close to the completion of a layer, the compressibility decreases—since an already compressed film is difficult to compress further—while when the film softens, the compressibility increases—since such a film has the potential to be compressed further.

The behavior of the third-sound speed can be characterized rather well by observing the trends in the compressibility. Indeed, a discussion of the relationship can be extracted from a discussion of how the generic sound speed in a bulk fluid

[9] It was difficult to keep the temperature at a fixed value. It was necessary to excite the third-sound resonance by shaking the shaker at a large drive level, particularly when the Q of the resonance signal was low. This violent shaking would inevitably make the entire dilution-fridge assembly shake, since the experimental cell was rigidly coupled to the mixing chamber to ensure optimal thermal contact. This would heat up the mixing chamber both because of a presumed increase in the heat load to the mixing chamber from the heating-up of the magnet, but also because of a nonequilibrium perturbation set forth on the phase-separated mash. However, the mixing chamber was able to robustly maintain a temperature around 250 mK for the most part, allowing for an approximate isothermal investigation of c_3 as a function of the helium coverage.

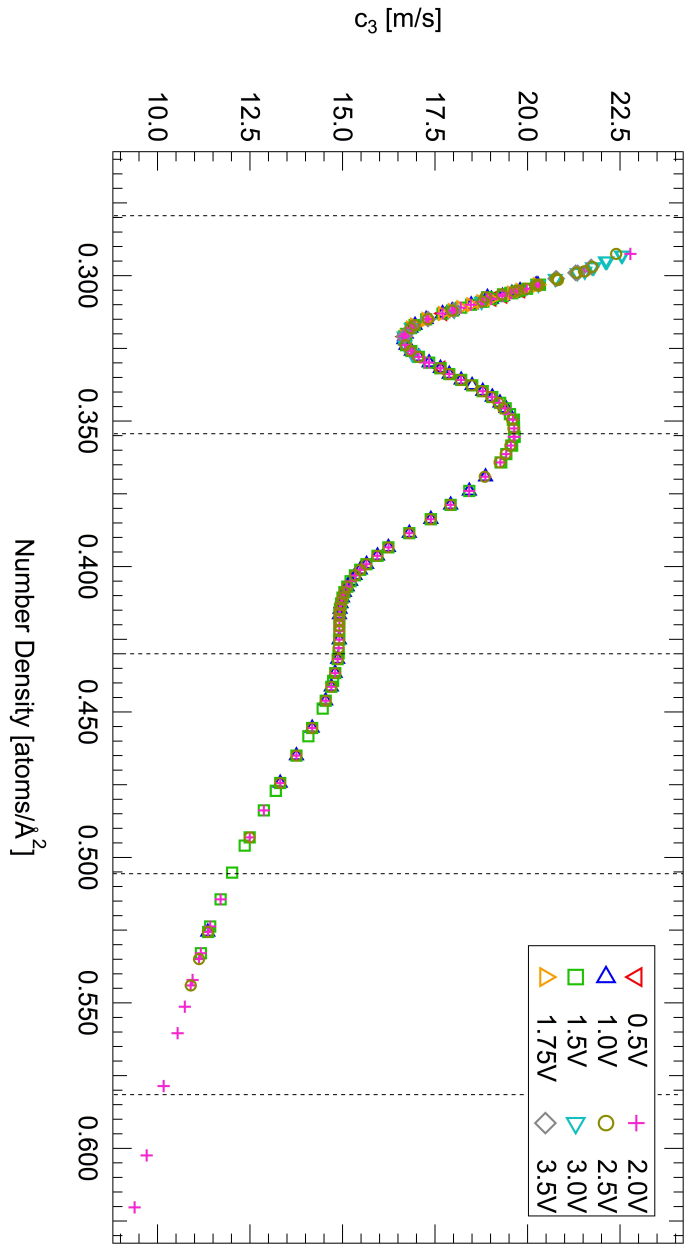

Figure 3.8: **Third-sound speed as a function of coverage at 250 mK.** c_3 oscillates at the lowest coverages with layer periodicity. The vertical lines indicate layer completion, starting from the 3rd-layer completion. The onset coverage is 0.293 atoms/Å^2. c_3 is a maximum at the 3rd (unseen) and 4th layer completions, with a suppressed maximum at the 5th layer completion where the decrease in the film compressibility is dominated by the reduction in the vdW potential.

(denoted as first sound in superfluid helium) depends on the compressibility. As in Equation 1.92a, the speed of first sound can be written as

$$c_1^2 = \left(\frac{\partial P}{\partial \rho}\right)_S.$$

The bulk-liquid density ρ may be rewritten in terms of the specific volume (i.e., volume of the bulk fluid per unit mass), v, as $\rho = 1/v$. Since $d(1/v) = -(1/v^2)dv$, then

$$c_1^2 = -v^2\left(\frac{\partial P}{\partial \rho}\right)_S = \frac{v}{\kappa_S},$$

where κ_S is the isentropic compressibility (using the specific entropy, s). Using a Jacobian transformation, the isentropic compressibility may be written in terms of the isothermal compressibility,

$$\begin{aligned}
\kappa_S \equiv -\frac{1}{v}\left(\frac{\partial v}{\partial \rho}\right)_S &= -\frac{1}{v}\frac{\partial(v,s)}{\partial(P,s)} \\
&= -\frac{1}{v}\frac{\partial(v,s)/\partial(P,T)}{\partial(P,s)/\partial(P,T)} \\
&= -\frac{1}{v}\left(\frac{\partial T}{\partial s}\right)_P\left[\left(\frac{\partial v}{\partial P}\right)_T\left(\frac{\partial s}{\partial T}\right)_P - \left(\frac{\partial v}{\partial T}\right)_P\left(\frac{\partial s}{\partial P}\right)_T\right] \\
&= -\frac{1}{v}\left[\left(\frac{\partial v}{\partial P}\right)_T - \left(\frac{\partial T}{\partial s}\right)_P\left(\frac{\partial v}{\partial T}\right)_P\left(\frac{\partial s}{\partial P}\right)_T\right].
\end{aligned}$$

From the (specific) Gibbs-free-energy differential (presuming no particle exchange, which is completely warranted for a bulk liquid), $dg = -sdT + vdP$, we have that

$$\left(\frac{\partial g}{\partial T}\right)_P = -s$$

and that

$$\left(\frac{\partial g}{\partial P}\right)_T = v.$$

Since g is a thermodynamic potential, the mixed partial derivatives must be equal. As a result, it must be true that

$$\left(\frac{\partial v}{\partial T}\right)_P = -\left(\frac{\partial s}{\partial P}\right)_T.$$

Using this, along with the definition of the specific heat capacity at constant pressure,

$$\mathcal{C}_P = T\left(\frac{\partial s}{\partial T}\right)_P,$$

the isentropic compressibility is rewritten as

$$\begin{aligned}\kappa_S &= -\frac{1}{v}\left[\left(\frac{\partial v}{\partial P}\right)_T + \frac{T}{\mathcal{C}_P}\left(\frac{\partial v}{\partial T}\right)_P^2\right] \\ &= -\frac{1}{v}\left(\frac{\partial v}{\partial P}\right)_T - \frac{T}{v\mathcal{C}_P}\left(\frac{\partial v}{\partial T}\right)_P^2 \\ &= \kappa_T - \frac{T}{v\mathcal{C}_P}\left(\frac{\partial v}{\partial T}\right)_P^2.\end{aligned}$$

Finally, defining the volumetric thermal expansion coefficient, α_V, as

$$\alpha_V \equiv \frac{1}{v}\left(\frac{\partial v}{\partial T}\right)_P,$$

the relationship between the isentropic and isothermal compressibilities becomes

$$\kappa_S = \kappa_T - \frac{Tv\alpha_V^2}{\mathcal{C}_P}. \tag{3.28}$$

Thus, using Equation 3.28, the first-sound speed may be written in terms of the isothermal compressibility as

$$c_1^2 = \frac{v}{\kappa_T - \frac{Tv\alpha_V^2}{\mathcal{C}_P}}. \tag{3.29}$$

Although this analysis cannot be completely applied to the 2D film, Equation 3.29 can be used to understand the overarching inverse relationship between the third-sound speed, c_3, and the (2D) isothermal compressibility, K_T. Indeed, Figure 3.9—taken from Reference [55]—showcases this relationship, where it is seen that a maximum in c_3 corresponds to a minimum in K_T, and a minimum in c_3

roughly corresponds to a maximum in K_T. The minima in the compressibility, along with the maxima in the sound speed, align perfectly with the completion of a layer. The maxima in the compressibility and the minima in the sound speed do not occur at the half-layer mark, but are slightly offset from that coverage.

The sound-speed was the only means by which the effects of layer-by-layer growth were seen in this study of ^{4}He adsorption on the MCNT powder. However, the Q also showed some interesting features as a function of the coverage, as can be seen in Figure 3.10. At the Q minima seen at 0.306 and 0.344 atoms/Å^2, there was much difficulty in trying to capture a signal above the noise, and it was necessary to ramp up the shaker amplitude to pick up the resonance. It is not entirely clear why there was significant attenuation at these coverages. In the plot of c_3 and Q at 1300 mK (Figure 3.5), there was significant attenuation around the onset region. At 250 mK, it was almost impossible to get a signal above the noise at the onset coverage of 0.290 atoms/Å^2. There seems to be a trend towards lower values of Q around this coverage in both drive levels shown in Figure 3.10, but even with drive levels above the ones shown, there was very little semblance of a resonance peak in this region. If 0.290 atoms/Å^2 is the onset coverage at this temperature, it is unclear why the Q jumps to such high values after such a small increase in the coverage (e.g., at 0.300 atoms/Å^2).

The coverage of 0.290 atoms/Å^2 becomes somewhat more anomalous in its identity as the onset coverage when looking at the profile of c_3 as a function of temperature at a fixed coverage near this region. Indeed, it was necessary to build up the coverage slightly in order to investigate the temperature dependence of the sound speed, as the signal was very difficult to extract near the onset. In fact, raising the shaker amplitude proved detrimental at this point, since the temperature would run away to much higher values very rapidly, not allowing for extraction of an isothermal FFT profile. As can be seen in Figure 3.10, the Q was more manageable at a coverage of around 0.300 atoms/Å^2, which was where the

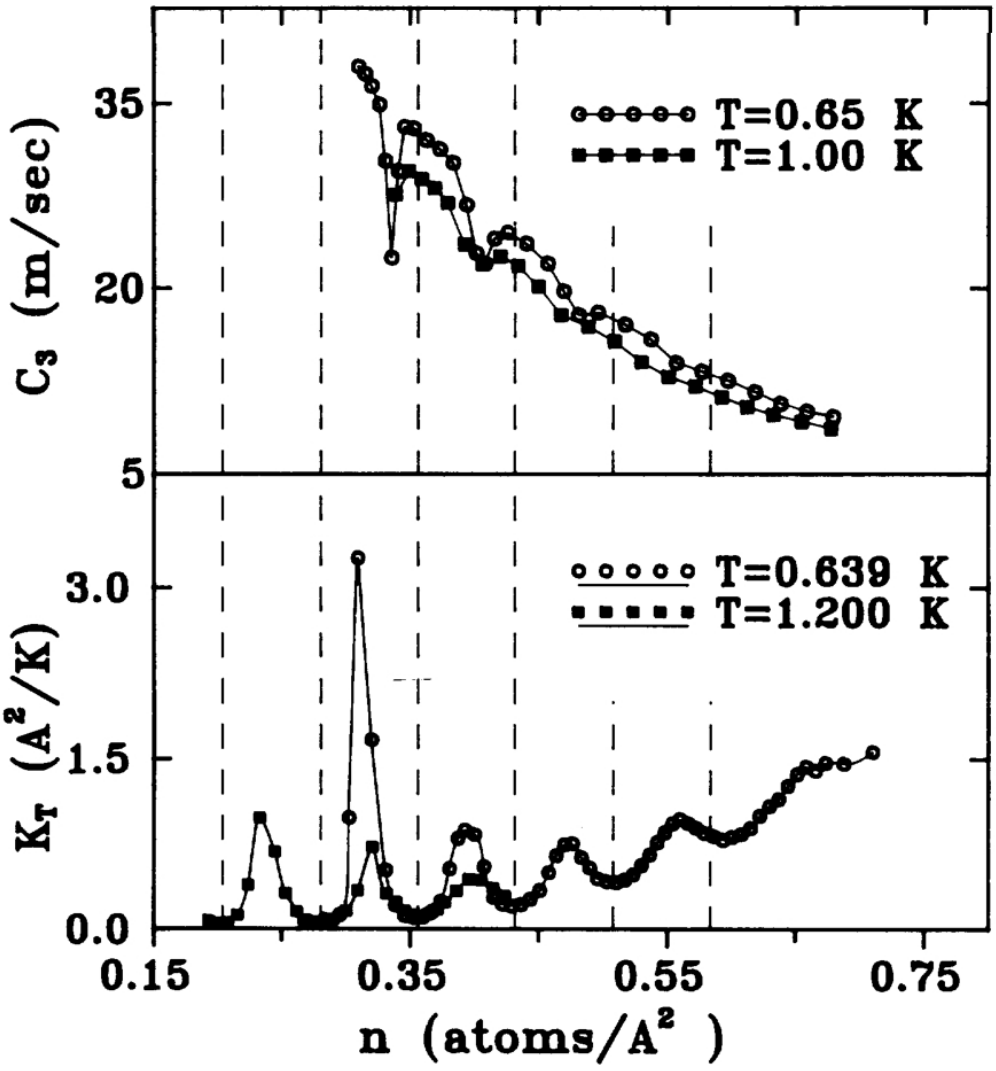

Figure 3.9: **Third-sound speed and isothermal compressibility of the ^{4}He film on graphite foam.** The plot is from Reference [55], which showcases c_3 and K_T as functions of the ^{4}He coverage. The dashed vertical lines indicate layer-completion coverages, starting from the completion of the 2nd layer. Note that the change for both the compressibility and for the third-sound speed is more dramatic for the lower-temperature data. Moreover, note that the minima in K_T and the maxima in c_3 align very well with the layer-completion coverages, while the maxima in the compressibility and the minima in the sound speed occur slightly before and slightly after the half-layer-completion points, respectively.

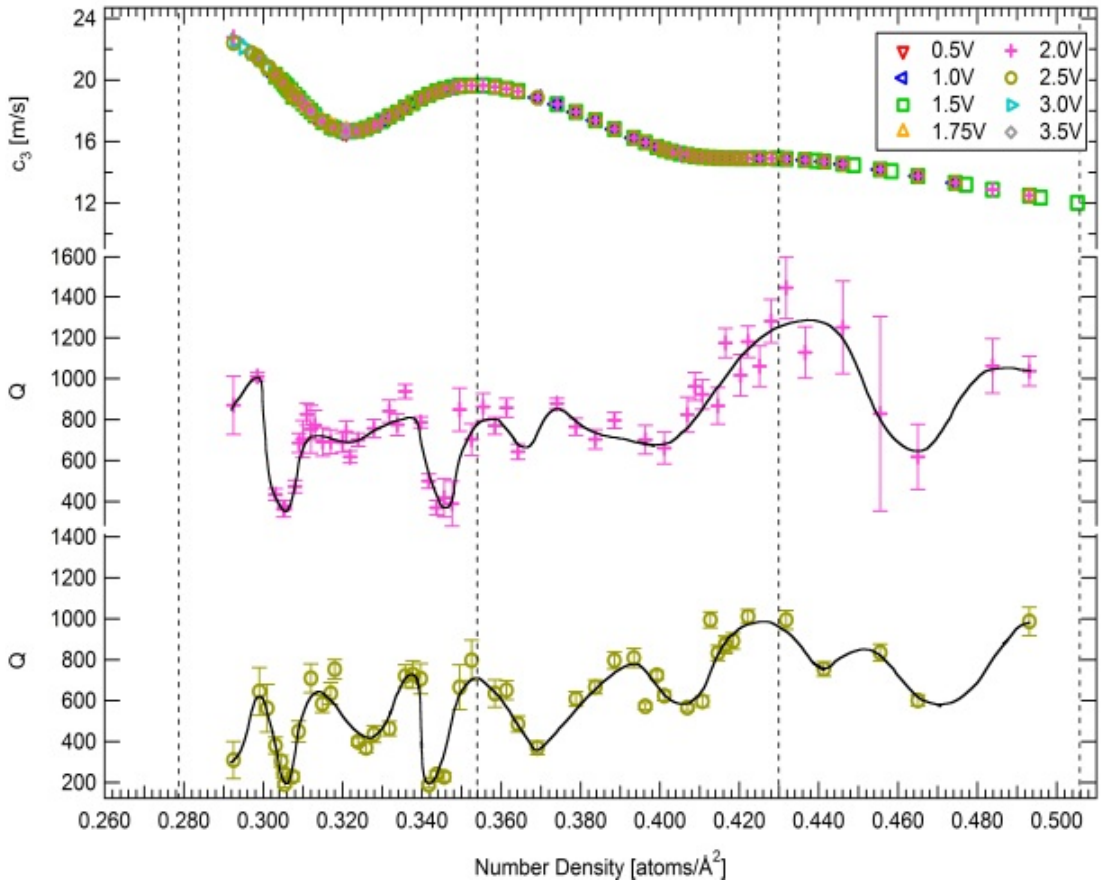

Figure 3.10: c_3 **and** Q **as functions of** ^{4}**He coverage at 250 mK.** The Q is plotted as a function of coverage for two different drive levels (2.0 V and 2.5 V) for the shaker. The Q has local minima at 0.306 and 0.344 atoms/Å^2, indicating an interesting attenuation pattern that is not commensurate with half- or full-layer-completion points. However, there seems to be a rise to a local maximum in the Q at the 4th and 5th layer completions. The solid line running through each plot of Q is meant for visual enhancement of the witnessed trends.

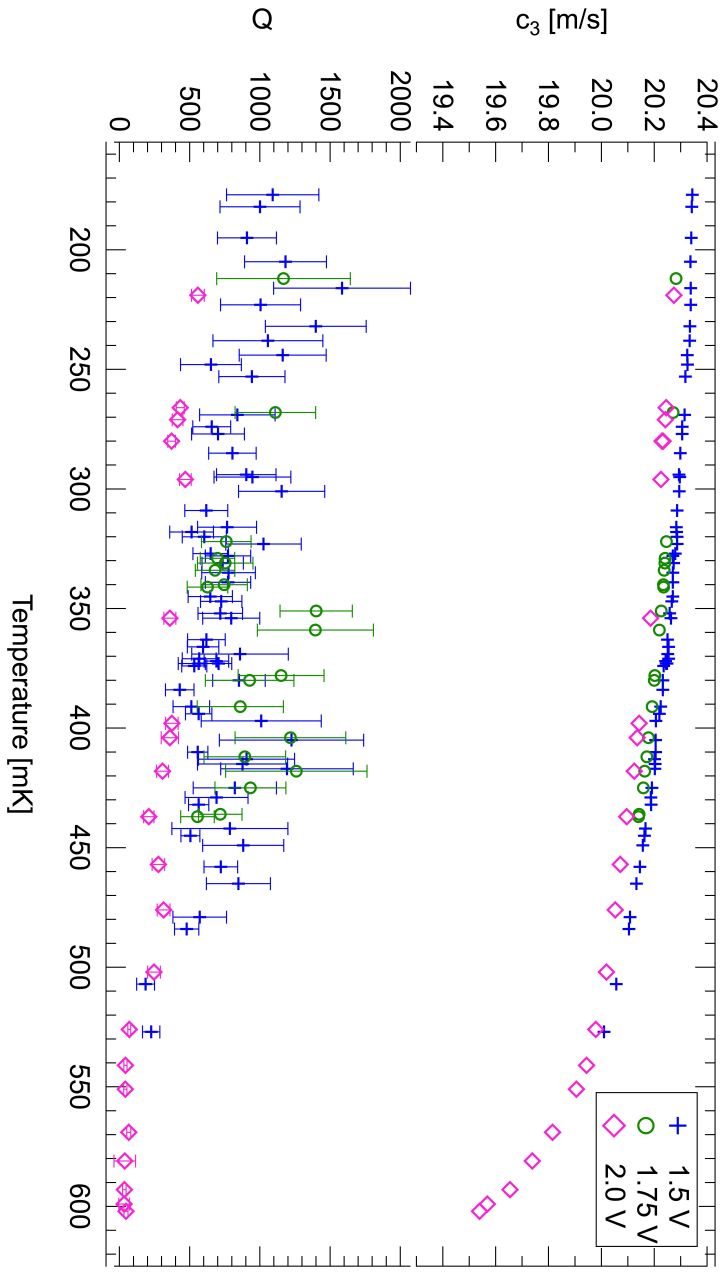

Figure 3.11: **Temperature sweep at a coverage of 0.303 atoms/Å².** The drop in the Q occurs at around 520 mK, which is taken as T_{KT} for this particular coverage.

first temperature sweep was performed. The result of this sweep, specifically at a coverage of 0.303 atoms/Å^2, is shown in Figure 3.11.

One of the strange features of this temperature sweep was its rather high KT onset temperature. In other words, a small change in the coverage from the presumed onset region—which one would assume to have a superfluid onset around 250 mK and, thus, a KT onset temperature slightly below that—resulted in a significant change in the KT and superfluid onset temperatures. In comparison to the study by Zimmerli *et al.*—where the lowest operating temperature was no less than 600 mK—it was initially believed that the onset coverage in the MCNT study should have more readily corresponded to a film thickness below the completion of the third layer, simply based on the fact that the operating temperature was significantly lower. From the KT theory, a lower temperature should allow for the detection of a superfluid film at an overall thinner film. [37]

According to Crowell *et al.* [89]—in which the adsorption of superfluid ^{4}He was studied on Grafoil in a torsion-oscillator assembly—a coverage near the completion of the 3rd layer has $T_{\mathrm{KT}} = 600$ mK, as shown in Figure 3.12. As the coverage is increased beyond the 2nd-layer completion, at a coverage of 20.4 atoms/nm^2, the onset temperature becomes roughly 300 mK 1.3 atoms/nm^2 before the 3rd-layer completion at 28.0 atoms/nm^2. By the completion of the 3rd layer, the onset temperature is in the neighborhood of 600 mK. However, this study with the MCNT powder would be inconsistent with the study of Crowell *et al.* if it was assumed that the initial peak in Figure 3.8 corresponded to the 2nd-layer completion (instead of the 3rd-layer completion), as a KT onset temperature of 600 mK is seen almost immediately after that c_3 maximum.[10] In the Crowell study, a superfluid signal in the 3rd layer (i.e., the film above the 2nd-layer completion coverage) with a transition temperature in the neighborhood of 300 mK is seen

[10]Again, the maximum in c_3 is a tell-tale sign of the completion of a layer. Thus, a layer completion must be recognized at this particular coverage.

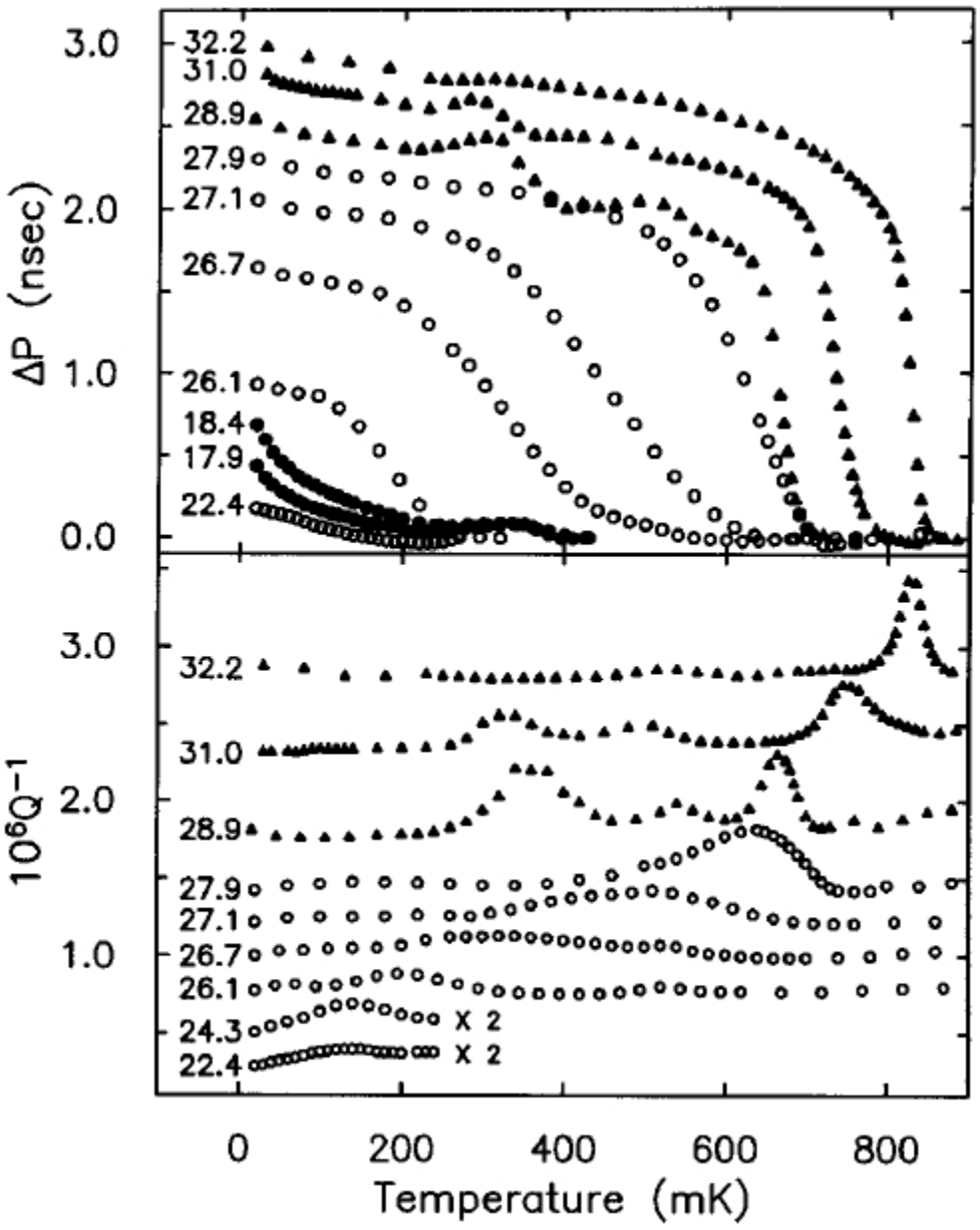

Figure 3.12: **Oscillator period shift ($\Delta\mathcal{P}$) and superfluid attenuation (Q^{-1}) as functions of the temperature, from Reference [89].** The closed circles in the $\Delta\mathcal{P}$ plot correspond to the 2nd layer, while the open circles and triangles correspond to the third and fourth layers, respectively. The ^{4}He coverage is indicated to the left of each trace. An abrupt shift in T_{KT} occurs over a small change in coverage, from 200 mK at 26.1 atoms/nm^2 to 600 mK at 27.9 atoms/nm^2, which is right before the 3rd-layer completion at 28.0 atoms/nm^2.

with a significant coverage above the completion point: almost 6.3 atoms/nm^2 = 0.063 atoms/Å^2 above the 2nd-layer completion. Thus, interpreting the first c_3 maximum in Figure 3.8 as the 2nd-layer completion would be difficult. Although it is true that the studies are not exactly the same based on the vastly different geometries involved, there should still be some general consistency between the studies, suggesting that the chosen scale for this MCNT study is reasonable even in the wake of having such high KT onset temperatures while operating significantly below the operating temperature of Zimmerli *et al.*

Another possibility regarding the absence of superfluidity in the third layer may be due to an absence of a connected path for macroscopic detection of the signal until a significant coverage is reached. In the study of Whitlock *et al.*, a 2D helium film was studied under the absence of a substrate for the purposes of establishing exactly at what value of coverage the film turned into a self-bound liquid. [106] In other words, it was shown that it takes the helium film a specific coverage in order for the film to actually be connected. Prior to reaching that critical coverage, the film is in a phase of (2D) gas-liquid coexistence consisting of unconnected liquid droplets. Above the critical coverage, which was determined to be 4 atoms/nm^2, the system would then condense into a connected liquid while possibly still in a coexistence regime with a 2D gas. Another study, by Clements *et al.*, looked at a more realistic helium film undergoing multilayer growth on top of two solid layers of ^{4}He on graphite. [107] In this study, it was determined that the 1st fluid layer (i.e., the 3rd overall ^{4}He layer) would condense into a self-bound liquid at a coverage of 3.5 atoms/nm^2. Moreover, the subsequent fluid layers were also found to undergo a transition into a self-bound liquid once each layer reached the same critical coverage. Although these studies exclusively focused on the adsorption of helium on flat geometries, their conclusions regarding liquid nucleation at a critical coverage should equally well apply to a cylindrical geometry, particularly since the existence of liquid globules—which do not form

an interconnected film—at low coverage should not be affected by surface-tension effects. In other words, the cylinder should look relatively flat for each of the liquid droplets, and the effects of surface tension could perhaps drive the critical coverage to a higher value since it now costs the globules extra energy to form a self-bound film on the inherently curved surface.

Coupling these notions with the MCNT powder geometry at the macroscopic scale—which showcases grain boundaries on length scales of approximately 10 μm as in Figures 2.4a and 2.4b—it is possible that a significant coverage must be obtained until a proper connected path is achieved across the macroscopic cell. Put another way, even though a superfluid film may exist on many of the grains across the sample, the linking between the films on adjacent grains may be weak enough to suppress the propagation of third-sound with significant attenuation. Perhaps this is the reason why there is no clear-cut reduction in the Q in Figure 3.10 at the presumed onset region. Adding to this, it may also be the reason why there is a very clear attenuation observed in Figure 3.5 for the experiments at 1300 mK, since this operating temperature requires a significantly thicker film for a superfluid layer to form. So, with an already macroscopically connected superfluid film established at these temperatures, the KT onset at the critical thickness is more readily observed with the reduction in the Q due to the vortex-antivortex screening of the superfluid current. As mentioned before, the data at 250 mK does not readily show such a reduction in the Q at the onset coverage in Figure 3.8, so that it is likely that the signal in this region already had a value of T_{KT} much higher than 250 mK, and it was just difficult to capture a signal with a lack of macroscopic connection across the powder.

Figures 3.13 to 3.20 show c_3 and Q as functions of the temperature for 0.308, 0.318, 0.331, 0.350, 0.355, 0.361, 0.364, and 0.381 atoms/Å^2, respectively. As in Figure 3.12—where T_{KT} is taken to coincide with the maximum in the attenuation,

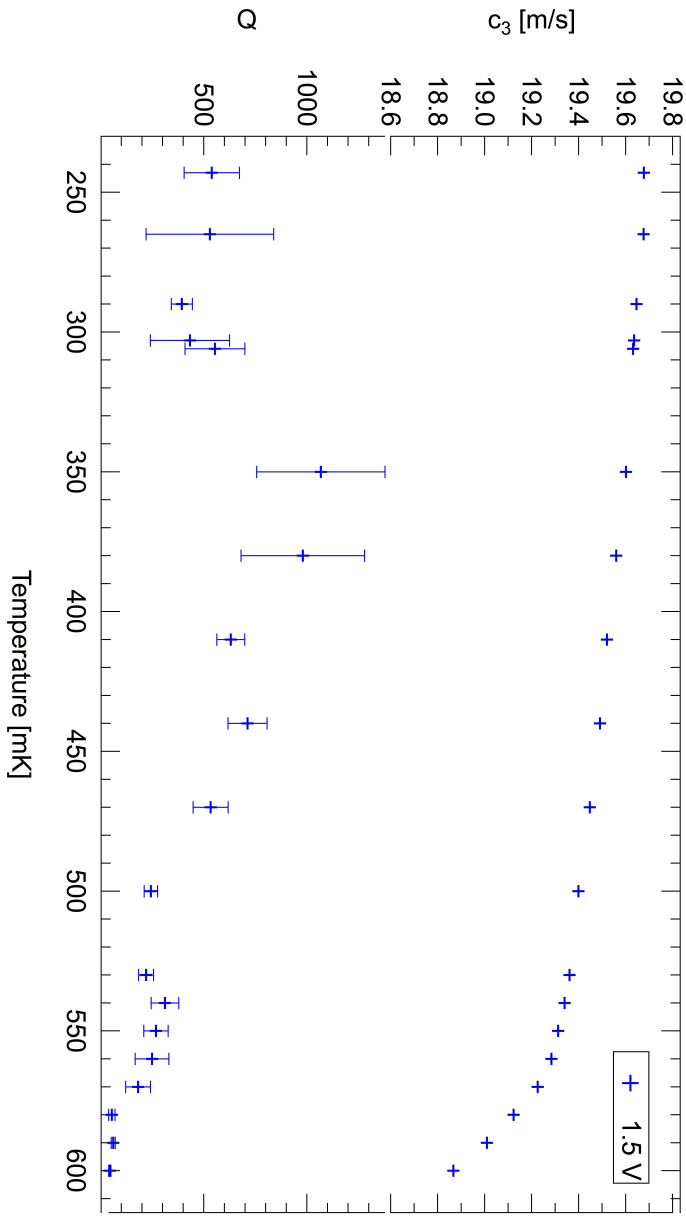

Figure 3.13: **Temperature sweep at a coverage of 0.308 atoms/Å^2.** The drop in the Q occurs at around 560 mK, which is taken as T_{KT} for this particular coverage.

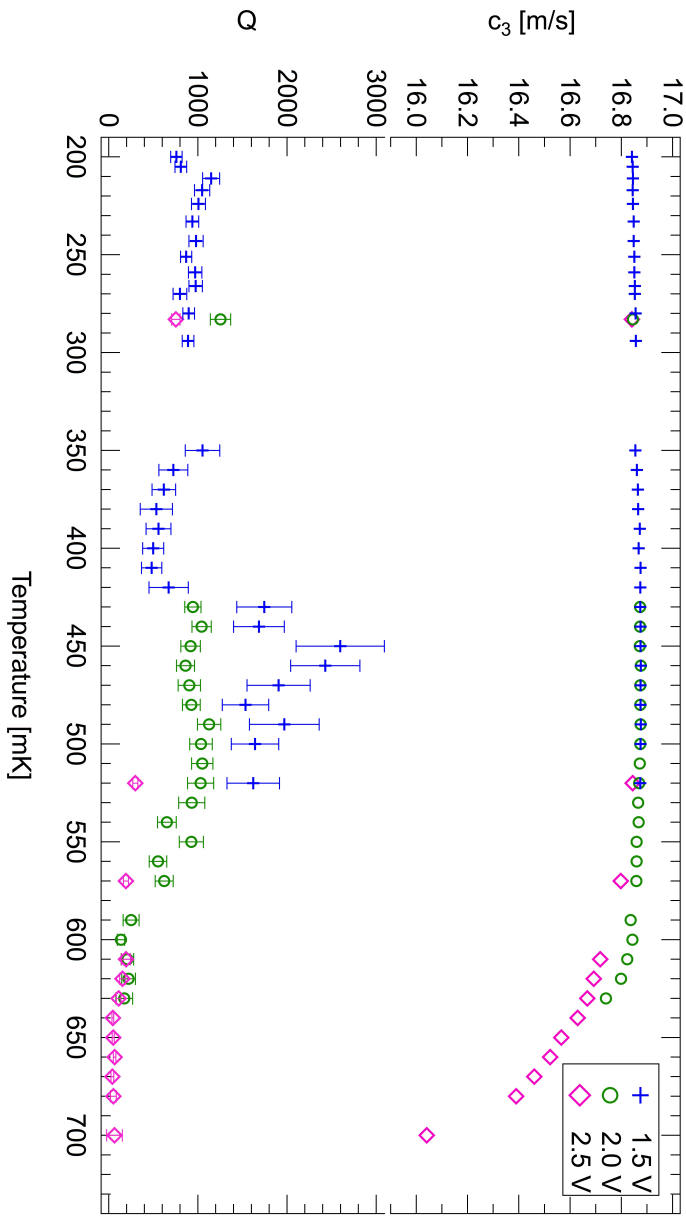

Figure 3.14: **Temperature sweep at a coverage of 0.318 atoms/Å².** The drop in the Q occurs at around 635 mK, which is taken as T_{KT} for this particular coverage. Notice that c_3 also slightly increases as a function of the temperature before reaching the KT onset temperature.

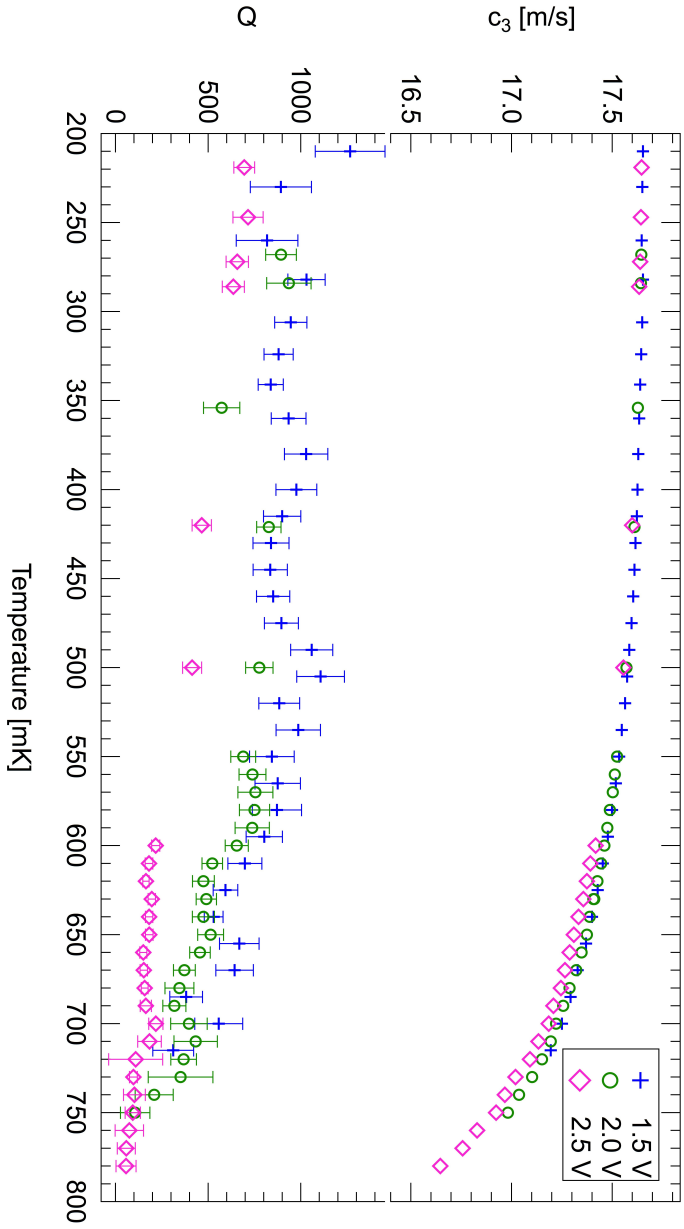

Figure 3.15: **Temperature sweep at a coverage of 0.332 atoms/Å^2.** The drop in the Q occurs at around 720 mK, which is taken as T_{KT} for this particular coverage.

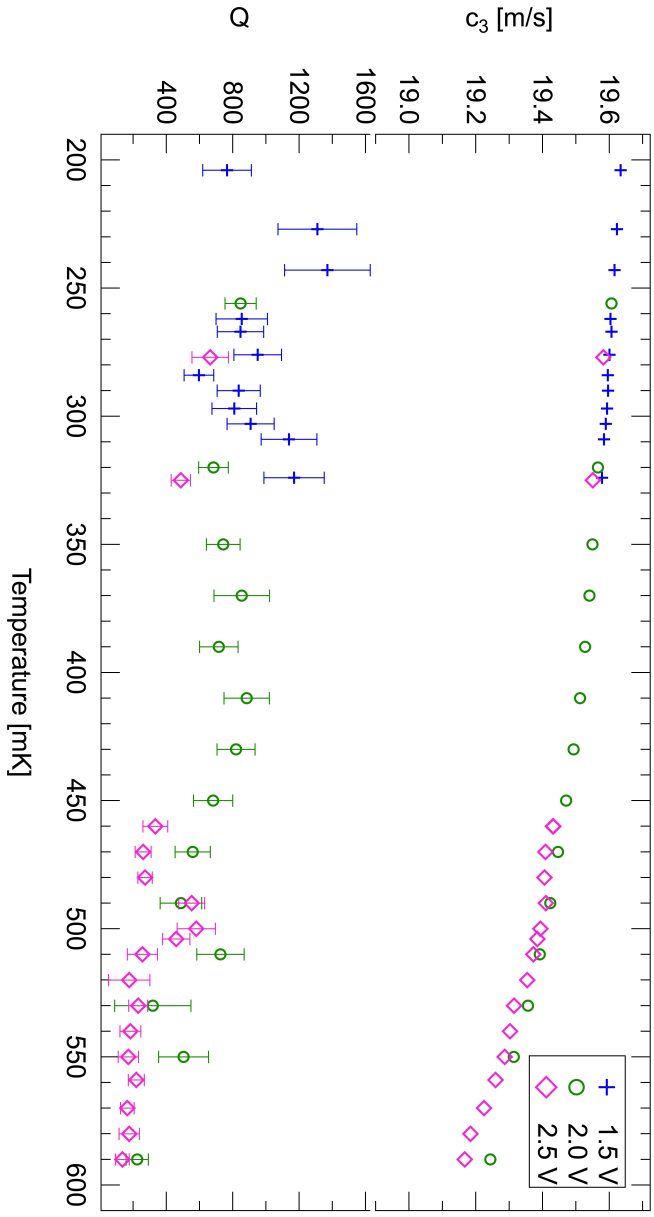

Figure 3.16: **Temperature sweep at a coverage of 0.350 atoms/Å^2.** There is a drop in the Q around 520 mK, taken as T_{KT} for this coverage. However, this drop is not substantial, as the Q remains quite high compared to the points prior to the rise at 490 mK. No signal was seen at any temperature above 590 mK, which could equally well serve as T_{KT}. For these reasons, a 70-mK uncertainty is quoted for T_{KT} at this coverage.

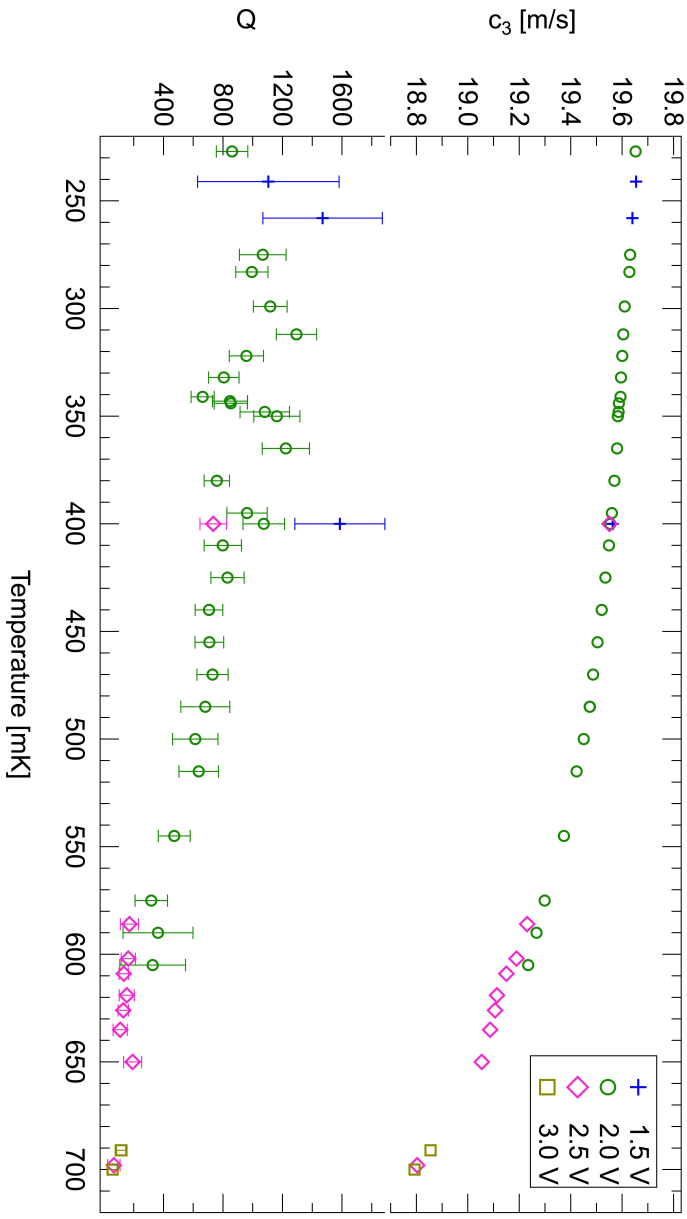

Figure 3.17: **Temperature sweep at a coverage of 0.355 atoms/Å².** There is no apparent drop in the Q to suggest the appropriate KT onset temperature. At 635 mK the Q is 110, while at 700 mK it is about 60. The KT onset temperature could perhaps be in between these values, or even above 700 mK since the signal could no longer be detected beyond this value. A value of 670 mK is taken as T_{KT}, with a 50-mK uncertainty.

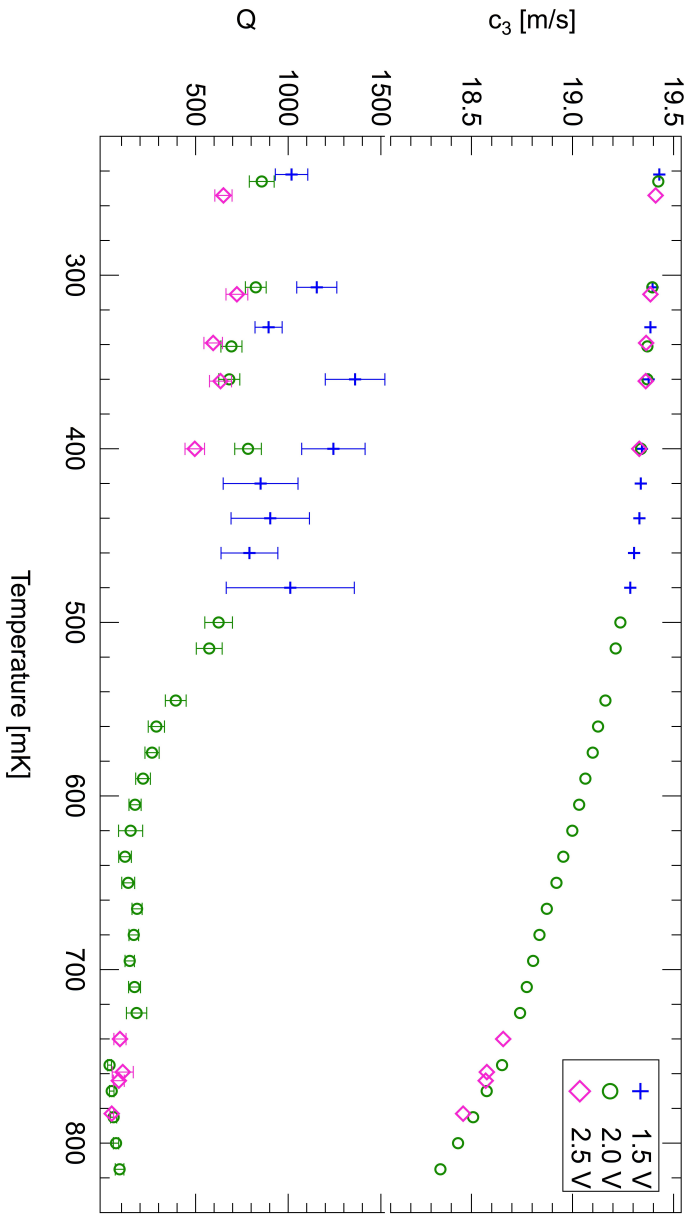

Figure 3.18: **Temperature sweep at a coverage of 0.361 atoms/Å².** There is a drop in the Q to a value below 100 around 750 mK, particularly in the 2.0-V drive data. There is a rise in the Q for this drive from this point to the last data point, but the largest value in this rise in the Q remains below 100. The KT onset is taken to occur at 750 mK with an uncertainty of 60 mK to account for these issues.

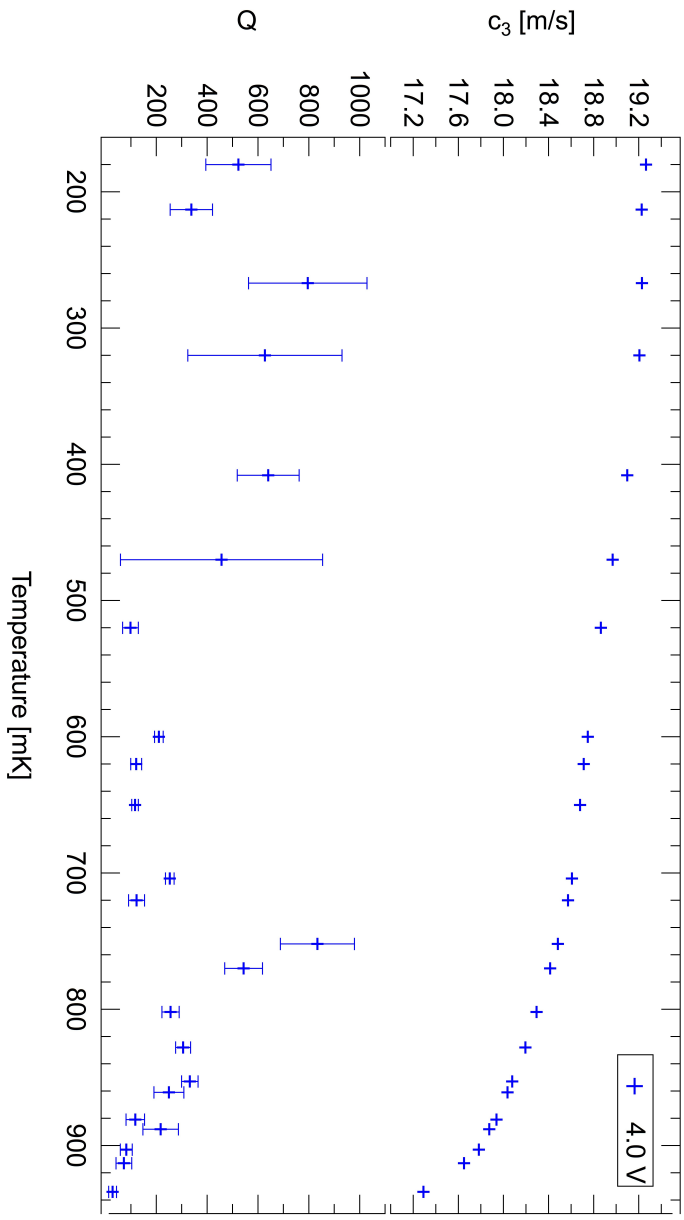

Figure 3.19: **Temperature sweep at a coverage of 0.364 atoms/Å².** A drop in the Q occurs at around 920 mK, which is taken as T_{KT} for this particular coverage. There are regions where the Q is low—such as at 520 mK—but the onset must occur at much higher temperatures for consistency with the KT theory.

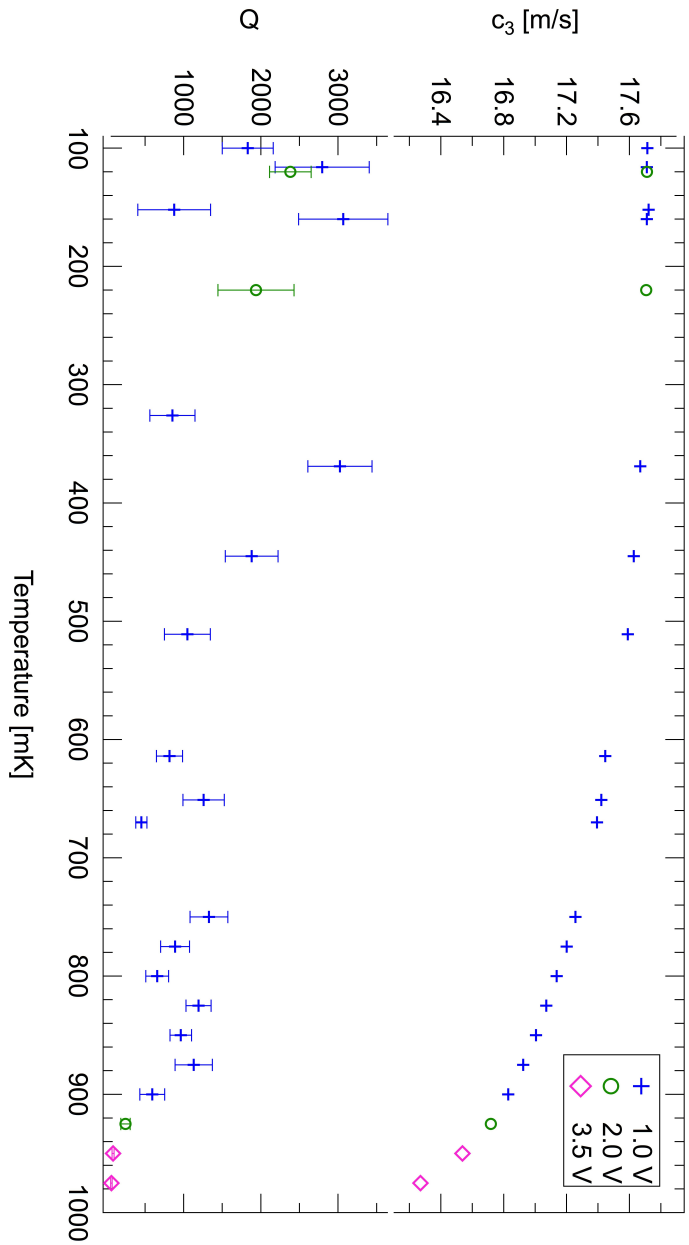

Figure 3.20: **Temperature sweep at a coverage of 0.381 atoms/Å².** Although the data points near the onset temperature are represented by different drive levels (which may have different levels of attenuation), a drop in the Q seems to occur near 950 mK, which is taken as T_{KT} for this coverage. An uncertainty of 70 mK is taken to make up for this lack of data points, owing to the difficulty of controlling the dilution refrigerator above 900 mK.

Q^{-1}—a similar analysis is done in this study when the Q sharply decreases.[11] For the temperature sweeps at 0.308, 0318, and 0.332 atoms/Å^2, the general trend is that the KT onset temperature increases as the coverage increases, which is consistent with the KT theory [40], even under the circumstances of finite-size [43] and finite-frequency broadening [38, 43].

However, one notable signature that is not seen in any of the other temperature sweeps is the slight increase in the sound speed as the temperature is increased at 0.318 atoms/Å^2, as shown in Figure 3.14. This is rather peculiar, as the sound speed—and thus the superfluid fraction—should gradually decrease as the temperature is increased towards T_{KT}, after which would come the gradual drop in the speed in the finite-size-broadened reduction of the superfluid fraction. Such an initial increase in the sound speed as a function of temperature seems to suggest a film thinning of the superfluid fraction, or perhaps a stiffening of the film, before the indicative KT drop.

It is not entirely clear exactly why this happens, particularly since a similar effect has not been seen in other studies, including the low-temperature, torsion oscillator studies on Grafoil [89]. Perhaps the coverage at which this sweep was done saw a restructuring in the film, which has been seen in other studies as a function of coverage [108, 109], and could possibly be seen as a function of temperature under specific conditions. In particular, it has been reported [109] that the second layer of ^{4}He adsorbing onto graphite undergoes a restructuring at the completion of the third layer. So, the core layers are affected by the adsorbate and are not static by any means in their structure. In particular, the restructuring is of the form that the second-layer solid is actually further compressed towards the substrate upon the 3rd-layer completion. In this sense, the increase in the density

[11] In some cases, as can be seen in some of the mentioned figures, the Q does not sharply decrease where signal was actually seen. Under those circumstances, a larger error bar in the KT onset temperature is employed to account for a range that also includes the point at which no signal was seen.

in the 2nd layer will prevent the 4th layer from filling until the restructuring is complete. Moreover, when the new layer begins to fill, there is a lack of percolation of the helium film in this new layer due to the need to reach a critical density for a self-bound liquid to form [107]. Because of the gas-liquid coexistence of the new layer, the helium atoms that are added to the cell are also going into the gaseous phase. A combination of this restructuring of the core film and this non-percolating topmost film layer is believed to result in a constancy in the value of T_{KT} in the 4th adsorbed layer as reported by Crowell *et al.* [89] This constancy can be seen in the attenuation, Q^{-1}, profile in Figure 3.21.

This restructuring of the film may be the cause behind probably the most anomalous feature observed in the temperature sweeps on the MCNT powder. Notice that the KT onset temperature is around 720 mK at 0.332 atoms/Å^2, but that there is altogether no superfluid signal detected beyond 590 mK and 700 mK at coverages of 0.350 and 0.355 atoms/Å^2, respectively. A temperature at which a signal is no longer detectable would ideally indicate the superfluid transition temperature T_{c}. However, the detection of third sound relies on the presence of a strong signal, and it is not as sensitive to the superfluid transition temperature as compared to torsion-oscillator measurements, as these Andronikashvili-type experiments can extend to capturing the superfluid fraction down to effectively zero, as can be seen in Figures 1.11 and 3.12.[12] Predominantly because of finite-size effects, the KT onset temperature, T_{KT}, will occur at a lower value of temperature than the superfluid onset temperature, T_{c}. So, if the signal in the MCNT powder at coverages of 0.350 and 0.355 atoms/Å^2 is lost at the temperatures of 590 mK and 700 mK, respectively, then these values of temperature should be an upper bound for T_{KT}. However, there is no clear-cut reduction in the Q at these coverages to suggest a finite-size broadened KT transition when a third-sound signal

[12]The sensitivity of the torsion-oscillator assembly owes to the great precision with which the period shift can be detected due to the superfluid decoupling from the oscillator's moment of inertia (provided the oscillation angular velocity does not exceed a critical velocity for superfluid atoms to get excited into higher-energy states).

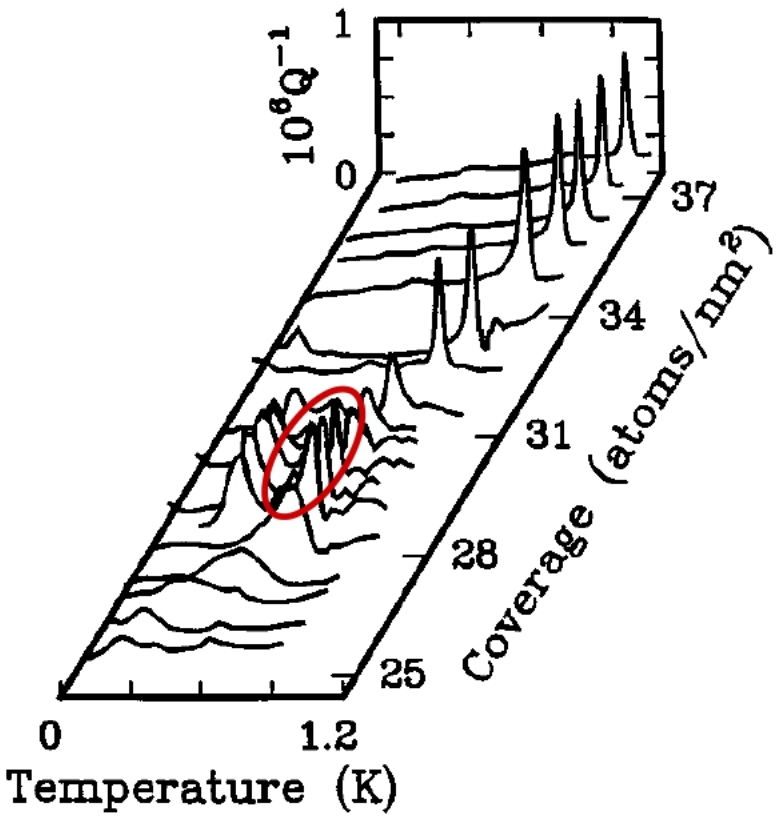

Figure 3.21: **Attenuation, Q^{-1}, as a function of temperature and coverage from Reference [89].** The peaks represent points of large attenuation. Note the encircled region between 28 - 30 atoms/nm^2 in coverage, where the peak—attributed to the KT transition—remains constant. The peaks at slightly lower temperatures next to the encircled region are an anomaly that could be attributed to a 3rd-sound resonance, although it was interpreted by Crowell *et al.* as a phase transition on some other surface in the cell (not the Grafoil) that happened to be detected at certain coverages.

is observed. Thus, it is difficult to use the observed data to robustly infer a reasonable KT onset temperature. Whatever the case may be, the value of the KT onset temperature at these coverages (even upon taking these upper bounds in temperature for each coverage) is less than the value obtained from the sweep at the coverage before it. This peculiarity thus presents a dip—instead of a plateau as in the work of Crowell *et al.* in Reference [89]—in the behavior of T_{KT} as a function of the ^{4}He coverage, as shown in Figure 3.23. Even when considering finite-size and finite-frequency effects in the KT transition, the universal KTN line will still determine the transition temperature, since these effects aim to broaden the transition to a superfluid fraction of zero without necessarily changing the essential physics of the transition.[13] The temperature sweep at 0.361 atoms/Å^2 continues the dip away from the linear relationship until it is again restored at 0.364 atoms/Å^2.

It is not clear why a dip in T_{KT}—seen at coverages ranging from roughly 0.345 - 0.365 atoms/Å^2—should occur in the MCNT powder as opposed to a plateau. This coverage range is in the neighborhood of the 4th-layer completion in the c_3 profile in Figure 3.8, so that it seems that a restructuring of the core film may be taking place closer to the 4th-layer completion instead of the 3rd-layer. Moreover, issues of the new film not being self-bound should occur at low coverages in the ^{4}He atoms adsorbing onto the new layer, but the dip in the KT profile is seen while a layer completes and a new one begins to form. Perhaps this latter inconsistency can be somewhat resolved by noting that there is not a single type of tube present in the MCNT powder. Indeed, there could certainly be some smearing in the adsorption of a new layer, as the tubes with a larger outer diameter would have their own 4th layer completed before the smaller-diameter ones.[14] The fact that

[13] The underlying physics is still unchanged, in the sense that the phase transition is controlled by the thermal excitation of vortex-antivortex pairs.

[14] Such a trend is established because a smaller radius of curvature would invariably result in a larger cost in surface energy, so that the smaller-diameter tubes should have a smaller film thickness than the ones with the larger diameter.

this smearing does not wash out the c_3 profile is a testament to the fact that the distribution of sizes is not considerably vast, but instead concentrated enough to make it reasonable to analyze the trends with a single diameter in mind. It is also important to note that these coverages at which there is a dip in T_{KT} do not correspond directly to the minima in Q seen in Figure 3.10.

Although the linear trend in T_{KT} versus the coverage is restored at 0.364 atoms/Å^2, the temperature at which onset is taking place—namely at or above 800 mK—is obscured by attenuation mechanisms other than just the topological excitations. Indeed, according to the Atkins-Bergman theory of third-sound attenuation, at temperatures above 800 mK, the ^{4}He vapor pressure becomes significant enough to provide an extra mechanism of attenuation, which is predominantly due to desorption effects. [49, 61, 62, 110] Thus, it is a bit more difficult to pin down the KT onset in looking at the attenuation profile alone, since desorption effects are also prevalent. The data point at the highest coverage shown in Figure 3.23 is from the data taken at 1300 mK, where the onset coverage at which a superfluid signal was detected was 0.413 atoms/Å^2.

Figure 3.23 also presents one other effect that has been seen regarding reentrant superfluidity. In Reference [89], the second layer exhibited a novel phenomenon in which a period-shift was observed over some coverage, but then disappeared on account of reaching a different phase of the adsorbed helium film in this layer, as shown in Figure 3.24. At temperatures around or above 20 mK—which was the baseline temperature in the study—the superfluid signal disappears once crossing over into the C+F (Commensurate + Fluid) phase on account of the formation of a quasi-solid in the film. In other words, it is believed that because the atoms in the liquid film become locked-on to the graphitic lattice structure, the mobility of the superfluid atoms becomes vanishingly small. As a result, there is no mass decoupling, which is why there is no period shift in the oscillator.

In the study on the MCNT powder, a similar effect occurs, which can be seen

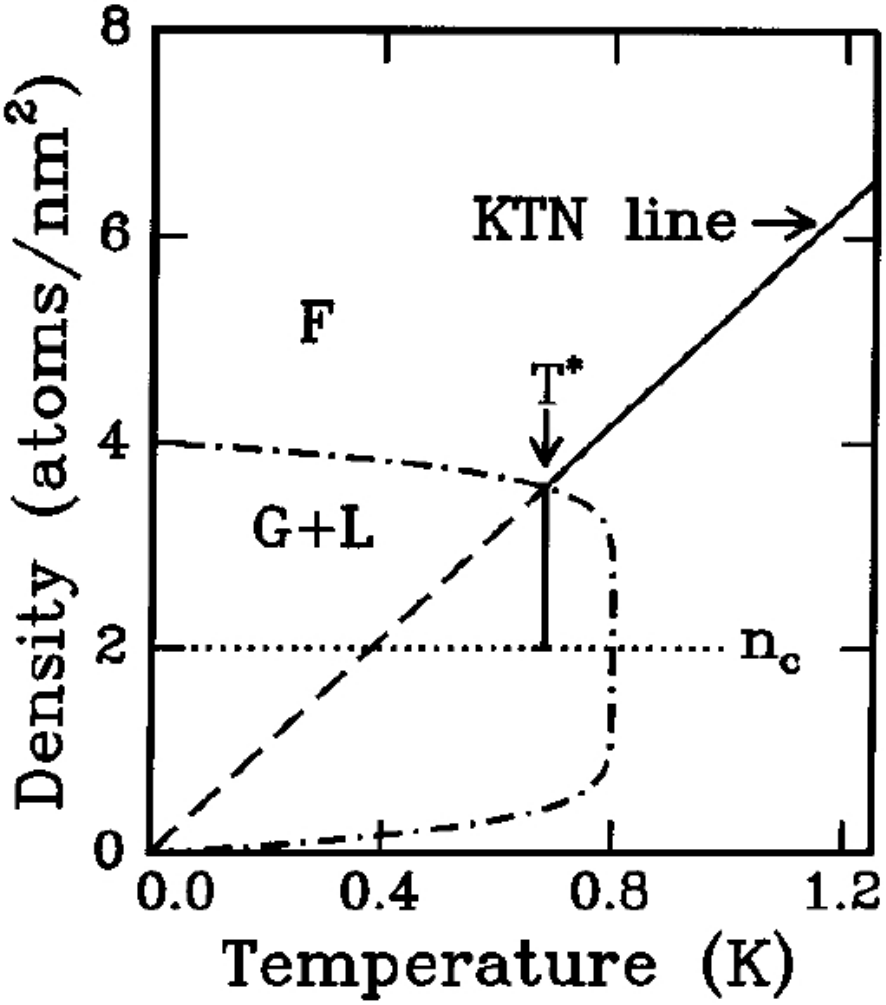

Figure 3.22: **Schematic representation of the KTN line for a newly formed ^{4}He layer on Grafoil from Reference [89].** The validity of the KTN line is not completely clear in the gas-liquid coexistence (G+L) region, particularly when the coverage in this new layer is below the critical density, n_c, where a self-bound liquid has not yet formed.

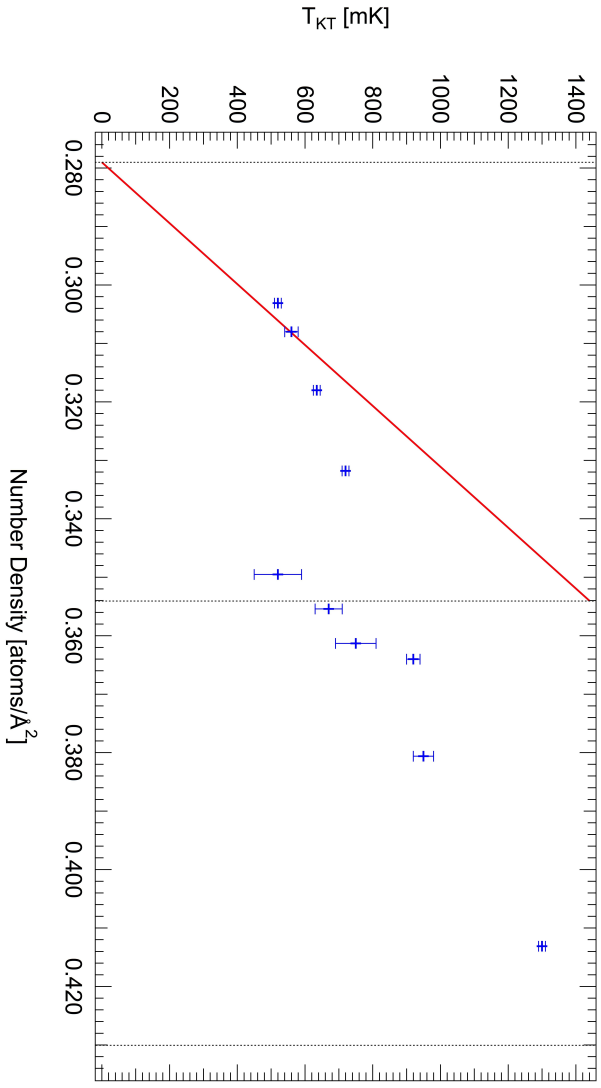

Figure 3.23: T_{KT} **as a function of the** ^{4}**He coverage on the MCNT powder.** The vertical lines indicate layer-completion coverages, starting from the 3rd-layer completion. The data points are taken from the temperature sweeps in Figures 3.11 and 3.13 to 3.20, with the last data point obtained from the onset coverage at 1300 mK in Figure 3.6. The solid line is the (theoretical) KTN line obtained using Equation 1.32. There is a dip in T_{KT} in the experimental data around the 4th-layer completion. A possible explanation for the mismatch in the slopes of the data and the theory is that a good fraction of the ^{4}He atoms remain gaseous and perhaps do not condense into a liquid to participate in superfluidity.

if one is sweeping the third-sound profile as a function of coverage at, for example, a temperature of 600 mK. According to Figure 3.23, a superfluid signal will not be seen until approaching 0.320 atoms/Å^2, since the onset temperature is below this value at lower coverages. Upon increasing the coverage from this point forward, a superfluid signal would be seen until approaching the neighborhood of 0.340 - 0.350 atoms/Å^2. Eventually, the superfluid signal will again be detectable upon reaching a coverage around 0.360 atoms/Å^2 or so. In this sense, there are two superfluid onsets instead of one, to which the second onset is referred as a case of re-entrant superfluidity. Such has not been seen to occur on other substrates, so that the effect seems to not only require long-ranged crystalline order in the underlying substrate, but also a strong coupling between the adsorbate and the substrate.

Albeit, it can be argued that the re-entrant behavior seen in the work of Crowell *et al.* may not be of the superfluid type. If it is, in fact, true that the first two layers of ^{4}He on graphite are solid [81], the period-shifts seen in these torsion-oscillator measurements could be on account of properties of the helium solid. Initially, it was believed that there was a supersolid phase in helium from the experiments of Kim and Chan [111], which saw a period shift in solid helium at a temperature below 100 mK. However, the shear modulus was also seen to exhibit the same strange behavior at identical transition temperatures. [112–114] Theories employing the importance of dislocations to help explain the novel effects seen in the shear modulus (e.g., Reference [115]) helped discredit the idea of the supersolid. Nonetheless, it is possible that the period-shift seen in Reference [89] in the 2nd layer might have been due to these effects within the solid helium, so that seeing the signal beyond the C+F phase in Figure 3.24 should really be taken as the only onset in superfluidity. The work of Crowell *et al.* was sensitive to an anomaly in the KT onset temperature that strayed away from the KTN line, as mentioned before. However, since it was a plateau in the onset temperature—as

opposed to a dip in the MCNT study—then the superfluid signal would not have disappeared when investigating the period-shift as a function of the coverage at a particular temperature.

A final note regarding Figure 3.23 is the disagreement between the slope of the KTN line in comparison to the experimental data. It is not completely clear if the KTN line should necessarily apply to the superfluid film in each layer, as shown in the schematic in Figure 3.22. For the MCNT powder, the KTN line shown in Figure 3.23 is determined by making a few assumptions. Since the coverage at which a third-sound signal is first seen is slightly above the 3rd-layer completion, the dead layer, D_{dead}, is taken to be three layers—which includes the initial two solid layers and roughly a full layer of inert liquid film. Thus, $T_{\mathrm{KT}} = 0$ at 3 layers = 0.279 atoms/Å^2. Another point must be determined in order to draw the theoretical line. To calculate T_{KT} at the 4th-layer completion, the universal-jump criterion in Equation 1.32 is utilized.

Since each layer after the 2nd-layer completion completes at a density of 0.076 atoms/Å^2, then the areal superfluid density is $\sigma_{\mathrm{s}} = 5.05 \times 10^{-25}$ g/cm^2. Using Equation 1.32 and solving for T_{KT}, the KT onset temperature should be 1440 mK. Therefore, $T_{\mathrm{KT}} = 1440$ mK at 4 layers = 0.354 atoms/Å^2. Of course, aside from the anomalous dip in T_{KT} seen in the data, the mismatch in the slopes between the experimental data and the theory suggests that there is less superfluid in the system than is predicted. Changing the coverage scale will still not change the slope of the experimental data in relation to the KTN line. Perhaps this is further evidence to suggest the presence of the gas-liquid coexistence on these substrates, where, for instance, the addition of more ^{4}He atoms above the 3rd layer completion has a large fraction going into the gas phase instead of into the liquid regions. So, in calculating the onset temperature at the 4th-layer completion for drawing the KTN line in Figure 3.23, it was assumed that all of the helium atoms became superfluid. Relaxing this assumption may allow for better

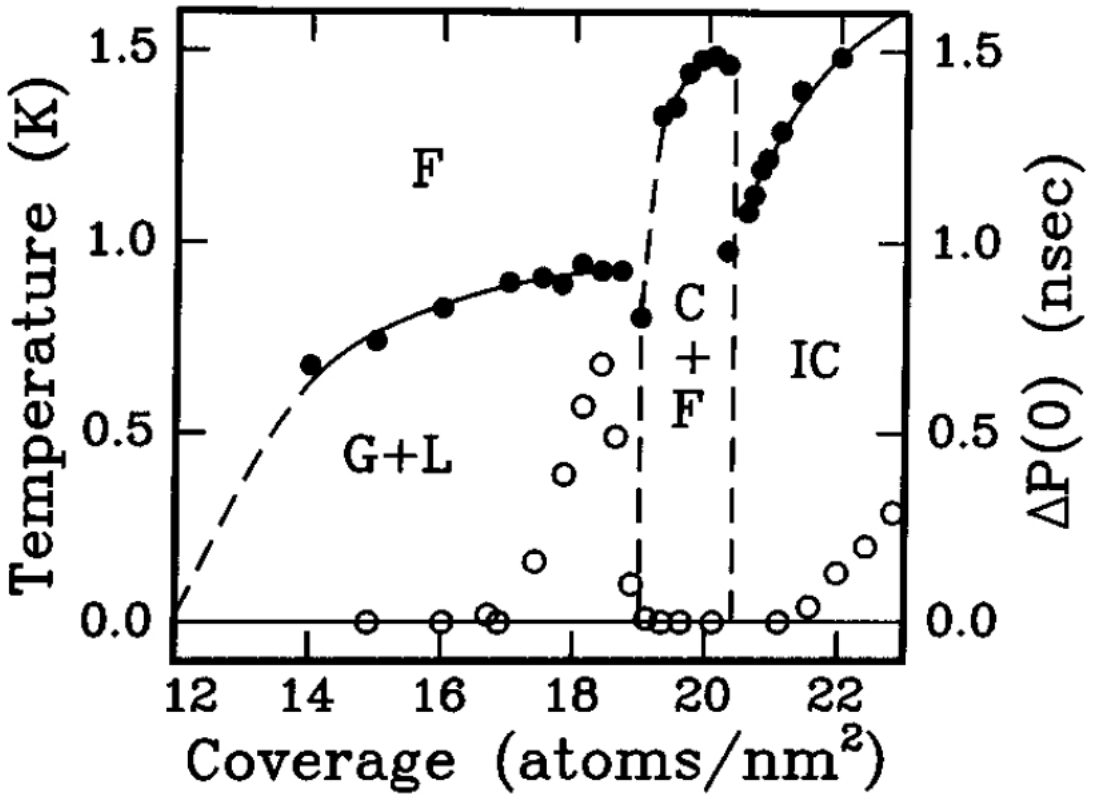

Figure 3.24: **Superfluid fraction as a function of ^{4}He coverage overlaid on the 2nd-layer phase diagram, from Reference [89].** The open circles represent the period-shift in the torsion oscillator—which is sensitive to the superfluid fraction—while the closed circles represent data taken from Reference [116]. The C+F (Commensurate + Fluid) phase represents a region of coverages at which there is a fluid film present, but that it is locked-on to the underlying substrate's lattice structure. The locking-on of the fluid film is thought to immobilize the superfluid, resulting in the loss of superfluidity in this phase. The superfluid fraction becomes nonzero again beyond the C+F phase, thus coining the phenomenon as a re-entrance of superfluidity.

agreement with the experimental data. Nonetheless, it is not completely clear why there should be a depression in the KT profile in Figure 3.23, as such effects would seemingly suggest a constancy in the KT temperature.

3.5 KT Transition on a Cylindrical Geometry

Before discussing the theoretical implications that the cylindrical geometry imposes on the helium film adsorbed on the exterior of the MCNT powder, it is important to discuss some further evidence regarding this study's insensitivity to adsorption on the interior of the nanotubes. Recall that one of the reasons for which it is believed that there is no significant adsorption on the inside diameter of the tubes is purely an inconsistency in the adopted coverage scale, as described in Section 3.2. However, even though the calibration of the coverage scale led to an unusually large estimate for the average inner diameter of the tubes in the powder, it would have been expected that two superfluid transitions would have been detected had there been a macroscopic adsorption within the tubes: one for the interior and one for the exterior.

The superfluid onset would first have taken place on the interior, since the film would preferentially adsorb onto the concave interior as opposed to the convex exterior [104], as in the discussion regarding capillary condensation in Section 3.3.[15] In this sense, the superfluid transition within the interior would have been the first onset observed in the acoustical investigation using third sound. As in the theoretical study of the adsorption of helium within cylindrical pores, by Saam and Cole, there eventually would have been an instability in the adsorbed film on the interior as the coverage was increased. [117] This instability is discussed in terms of surface modes within the film. The quasiparticle of these surface modes

[15] Of course, this is assuming that the interior is large enough that a helium atom can overcome its zero-point energy to be caged. As discussed in Section 3.2, this would not be a problem as the inner diameter—albeit assumed to be very large in this study due to the adopted coverage scale—should definitely be much larger than 18 Å [70].

is the ripplon, which is a quantized capillary-tension wave on the surface. At a specific coverage on the interior, the instability will result in the complete filling of the cylindrical pore, so that there is no longer a film. Upon following the third-sound wave on the interior film, this instability should result in a complete loss of the third-sound signal, as the relevant sound wave upon pore filling will be fourth sound. Although there will be some smearing of the signal from the distribution of diameters within a system like the MCNT powder of this study, eventually the third-sound signal should completely disappear. Afterwards, the film should begin adsorbing on the exterior, which will then result in a secondary onset of superfluidity. However, only a single onset was observed even though the sound signal was tracked very carefully at many coverages, particularly in the data taken at 1300 mK where an additional effort was made to obtain the adsorption isotherm of the helium film. A conscious effort was also made to search for the fourth-sound signal at higher frequencies in the FFT profile—since $c_4 > c_3$—but no such resonances were observed.

It is possible that even if a good number of the tubes were open, that an interconnected film may not have been present to detect the flow across the MCNT powder. Indeed, it is not even clear if the gaps between the micron-sized grains in the powder—as in Figure 2.4—would even allow for the connection of the film between the interiors without the presence of a film on the exteriors. Moreover, it is possible that a vast majority of the tubes are capped in the first place, so that even if some proportion of the tubes are open on one or both ends, there still might not even be a macroscopic connection of the film internally through the tubes for the detection of a signal. It is possible to open the interior of carbon nanotubes by breaking the tubes to, at least, open one cap. One method of doing this is via sonication [118], but the tubes used in this study were not sonicated upon receipt from the manufacturer. Thus, it is inconclusive whether or not there is adsorption of helium on the interior of the tubes. As a result,

this study assumes that no adsorption takes place within the tubes both on the premise of the consistency of the adopted coverage scale with other studies on graphitic substrates—as discussed in Section 3.2—but also because of the absence of a dual onset in the superfluid signal.

However, there is most certainly helium adsorbing to the exterior of the tubes, and a theoretical model has been devised, by Machta and Guyer, to describe the modified KT transition that takes place on the constraining cylindrical geometry. One of the main conclusions of this study, taken directly from Reference [119], is that there is no vortex unbinding transition[16], so that there is a continuous, instead of abrupt, decrease of the superfluid fraction to zero. On the flat, 2D geometry, the energy required to separate two vortices grows logarithmically in the separation between the vortex-antivortex pairs. In this sense, there is enough thermal energy present within the film to separate the pairs to effectively infinite separation. In the case of the cylindrical geometry, the energy to separate the pairs, instead, grows linearly in the axial separation, so that there is not enough thermal energy available at the relevant temperatures to separate the vortices to infinite separation. It must be noted that separation can occur in both axial and azimuthal directions. Of course, the vortices cannot separate much azimuthally because of the constraining geometry; however, even on the longer length scale—namely, the axial direction—a vortex-unbinding transition is still forbidden due to the energy profile in the separation of vortices. Thus, the KT transition is considerably broadened with no abrupt drop in the superfluid fraction.

Another important conclusion is that even though the vortex pairs do not unbind, there is a zero-frequency dissipation mechanism that is set up by the counter-rotation of a pair of vortices azimuthally to reduce the superfluid current. On the flat, 2D geometry, finite frequency effects do create a rounded KT transi-

[16]This is true for a single cylinder, but a jungle gym of such cylinders may allow for a vortex unbinding transition, as in the discussion regarding vortex strings in Section 1.6.

tion [38]. In the absence of an alternating superfluid current, the KT transition on such a flat geometry introduces an abrupt drop in the superfluid fraction at the KT onset temperature. However, even though there is a rounded transition on the cylindrical geometry, there is a considerable amount of dissipation sufficiently below T_{KT}—where finite-size effects can be neglected—which aims to reduce the superfluid fraction.

Indeed, because of the difference in the energy involved in separating bound pairs azimuthally and axially, the superfluid density is actually different along each of these directions. In this sense, the superfluid density must be treated as a tensor. However, although the superfluid density must be treated as a tensor, as Machta and Guyer explain, experiments that deal with cylindrical geometries with a large aspect ratio will only be sensitive to the axial superfluid density.

3.6 Future Work

A significant amount of future work can be conducted regarding this system of MCNT powders. It would be worthwhile to provide fits of this experimental data according to the theory of the KT transition on the cylindrical geometry provided by Reference [119]. However, to do this requires a much more detailed survey of the surface area available for adsorption of the helium film. A correspondence between the helium adsorption isotherm of Figure 3.3 and a nitrogen (N_2) BET adsorption isotherm [120] would help characterize the adsorption profile a bit more conclusively. Moreover, the installation of an *in situ* pressure gauge would further help characterize the adsorption properties of the helium film by looking for the layer-completion steps as seen by Zimmerli *et al.*, which is shown in Figure 3.4.

To obtain potential agreement with the predictions set forth by the KT theory on the cylinder, it would also be paramount to have better control over the distribution of diameters in the MCNT powder. A scalable, cost-effective technique

of producing MCNTs of a very specific diameter would be very helpful, as the system would then be more readily understood in its adsorption behavior. It is also very important to characterize whether or not the tubes are open. Such an ambiguity makes the adsorption profile very difficult to establish. If the tubes are known to be open to a large degree, then it would be easier to pursue a diligent search of a signal at the lowest coverages.

If a cost-effective technique of harvesting a macroscopic number of nanotubes at a very small range of diameters was possible, the adsorption properties could be mapped out as a function of diameter. This would be particularly beneficial for verifying the specific trend that the helium film follows to better establish a more complete experimental backbone to compare with the theory of superfluid helium on the cylindrical geometry. Although it would be ideal to look at very small diameters by resorting to a powder of SCNTs, this was seen to be difficult because of the tendency for a collection of such tubes to form ropes, causing the effective diameter to be larger and for the presence of an extra corrugation in the geometry. [121]

The ultimate investigation into adsorption on such a geometry is to truly build up to a one-dimensional regime. Due to the unfortunate engineering issues in this study regarding the cooling power of the dilution refrigerator, a thin-enough superfluid film was not encountered to try to drive up the vortex core size to become comparable to the MCNT diameter. A way to get around this, without resolving the cooling issue, is to add ^{3}He on top of the ^{4}He film, because this may drive up the vortex-core size on account of the normal ^{3}He atoms getting sucked into the vortex cores and expanding them on account of the Pauli Exclusion Principle. [73] This was seen to increase the core size to about 100 Å around 250 mK on Al_2O_3 powders. Searching for such a one-dimensional crossover is very meaningful in the further extrapolation of phase transitions and how dimensionality plays a role in its physics.

Studies of the multilayer film growth, particularly of the superfluid, on carbon nanotubes would also help in establishing a better idea regarding the adsorption properties of helium on such cylindrical substrates. Some simulations have looked at adsorption on graphene [122] and buckyballs [123], while others have looked strictly at cylindrical geometries such as nanotube bundles [124], inside a single nanotube [125], and on a single nanotube [126, 127], but they have not been tremendously focused on investigating superfluidity. The focus has mostly been on the first couple of layers, which may not necessarily display superfluid behavior. Although the studies have established interesting phases, ranging from incommensurate to commensurate solids and sometimes to liquids if the conditions are correct (mainly determined by the cylinder radius), the focus has been shifted away from the superfluid phase transition. It would be very valuable to witness a simulation study that is strictly determined to establish trends in the superfluid nature of helium films adsorbed on cylindrical geometries.

References

[1] D. D. Osheroff, R. C. Richardson, and D. M. Lee, "Evidence for a new phase of solid ^{3}He," *Phys. Rev. Lett.*, vol. 28, no. 14, pp. 885–888, 1972.

[2] D. D. Osheroff, W. J. Gully, R. C. Richardson, and D. M. Lee, "New magnetic phenomena in liquid ^{3}He below 3 mK," *Phys. Rev. Lett.*, vol. 29, no. 14, pp. 920–923, 1972.

[3] D. R. Tilley and J. Tilley, *Superfluidity and Superconductivity*. Graduate Student Series in Physics, IOP, 3rd ed., 1990.

[4] J. Wilks and D. S. Betts, *An Introduction to Liquid Helium*. Oxford University Press, 2nd ed., 1987.

[5] R. J. Donnelly, *Quantized Vortices in Helium II*. Cambridge Studies in Low Temperature Physics, Cambridge University Press, 1991.

[6] J. F. Annett, *Superconductivity, Superfluids and Condensates*. Oxford Master Series in Condensed Matter Physics, Oxford University Press, 2004.

[7] F. London, *Superfluids: Macroscopic Theory of Superfluid Helium*, vol. 2. Dover, 1964.

[8] L. D. Landau and E. M. Lifshitz, *Fluid Mechanics*, vol. 6 of *Course of Theoretical Physics*. Pergamon Press, 1987.

[9] R. A. Aziz, V. P. S. Nain, J. S. Carley, W. L. Taylor, and G. T. McConville, "An accurate intermolecular potential for helium," *J. Chem. Phys.*, vol. 70, no. 9, pp. 4330–4342, 1979.

[10] M. J. Buckingham and W. M. Fairbank, "The nature of the λ-transition in liquid helium," *Progress in Low Temperature Physics*, vol. 3, pp. 80–112, 1961.

[11] P. Kapitza, "Viscosity of liquid helium below the λ-point," *Nature*, vol. 141, no. 3558, p. 74, 1938.

[12] J. F. Allen and A. D. Misener, "Flow of liquid Helium II," *Nature*, vol. 142, no. 3597, p. 643, 1938.

[13] J. D. Reppy and D. Depatie, "Persistent currents in superfluid helium," *Phys. Rev. Lett.*, vol. 12, no. 8, pp. 187–189, 1964.

[14] L. Tisza, "Transport phenomena in Helium II," *Nature*, vol. 141, p. 913, 1938.

[15] A. Leitner, "Physics demonstration: Superfluid liquid helium (isotope 4)."

[16] F. London *Nature*, vol. 141, p. 643, 1928.

[17] L. D. Landau *J. Phys. (USSR)*, vol. 5, p. 71, 1941.

[18] E. L. Andronikashvili *J. Phys. (USSR)*, vol. 10, p. 201, 1946.

[19] T. R. Sosnick, W. M. Snow, R. N. Silver, and P. E. Sokol, "Deviations from the impulse approximation in liquid ^{4}He: An experimental test at $q = 23$ å$^{-1}$," *Phys. Rev. B.*, vol. 43, no. 1, pp. 216–228, 1991.

[20] P. A. Whitlock and R. M. Panoff, "Accurate momentum distributions from computations on ^{3}He and ^{4}He," *Can. J. Phys.*, vol. 65, no. 11, pp. 1409–1415, 1987.

[21] D. M. Ceperley and E. L. Pollock, "The momentum distribution of normal and superfluid liquid ^{4}He," *Can. J. Phys.*, vol. 65, no. 11, pp. 1416–1420, 1987.

[22] S. Moroni, G. Senatore, and S. Fantoni, "Momentum distribution of liquid helium," *Phys. Rev. B.*, vol. 55, no. 2, pp. 1040–1049, 1997.

[23] V. L. Ginzburg and L. D. Landau, "On the theory of superconductivity," *J. Phys. (USSR)*, vol. 20, no. 1064, 1950.

[24] L. Onsager, "Statistical hydrodynamics," *Nuovo Cim. Suppl. 9*, vol. 6, pp. 249–287, 1949.

[25] R. P. Feynman, "Application of quantum mechanics to liquid helium," in *Progress in Low Temperature Physics* (C. J. Gorter, ed.), vol. 1, p. 17, North-Holland, 1955.

[26] G. A. Williams and R. E. Packard, "A technique for photographing vortex positions in rotating superfluid helium," *J. Low Temp. Phys.*, vol. 39, no. 5/6, pp. 553–577, 1980.

[27] P. W. Anderson, "Considerations on the flow of superfluid helium," *Rev. Mod. Phys.*, vol. 38, no. 2, pp. 298–310, 1966.

[28] H. R. Glyde, *Excitations in Liquid and Solid Helium.* Clarendon, 1994.

[29] H. Godfrin, M. Meschke, H. J. Lauter, A. Sultan, H. M. Bohm, E. Krotscheck, and M. Panholzer, "Observation of a roton collective mode in a two-dimensional fermi liquid," *Nature*, vol. 483, no. 576-579, 2012.

[30] L. D. Landau, "Theory of superfluidity of Helium II," *J. Phys. (USSR)*, vol. 11, pp. 91–92, 1947.

[31] D. G. Henshaw and A. D. B. Woods, "Modes of atomic motions in liquid helium by inelastic scattering of neutrons," *Phys. Rev.*, vol. 121, no. 5, pp. 1266–1274, 1961.

[32] T. Ellis, C. I. Jewell, and P. V. E. McClintock, "Measurement of the Landau velocity in He II," *Phys. Lett. A*, vol. 78, no. 4, pp. 358–360, 1980.

[33] F. W. Sheard and R. M. Bowley, "Influence of one-roton emission processes on the velocity-field characteristics of negative ions in liquid ^{4}He at very low temperatures," *Phys. Rev. B.*, vol. 17, no. 1, pp. 201–203, 1978.

[34] J. S. Brooks and R. J. Donnelly, "The calculated thermodynamic properties of superfluid Helium-4," *J. Phys. Chem. Ref. Data*, vol. 6, no. 1, pp. 51–104, 1977.

[35] J. D. Reppy, "Application of a superfluid gyroscope to the study of critical velocities in liquid helium near the λ transition," *Phys. Rev. Lett.*, vol. 14, no. 18, pp. 733–735, 1965.

[36] J. S. Langer and J. D. Reppy, "Intrinsic critical velocities in superfluid helium," in *Progress in Low Temperature Physics* (C. J. Gorter, ed.), vol. 6, ch. 1, pp. 1–35, North-Holland, 1970.

[37] D. J. Bishop and J. D. Reppy, "Study of superfluid transition in two-dimensional ^{4}He films," *Phys. Rev. Lett.*, vol. 40, no. 26, pp. 1727–1730, 1978.

[38] V. Ambegaokar, B. I. Halperin, D. R. Nelson, and E. D. Siggia, "Dynamics of superfluid films," *Phys. Rev. B.*, vol. 21, no. 5, pp. 1806–1826, 1980.

[39] J. M. Kosterlitz and D. J. Thouless, "Ordering, metastability and phase transitions in two-dimensional systems," *J. Phys. C.*, vol. 6, pp. 1181–1203, 1973.

[40] D. R. Nelson and J. M. Kosterlitz, "Universal jump in the superfluid density of two-dimensional superfluids," *Phys. Rev. Lett.*, vol. 39, no. 19, pp. 1201–1205, 1977.

[41] H. Cho, *Vortex Core Size in Submonolayer Superfluid Helium-4 Films*. PhD thesis, UCLA, 1996.

[42] I. Rudnick, "Critical surface density of the superfluid component in ^{4}He films," *Phys. Rev. Lett.*, vol. 40, no. 22, pp. 1454–1455, 1978.

[43] V. Kotsubo and G. A. Williams, "Superfluid transition of ^{4}He films adsorbed in porous materials," *Phys. Rev. B.*, vol. 33, no. 9, pp. 6106–6122, 1986.

[44] T. Minoguchi and Y. Nagaoka, "Vortices, superfluidity and phase transition in ^{4}He films adsorbed on porous materials," *Prog. Theo. Phys.*, vol. 80, no. 3, pp. 397–416, 1988.

[45] J. Machta and R. A. Guyer, "Superfluid films in porous media," *Phys. Rev. Lett.*, vol. 60, no. 20, 1988.

[46] F. Gallet and G. A. Williams, "Superfluid transition of ^{4}He films adsorbed on multiply connected surfaces," *Phys. Rev. B.*, vol. 39, no. 7, pp. 4673–4676, 1989.

[47] G. A. Williams, "Vortex-ring model of the superfluid λ transition," *Phys. Rev. Lett.*, vol. 59, no. 17, pp. 1926–1929, 1987.

[48] A. K. Nguyen and A. Sudbo, "Topological phase fluctuations, amplitude fluctuations, and criticality in extreme type-II superconductors," *Phys. Rev. B.*, vol. 60, no. 22, pp. 15307–15331, 1999.

[49] K. R. Atkins, "Third and fourth sound in liquid Helium II," *Phys. Rev.*, vol. 113, no. 4, pp. 962–965, 1959.

[50] G. A. Williams, R. Rosenbaum, and I. Rudnick, "Fifth sound in superfluid ^{4}He and ^{3}He-^{4}He mixtures," *Phys. Rev. Lett.*, vol. 42, no. 19, pp. 1282–1285, 1979.

[51] G. A. Williams, *Wave Modes in Liquid Helium*, vol. 2 of *Encyclopedia of Acoustics*, ch. 59, pp. 673–682. John Wiley and Sons, 1997.

[52] K. R. Atkins, "Ripplons and the critical velocity of the helium film," *Physica*, vol. 23, pp. 1143–1144, 1957.

[53] K. R. Atkins, B. Rosenbaum, and H. Seki, "Evaporation effects during superflow of liquid Helium II," *Phys. Rev.*, vol. 113, no. 3, pp. 751–754, 1959.

[54] I. Rudnick and J. C. Fraser, "Third sound and the superfluid parameters of thin helium films," *J. Low Temp. Phys.*, vol. 3, no. 3, pp. 225–234, 1970.

[55] G. Zimmerli, G. Mistura, and M. H. W. Chan, "Third-sound study of a layered superfluid film," *Phys. Rev. Lett.*, vol. 68, no. 1, pp. 60–63, 1992.

[56] I. Rudnick, R. S. Kagiwada, J. C. Fraser, and E. Guyon, "Third sound in adsorbed superfluid films," *Phys. Rev. Lett.*, vol. 20, no. 9, pp. 430–432, 1968.

[57] J. S. Brooks, F. M. Ellis, and R. B. Hallock, "Direct observation of third-sound mass displacement in unsaturated ^{4}He films," *Phys. Rev. Lett.*, vol. 40, no. 4, pp. 240–243, 1978.

[58] J. J. M. Valles, D. T. Smith, and R. B. Hallock, "Third sound in ^{4}He adsorbed on Nuclepore," *Phys. Rev. Lett.*, vol. 54, no. 14, pp. 1528–1531, 1985.

[59] D. T. Smith, K. M. Godshalk, and R. B. Hallock, "Adsorption and capillary condensation of ^{4}He on nuclepore: Third-sound and capacitance measurements," *Phys. Rev. B.*, vol. 36, no. 1, pp. 202–217, 1987.

[60] J. A. Roth, G. J. Jelatis, and J. D. Maynard, "Third-sound velocity and onset on Grafoil," *Phys. Rev. Lett.*, vol. 44, no. 5, pp. 333–337, 1980.

[61] D. Bergman, "Hydrodynamics and third sound in thin He II films," *Phys. Rev.*, vol. 188, no. 1, pp. 370–384, 1969.

[62] D. J. Bergman, "Third sound in superfluid helium films of arbitrary thickness," *Phys. Rev. A.*, vol. 3, no. 6, pp. 2058–2066, 1971.

[63] R. C. Richardson and E. N. Smith, *Experimental Techniques in Condensed Matter Physics at Low Temperatures.* Addison-Wesley, 1988.

[64] J. C. Wheatley, "Dilute solutions of ^{3}He in ^{4}He at low temperatures," *Am J Phys*, vol. 36, no. 3, pp. 181–210, 1968.

[65] O. V. Lounasmaa, *Experimental Principles and Methods Below 1K.* Academic Press, 1974.

[66] E. Webster, G. Webster, and M. Chester, "Precipitous onset for superfluidity in ^{3}He-^{4}He mixtures," *Phys. Rev. Lett.*, vol. 42, no. 4, pp. 243–246, 1979.

[67] D. McQueeney, G. Agnolet, and J. D. Reppy, "Surface superfluidity in dilute ^{3}He-^{4}He mixtures," *Phys. Rev. Lett.*, vol. 52, no. 15, pp. 1325–1328, 1984.

[68] D. J. Bishop, J. E. Berthold, J. M. Parpia, and J. D. Reppy, "Superfluid density of thin ^{4}He films adsorbed in porous Vycor glass," *Phys. Rev. B.*, vol. 24, no. 9, pp. 5047–5057, 1981.

[69] S. M. Cohen, R. A. Guyer, and J. Machta, "Hydrodynamic modes of superfluid helium adsorbed on Nuclepore," *Phys. Rev. B.*, vol. 33, no. 7, pp. 4664–4668, 1986.

[70] H. Yano, S. Yoshizaki, S. Inagaki, Y. Fukushima, and N. Wada, "Observation of superfluid ^{4}He adsorbed in one-dimensional mesopores," *J. Low Temp. Phys.*, vol. 110, no. 1/2, pp. 573–578, 1998.

[71] H. Cho and G. A. Williams, "One-dimensional excitations in superfluid ^{4}He and ^{3}He-^{4}He mixture films adsorbed in porous materials," *Phys. Rev. B.*, vol. 64, no. 144503, 2001.

[72] H. Chu and G. A. Williams, "Superfluid density of ^{4}He films adsorbed in porous MCM-41 ceramic," *J. Low Temp. Phys.*, vol. 138, no. 1/2, pp. 343–348, 2005.

[73] H. Cho and G. A. Williams, "Superfluid phase transition of ^{3}He-^{4}He mixture films adsorbed on alumina powder," *J. Low Temp. Phys.*, vol. 110, no. 1/2, pp. 533–538, 1998.

[74] H. Cho and G. A. Williams, "Vortex core size in submonolayer superfluid ^{4}He films," *Phys. Rev. Lett.*, vol. 75, no. 8, pp. 1562–1565, 1995.

[75] M. Bernard and G. A. Williams, "Surface and bulk tortuosity of porous ceramics near the percolation threshold," *Phys. Rev. Lett.*, vol. 67, no. 18, pp. 2585–2588, 1991.

[76] C. Laurent, E. Flahaut, and A. Peigney, "The weight and density of carbon nanotubes versus the number of walls and diameter," *Carbon*, vol. 48, no. 10, pp. 2994–2996, 2010.

[77] M. Bernard, *Tortuosity Measurements of Porous Ceramics using Superfluid Acoustics*. PhD thesis, UCLA, 1992.

[78] S. Feng, B. I. Halperin, and P. N. Sen, "Transport properties of continuum systems near the percolation threshold," *Phys. Rev. B.*, vol. 35, no. 1, pp. 197–214, 1987.

[79] H. Preston-Thomas, "The International Temperature Scale of 1990 (ITS-90)," *Metrología*, vol. 27, pp. 3–10, 1990.

[80] V. A. Kirsch, "Calculation of the van der Waals force between a spherical particle and an infinite cylinder," *Adv. Colloid Interface Sci.*, vol. 104, pp. 311–324, 2003.

[81] H. J. Lauter, H. Godfrin, and P. Leiderer, "^{4}He films on graphite studied by neutron scattering," *J. Low Temp. Phys.*, vol. 87, no. 3/4, pp. 425–443, 1992.

[82] E. Cheng and M. W. Cole (Unpublished).

[83] J. Frenkel, *Kinetic Theory of Liquids*. Oxford University Press, 1946.

[84] G. D. Halsey, "Physical adsorption on non-uniform surfaces," *J. Chem. Phys.*, vol. 16, no. 10, pp. 931–937, 1948.

[85] T. L. Hill, "Statistical mechanics of multimolecular adsorption. i," vol. 14, no. 4, pp. 263–267, 1946.

[86] J. G. Dash, *Films on Solid Surfaces*. Academic Press, 1975.

[87] M. S. Dresselhaus, G. Dresselhaus, and P. Avouris, *Carbon Nanotubes: Synthesis, Structure, Properties, and Applications*, vol. 80 of *Topics in Applied Physics*. Springer, 2001.

[88] S. Ramesh and J. D. Maynard, "Measurement of epitaxial adsorption of solid ^{4}He on graphite," *Phys. Rev. Lett.*, vol. 49, no. 1, pp. 47–50, 1982.

[89] P. A. Crowell and J. D. Reppy, "Superfluidity and film structure in ^{4}He adsorbed on graphite," *Phys. Rev. B.*, vol. 53, no. 5, pp. 2701–2718, 1996.

[90] P. J. Shirron and J. M. Mochel, "Atomically thin superfluid helium films on solid hydrogen," *Phys. Rev. Lett.*, vol. 67, no. 9, pp. 1118–1121, 1991.

[91] J. M. Mochel and M. T. Chen, "Superfluid helium on solid hydrogen," *Physica B*, vol. 197, pp. 278–282, 1994.

[92] E. S. Sabisky and C. H. Anderson, "Verification of the Lifshitz theory of the van der Waals potential using liquid-helium films," *Phys. Rev. A.*, vol. 7, no. 2, pp. 790–806, 1973.

[93] J. A. Herb and J. G. Dash, "Mass transport of ^{4}He films adsorbed on graphite," *Phys. Rev. Lett.*, vol. 29, no. 13, pp. 846–848, 1972.

[94] M. Bretz, J. G. Dash, D. C. Hickernell, E. O. McLean, and O. E. Vilches, "Phases of ^{3}He and ^{4}He monolayer films adsorbed on basal-plane oriented graphite," *Phys. Rev. A.*, vol. 8, no. 3, pp. 1589–1615, 1973.

[95] S. E. Polanco and M. Bretz, "Thermal resistivity of layered ^{4}He films on ZYX graphite below 2 K," *Surf. Sci.*, vol. 94, pp. 1–15, 1980.

[96] D. S. Greywall and P. A. Busch, "Heat capacity of fluid monolayers of ^{4}He," *Phys. Rev. Lett.*, vol. 67, no. 25, pp. 3535–3538, 1991.

[97] L. Dang and M. Boninsegni, "Phases of lattice hard-core bosons in a perioidic superlattice," *Phys. Rev. B.*, vol. 81, no. 224502, 2010.

[98] P. Corboz, M. Boninsegni, L. Pollet, and M. Troyer, "Phase diagram of ^{4}He adsorbed on graphite," *Phys. Rev. B.*, vol. 78, no. 245414, 2008.

[99] J. Happacher, P. Corboz, M. Boninsegni, and L. Pollet, "Phase diagram of ^{4}He on graphene," *Phys. Rev. B.*, vol. 87, no. 094514, 2013.

[100] D. Y. Kim and M. H. W. Chan, "Absence of supersolidity in solid helium in porous Vycor glass," *Phys. Rev. Lett.*, vol. 109, no. 155301, 2012.

[101] S. H. Kim, G. W. Mulholland, and M. R. Zachariah, "Density measurement of size selected multiwalled carbon nanotubes by mobility-mass characterization," *Carbon*, vol. 47, no. 5, pp. 1297–1302, 2009.

[102] A. Peigney, C. Laurent, E. Flahaut, R. R. Basca, and A. Rousset, "Specific surface area of carbon nanotubes and bundles of carbon nanotubes," *Carbon*, vol. 39, no. 4, pp. 507–514, 2001.

[103] G. Zimmerli, *Multilayer Growth and Wetting of Films Physisorbed on Graphite*. PhD thesis, The Pennsylvania State University, 1990.

[104] R. Rosenbaum, G. A. Williams, D. Heckerman, J. Marcus, D. Scholler, J. Maynard, and I. Rudnick, "Surface tension sound in superfluid helium films adsorbed on alumina powder," *J. Low Temp. Phys.*, vol. 37, no. 5/6, pp. 663–678, 1979.

[105] E. Cheng, W. F. Saam, M. W. Cole, and J. Treiner, "Theoretical study of third sound in a layered superfluid film," *J. Low Temp. Phys.*, vol. 92, no. 1/2, pp. 11–24, 1993.

[106] P. A. Whitlock, G. V. Chester, and M. H. Kalos, "Monte Carlo study of ^{4}He in two dimensions," *Phys. Rev. B.*, vol. 38, no. 4, pp. 2418–2425, 1988.

[107] B. E. Clements, J. L. Epstein, E. Krotscheck, and M. Saarela, "Structure of boson quantum films," *Phys. Rev. B.*, vol. 48, no. 10, pp. 7450–7470, 1993.

[108] B. E. Clements, H. Forbert, E. Krotscheck, H. J. Lauter, M. Saarela, and C. J. Tymczak, "Dynamics of boson quantum films," *Phys. Rev. B.*, vol. 50, no. 10, pp. 6958–6981, 1994.

[109] H. J. Lauter, H. Godfrin, V. L. P. Frank, and P. Leiderer, *Phase Transitions in Surface Films 2*, ch. Neutron Scattering Studies of Quantum Films, pp. 135–152. Plenum, 1991.

[110] K. Penanen and R. E. Packard, "A model for third sound attenuation in thick ^{4}He films," *J. Low Temp. Phys.*, vol. 128, no. 1/2, pp. 25–35, 2002.

[111] E. Kim and M. H. W. Chan, "Probable observation of a supersolid helium phase," *Nature*, vol. 427, no. 225-227, 2004.

[112] J. Day and J. Beamish, "Low-temperature shear modulus changes in solid ^{4}He and connection to supersolidity," *Nature*, vol. 450, no. 853-856, 2007.

[113] H. J. Maris and S. Balibar, "Effect of helium elasticity on torsional oscillator measurements," *J. Low Temp. Phys.*, vol. 162, pp. 12–22, 2011.

[114] J. D. Reppy, X. Mi, A. Justin, and E. J. Mueller, "Interpreting torsional oscillator measurements: Effect of shear modulus and supersolidity," *J. Low Temp. Phys.*, vol. 168, pp. 175–193, 2012.

[115] I. Iwasa, "Dislocation-vibration model for nonclassical rotational inertia," *Phys. Rev. B.*, vol. 81, no. 104527, 2010.

[116] D. S. Greywall, "Heat capacity and the commensurate-incommensurate transition of ^{4}He adsorbed on graphite," *Phys. Rev. B.*, vol. 47, no. 1, pp. 309–318, 1993.

[117] W. F. Saam and M. W. Cole, "Excitations and thermodynamics for liquid-helium films," *Phys. Rev. B.*, vol. 11, no. 3, pp. 1086–1105, 1975.

[118] D. Hecht, L. Hu, and G. Gruner, "Conductivity scaling with bundle length and diameter in single walled carbon nanotube networks," *Appl. Phys. Lett.*, vol. 89, no. 133112, 2006.

[119] J. Machta and R. A. Guyer, "Superfluid films on a cylindrical surface," *J. Low Temp. Phys.*, vol. 74, no. 3/4, pp. 231–261, 1989.

[120] S. J. Gregg and K. S. W. Sing, *Adsorption, Surface Area and Porosity.* Academic Press, 1967.

[121] S. Vo, H. Fard, A. Kogar, and G. A. Williams, "Adsorption properties and third sound propagation in superfluid ^{4}He films on carbon nanotubes," *J. Phys.: Conf. Ser.*, vol. 150, no. 032117, 2009.

[122] Y. Kwon and D. M. Ceperley, "^{4}He adsorption on a single graphene sheet: Path-integral Monte Carlo study," *Phys. Rev. B.*, vol. 85, no. 224501, 2012.

[123] Y. Kwon and H. Shin, "Superfluidity and structural order in ^{4}He adsorbed on a C_{20} molecule: Path-integral Monte Carlo calculations," *Phys. Rev. B.*, vol. 82, no. 172506, 2010.

[124] M. C. Gordillo, "^{4}He adsorbed on the outer surface of carbon nanotube bundles," *Phys. Rev. Lett.*, vol. 101, no. 046102, 2008.

[125] M. C. Gordillo, J. Boronat, and J. Casulleras, "^{4}He adsorbed inside (10,10) single-walled carbon nanotubes," *Phys. Rev. B.*, vol. 76, no. 193402, 2007.

[126] M. C. Gordillo and J. Boronat, "^{4}He adsorbed outside a single carbon nanotube," *Phys. Rev. B.*, vol. 86, no. 165409, 2012.

[127] A. D. Leuking and M. W. Cole, "Commensurate phases of gases adsorbed on carbon nanotubes," *Phys. Rev. B.*, vol. 75, no. 195425, 2007.